Eindige-elementen- en FDTD-gebaseerde technieken voor de tijdsdomeinsimulatie van interacties tussen plasma's en elektromagnetische golven

Finite Element and Finite Difference Based Approaches for the Time-Domain Simulation of Plasma-Wave Interactions

Wouter Tierens

Promotor: prof. dr. ir. D. De Zutter
Proefschrift ingediend tot het behalen van de graad van
Doctor in de Ingenieurswetenschappen: Toegepaste Natuurkunde

Vakgroep Informatietechnologie
Voorzitter: prof. dr. ir. D. De Zutter
Faculteit Ingenieurswetenschappen en Architectuur
Academiejaar 2012 - 2013

UNIVERSITEIT
GENT

ISBN 978-90-8578-590-3
NUR 928, 919
Wettelijk depot: D/2013/10.500/23

Acknowledgments

I would like to thank the following people

- My promotor prof. Daniël De Zutter, whose excellent advice has been of great help, especially relating to the more diplomatic aspects of research work.
- prof. Guido Van Oost, without whom I would probably not have written a master's thesis, let alone a PhD. , in the field of plasma physics.
- dr. Dirk Van Eester, who was always ready to give feedback.

Gent, March 2013
Wouter Tierens

Contents

Summary

In this doctoral thesis, a fully spatio-temporally collocated time-domain discretisation of Maxwell's equations is developed, useful for the simulation of magnetized plasmas. This method has the following properties

- It is unconditionally stable: this contrasts with the FDTD method [16] where the Courant condition, $c\Delta_t < \Delta$, must be obeyed. For materials where the propagation speed of the electromagnetic waves differs significantly from the vacuum speed of light c, this enables the adaptation of the spatial discretisation length Δ to the wavelength, and of the time step Δ_t to the period, independently. To model such materials while obeying the Courant condition, either the number of space steps per wavelength would be much larger than the number of time steps per period, or vice versa, but the discretisation error remains dominated by the worst-resolved of these.
- The discretisation length Δ need not be uniform, adapting it to the (non-uniform) wave equation under consideration is possible, and carries no cost in terms of stability or accuracy. In FDTD, on the other hand, a uniform grid is required to maintain second-order accuracy.
- Fully collocated, i.e. all field components are discretized on the same spatio-temporal positions. Constitutive equations for anisotropic materials, such as magnetized plasmas, which require all components of a vector field at a certain position, can be discretized in their natural form, without additional interpolations. The difficulty of modelling general anisotropic materials in staggered (non-collocated) approaches has been widely pointed out in the relevant literature [13, 19, 20, 21, 11].
- Requires the solution of a sparse set of equations at every time step. This is a disadvantage relative to pure FDTD, where an explicit solution is available. It is also a disadvantage relative to hybrid approaches [13], which, while not entirely explicit, still require only linear time $O(N)$ for a single time step.

We use this method to model interactions between electromagnetic waves and magnetized plasmas, phenonema which are of interest in both fusion science [10, 15, 3, 8, 5, 9] and astrophysics [12, 6]. We start with the well-known cold plasma model [13, 14],

$$\frac{\partial \vec{J}_s}{\partial t} = \epsilon_0 \omega_s^2 \vec{E} - \vec{\Omega}_s \times \vec{J} \tag{1}$$

where $\vec{J}_s$ is the current density associated with particle specie s, $\omega_s^2 = \frac{n_s q_s^2}{m_s \epsilon_0}$ is the plasma frequency for this specie (n_s is the density, q_s the charge and m_s the mass), and $\vec{\Omega}_s = \frac{q_s \vec{B}_0}{m_s}$ is the cyclotron frequency due to the background magnetic field $\vec{B}_0$. (1) is Newton's law given the electric force and the Lorentz force due to an externally applied background magnetic field. It is precisely this cross product which makes staggered approaches somewhat problematic: if several components of a vectorfield are discretized on different positions, calculating a component of the cross product of this vector-field with a given “background” vector-field requires interpolating components to collocated positions, which introduces non-physical interpolation operators in the components which are interpolated to collocated positions but not in the components which are already on the desired positions. This, in turn, tends to “pollute” the discrete dispersion relation.

Later on, we also develop more advanced plasma descriptions that more closely approximate the behaviour of hot Maxwellian plasmas [3, 15]. The dielectric tensor describing such hot plasma is rather unpractical from a computational point of view: it can only be expressed as an infinite sum of which each term contains special functions. Our approximations to it are conceptually similar to the standard Finite Larmor Radius (FLR) approximation [2], i.e. they rely on a finite-order series in $\lambda = \frac{k_x^2 v_{th}^2}{2\Omega_s^2}$, which is assumed to be small (v_{th} is the thermal velocity). The resulting finite-order expressions can then be transformed into time-domain differential equations by inverse Fourier transforms as in [7]. However, our approximations are rational rather than polynomial, and chosen such that the resulting time-domain differential equations are unconditionally stable: they obey an energy conservation law even when the assumed small expansion parameter is not actually small. The maximum possible value of k_x^2, and with it the maximum possible value of λ, is determined by the discretisation (usually $k_{\max} = \pi/\Delta$). Bounding it would require, in time-domain, either making Δ sufficiently large and thereby limiting the ability to resolve short wavelengths, or filtering out short wavelength components at every time step. By choosing an unconditionally well-behaved set of equations, we sidestep this problem entirely.

We have been able to use these models to numerically produce the lowest-order Bernstein wave. For now, these approximations are limited to perpendicular propagation, i.e. the wavevector $\vec{k}$ is perpendicular to the background magnetic field. We give solutions for both the $\vec{E} \perp \vec{B}_0$ and $\vec{E} \parallel \vec{B}_0$ cases, unlike in [18] where only $\vec{E} \perp \vec{B}_0$ was discussed. As a consequence of the perpendicular propagation, there are no loss terms and no collisionless Landau damping [1, 22].

Finally, we hybridize this fully implicit method with the standard FDTD method. This enables the local use of very small discretisation lengths in the fully implicit parts, while the FDTD parts can be run at the standard FDTD Courant limit. In 1D, this hybridisation is free of spurious reflections at the interface. We use this to calculate transmission coefficients for waves propagating through thin layers of conducting materials, and to solve the Budden tunneling equation.

Aside from all this, this thesis also contains some tangential work on explicit local refinement techniques in toroidal geometries [17]. In [4], a provably stable three-dimensional local refinement algorithm was constructed for FDTD. This method is based on constructing basis-functions which obey the so-called curl inclusion property: the magnetic basis-functions exactly span the curl of electric basis-functions. In cartesian coordinates, this gives rise to fairly simple pulse and triangle functions. The Finite Element description based on these functions reduces to classical FDTD if the testing integrals are calculated using trapezoidal integration ("mass lumping"). However, the Finite Element formulation is flexible enough to enable local refinement by connecting the triangle and pulse functions with smaller versions of themselves.

In cylindrical coordinates (Body-Of-Revolution, "BOR" FDTD), the situation is more complicated. Nonetheless, we managed to construct a set of nearly-triangular and nearly-rectangular basis-functions which obey the curl inclusion property in cylindrical coordinates. Using this, we were able to extend the algorithms of [4] to toroidal geometries. We used this technique to calculate the eigenfrequencies of a rotationally symmetric cavity with a sharp internal feature.

Bibliography

[1] R. Bilato and M. Brambilla. On the nature of “collisionless” Landau damping. *Communications in Nonlinear Science and Numerical Simulation*, 13(1):18 – 23, 2008.

[2] M. Brambilla. Finite Larmor radius wave equations in tokamak plasmas in the ion cyclotron frequency range. *Plasma Physics and Controlled Fusion*, 31(5):123–151, 1989.

[3] M. Brambilla. *Kinetic theory of plasma waves*. Clarendon Press, 1998.

[4] R. A. Chilton. *H-, P- and T-refinement strategies for the finite-difference-time-domain (FDTD) method developed via finite-element (FE) principles*. PhD thesis, Ohio State University, 2008.

[5] D. Van Eester and R. Koch. A variational principle for studying fast-wave mode conversion. *Plasma Physics and Controlled Fusion*, 40(11):1949, 1999.

[6] DA Gurnett, WS Kurth, A. Roux, SJ Bolton, and CF Kennel. Evidence for a magnetosphere at ganymede from plasma-wave observations by the Galileo spacecraft. *Nature*, 384(6609):535–537, 1996.

[7] R. M. Joseph, S. C. Hagness, and A. Taflove. Direct time integration of Maxwell’s equations in linear dispersive media with absorption for scattering and propagation of femtosecond electromagnetic pulses. *Optics Letters*, 16(18):1412–1414, May 1991.

[8] Y. Kazakov, I. Pavlenko, D. Van Eester, B. Weyssow, and I. Girka. Enhanced ICRF (ion cyclotron range of frequencies) mode conversion efficiency in plasmas with two mode conversion layers. *Plasma Physics and Controlled Fusion*, 52(11):115006, 2010.

[9] H. P. Laqua. Electron Bernstein wave heating and diagnostic. *Plasma Physics and Controlled Fusion*, 49(4):1–42, 2007.

[10] M.J. Mantsinen, M.-L. Mayoral, and D. Van Eester. Localized bulk electron heating with ICRF mode conversion in the JET tokamak. *Nuclear Fusion*, 44(1):33–46, 2004.

[11] M. Nauta. FDTD method on a Lebedev grid for anisotropic materials. *IEEE APS conference paper*, 2012.

[12] H. Oya. Origin of jovian decameter wave emissions-conversion from the electron cylotron plasma wave to the ordinary mode electromagnetic wave. *Planetary and Space Science*, 22(5):687–708, 1974.

[13] D. N. Smithe. Finite-difference time-domain simulation of fusion plasmas at radiofrequency time scales. *Physics of Plasmas*, 14(14):2537–2549, Apr. 2007.

[14] D. N. Smithe. Time domain modeling of plasmas at RF time-scales. *Journal of Physics: Conference Series*, 78(1):012069, 2007.

[15] T. Stix. *Waves in Plasmas*. American Institute of Physics, 1992.

[16] A. Taflove and S. Hagness. *Computational Electrodynamics: The Finite-Difference Time-Domain Method*. Artech House, 2005.

[17] W. Tierens and D. De Zutter. BOR-FDTD subgridding based on finite element principles. *Journal of Computational Physics*, pages 4519–4535, 2011.

[18] W. Tierens and D. De Zutter. Finite-temperature corrections to the time-domain equations of motion for perpendicular propagation in nonuniform magnetized plasmas. *Physics of Plasmas*, 19:1–9, 2012.

[19] W. Tierens and D. De Zutter. An unconditionally stable time-domain discretization on cartesian meshes for the simulation of nonuniform magnetized cold plasma. *Journal of Computational Physics*, pages 5144–5156, 2012.

[20] J.L. Young. A full finite difference time domain implementation for radio wave propagation in a plasma. *Radio Science*, pages 1513–1522, 1994.

[21] Y. Yu. An E-J collocated 3-D FDTD model of electromagnetic wave propagation in magnetized cold plasma. *IEEE transactions on Antennas and Propagation*, 58(2):469–478, 2010.

[22] T. Zhou, Y. Gue, and C. Shu. Numerical study on Landau damping. *Physica D*, 157(4):322–333, 2001.

Samenvatting

In deze doctoraatsthesis construeren we een volledig gelocalizeerde (collocated) tijdsdomein-discretisatie van Maxwell's vergelijkingen. Dit is bruikbaar voor de numerieke simulatie van gemagnetiseerde plasmas. Onze methode heeft de volgende eigenschappen

- Ze is onvoorwaardelijk stabiel: dit staat in contrast tot de klassieke FDTD methode [15] waar aan de Courant-voorwaarde $c\Delta_t < \Delta$ voldaan moet zijn. Voor materialen waar de voortplantingssnelheid van de elektromagnetische golven sterk afwijkt van de lichtsnelheid in vacuum c, stelt dit ons in staat de spatiale discretisatielengte Δ aan te passen aan de golflengte en de tijdsstap Δ_t aan de periode, en dit onafhankelijk van elkaar. Om zo een materiaal te modelleren als aan de Courant voorwaarde voldaan moet zijn, moet ofwel de hoeveelheid discretisatielengtes per golflengte veel groter zijn dan de hoeveelheid tijdsstappen per periode, ofwel vice versa, terwijl de discretisatiefout gedomineerd blijft door de slechtst geresolveerde van beide.
- De discretisatie-lengte Δ hoeft niet uniform te zijn, het is mogelijk om deze lengte aan te passen aan de noden van de beschouwde golfvergelijking. Dit kan gebeuren zonder de stabiliteit of nauwkeurigheid te verminderen. In FDTD, aan de andere kant, is een uniform rooster nodig om tweede-orde accuraatheid te garanderen.
- Volledig samen-gelocalizeerd, d.w.z. alle veldcomponenten worden gelocaliseerd op dezelfde spatio-temporele posities. Constitutieve vergelijkingen voor anisotrope materialen, zoals gemagnetiseerde plasmas, waarvoor alle componenten van een vectorveld op dezelfde plaats nodig zijn, kunnen in hun natuurlijke vorm gediscretiseerd worden, zonder extra interpolaties. De moeilijkheid van het modelleren van algemene anisotrope materialen in niet-gelocaliseerde (staggered) aanpakken is algemeen bekend in de relevante literatuur [12, 18, 19, 20, 10].
- Bij iedere tijdsstap moet een stelsel van vergelijkingen opgelost worden. Dit is een nadeel vergeleken met puur FDTD, waar een expliciete oplossing bekend is. Het is ook een nadeel ten opzichte van sommige gedeeltelijk impliciete aanpakken zoals [12] die, hoewel ze niet volledig expliciet zijn, slechts lineaire tijd $O(N)$ nodig hebben voor één tijdsstap.

We gebruiken deze methode om wisselwerkingen tussen elektromagnetische golven en gemagnetiseerde plasmas te modelleren. Deze fenomenen zijn belangrijk

in het fusie-onderzoek [9, 14, 2, 7, 4, 8] en de astrofysica [11, 5]. We starten met het bekende koud plasma-model [12, 13],

$$\frac{\partial \vec{J}_s}{\partial t} = \epsilon_0 \omega_s^2 \vec{E} - \vec{\Omega}_s \times \vec{J} \tag{2}$$

waar $\vec{J}_s$ de stroomdichtheid geassocieerd met deeltjessoort s is, $\omega_s^2 = \frac{n_s q_s^2}{m_s \epsilon_0}$ de plasmafrequentie voor deze deeltjessoort (n_s is de dichtheid, q_s de lading en m_s de massa), en $\vec{\Omega}_s = \frac{q_s \vec{B}_0}{m_s}$ is de cyclotronfrequentie tengevolge van het extern magnetisch veld $\vec{B}_0$. (2) is Newton's wet onder de elektrische kracht en de Lorentzkracht tengevolge van het externe magneetveld. Het is precies dit vectorieel product dat een niet-gelocaliseerde (staggered) aanpak problematisch maakt: als verschillende componenten van een vectorveld gediscretiseerd worden op verschillende posities en we willen een vectorieel product berekenen met een gegeven "achtergrond" vectorveld, dan moeten we bepaalde componenten gaan interpoleren naar de posities waarop andere componenten gediscretiseerd zijn, terwijl we componenten die al op de gewenste plaats staan niet moeten interpoleren. Dit kan voor fouten zorgen in de discrete dispersierelatie.

Later construeren we meer geavanceerde plasma-beschrijvingen die het gedrag van hoge-temperatuur Maxwelliaanse plasmas beter beschrijven [2, 14]. De diëlektrische tensor die deze plasmas beschrijft is onpraktisch vanuit computationeel oogpunt: hij kan alleen uitgedrukt worden als een oneindige som waarvan iedere term speciale functies bevat. Onze benaderingen ervan zijn conceptueel gelijkaardig aan de eindige-Larmor-straal (FLR) benadering [1], d.w.z. ze gebruiken een eindige-orde reeksontwikkeling in $\lambda = \frac{k_x^2 v_{th}^2}{2\Omega_s^2}$, wat verondersteld wordt klein te zijn (v_{th} is de thermische snelheid). De resulterende eindige-orde uitdrukkingen kunnen getransformeerd worden tot tijdsdomein-differentiaalvergelijkingen door middel van de inverse Fouriertransformatie, zoals in [6]. Maar, onze benaderingen zijn rationaal i.p.v. polynomiaal, en op zodanige manier gekozen dat de resulterende tijdsdomein-differentiaalvergelijkingen onvoorwaardelijk stabiel zijn: ze gehoorzamen aan een energie-behoudswet zelfs wanneer de zogezegd kleine parameter λ eigenlijk niet klein is. De grootst mogelijke waarde van k_x^2, en daarmee de grootst mogelijke waarde van λ, wordt bepaald door de discretisatie (gewoonlijk $k_{\max} = \pi/\Delta$). Deze grootheid beperken vereist, in het tijdsdomein, ofwel dat Δ voldoende groot is en dus dat korte golflengten niet meer resolveerbaar zijn, ofwel dat korte golflengten na iedere tijdsstap uitgefilterd moeten worden. Door onvoorwaardelijk stabiele vergelijkingen te construeren vermijden we dit probleem.

We zijn in staat geweest deze modellen te gebruiken om numeriek de laagste-orde Bernsteingolf te produceren. Voorlopig zijn deze benaderingen beperkt tot loodrechte voortplanting, d.w.z. de golfvector $\vec{k}$ staat loodrecht op het extern magnetisch veld. We geven oplossingen voor zowel $\vec{E} \perp \vec{B}_0$ en $\vec{E} \parallel \vec{B}_0$ waar we in

[17] alleen een oplossing voor $\vec{E} \perp \vec{B}_0$ gaven. Tengevolge van de loodrechte voortplanting zijn er geen verliestermen en is er geen botsingsloze Landau demping.

Tot slot hybridizeren we deze volledig impliciete methode met het standaard FDTD model. Dit laat ons toe lokaal een zeer kleine discretisatielengte te gebruiken in de volledig impliciete stukken, terwijl de FDTD stukken nog steeds gehoorzamen aan de standaard Courant voorwaarde. Deze hybridisatie is vrij van onechte (spurious) reflecties aan de interface in 1D. We gebruiken dit om de transmissiecoëfficiënt te berekenen voor een golf die door een dunne laag metaal propageert, en ook om de Budden tunneling vergelijking (Budden tunneling equation) op te lossen.

Deze doctoraatsthesis bevat ook ons vroeger werk i.v.m. expliciete lokale verfijningstechnieken in toroidale geometrieën [16]. In [3] wordt een bewijsbaar stabiel driedimensionaal verfijningsalgoritme voor FDTD geconstrueerd. Deze methode is gebaseerd op het construeren van basis-functies die aan de zogeheten curl inclusion property voldoen: de magnetische basis-functies spannen de rotatie van de elektrische basis-functies op. In cartesische coördinaten geeft dit redelijk eenvoudige driehoekige en rechthoekige functies. De Eindige Elementen beschrijving gebaseerd op deze functies is precies het klassieke FDTD algoritme, tenminste als de integralen berekend worden met trapezoidale integratie (zogeheten mass lumping). De Eindige Elementen beschrijving is flexibel genoeg om lokale verfijning toe te laten door de driehoekige en rechthoekige functies aan kleinere versies van zichzelf te koppelen.

In cylindrische coordinaten (Omwentelingslichaam FDTD (Body-Of-Revolution, “BOR” FDTD)) is de situatie ingewikkelder. We zijn in staat geweest om bijna-driehoekige en bijna-rechthoekige functies te construeren die voldoen aan de curl inclusion property in cylindrische coordinaten. Zo werd het mogelijk om de algoritmes van [3] uit te breiden naar toroidale geometrieën. We hebben deze techniek gebruikt om eigenfrequenties te berekenen van een rotationeel symmetrische caviteit met een scherpe inwendige hoek.

Bibliography

[1] M. Brambilla. Finite Larmor radius wave equations in tokamak plasmas in the ion cyclotron frequency range. *Plasma Physics and Controlled Fusion*, 31(5):123–151, 1989.

[2] M. Brambilla. *Kinetic theory of plasma waves*. Clarendon Press, 1998.

[3] R. A. Chilton. *H-, P- and T-refinement strategies for the finite-difference-time-domain (FDTD) method developed via finite-element (FE) principles*. PhD thesis, Ohio State University, 2008.

[4] D. Van Eester and R. Koch. A variational principle for studying fast-wave mode conversion. *Plasma Physics and Controlled Fusion*, 40(11):1949, 1999.

[5] DA Gurnett, WS Kurth, A. Roux, SJ Bolton, and CF Kennel. Evidence for a magnetosphere at ganymede from plasma-wave observations by the Galileo spacecraft. *Nature*, 384(6609):535–537, 1996.

[6] R. M. Joseph, S. C. Hagness, and A. Taflove. Direct time integration of Maxwell's equations in linear dispersive media with absorption for scattering and propagation of femtosecond electromagnetic pulses. *Optics Letters*, 16(18):1412–1414, May 1991.

[7] Y. Kazakov, I. Pavlenko, D. Van Eester, B. Weyssow, and I. Girka. Enhanced ICRF (ion cyclotron range of frequencies) mode conversion efficiency in plasmas with two mode conversion layers. *Plasma Physics and Controlled Fusion*, 52(11):115006, 2010.

[8] H. P. Laqua. Electron Bernstein wave heating and diagnostic. *Plasma Physics and Controlled Fusion*, 49(4):1–42, 2007.

[9] M.J. Mantsinen, M.-L. Mayoral, and D. Van Eester. Localized bulk electron heating with ICRF mode conversion in the JET tokamak. *Nuclear Fusion*, 44(1):33–46, 2004.

[10] M. Nauta. FDTD method on a Lebedev grid for anisotropic materials. *IEEE APS conference paper*, 2012.

[11] H. Oya. Origin of jovian decameter wave emissions-conversion from the electron cylotron plasma wave to the ordinary mode electromagnetic wave. *Planetary and Space Science*, 22(5):687–708, 1974.

[12] D. N. Smithe. Finite-difference time-domain simulation of fusion plasmas at radiofrequency time scales. *Physics of Plasmas*, 14(14):2537–2549, Apr. 2007.

[13] D. N. Smithe. Time domain modeling of plasmas at RF time-scales. *Journal of Physics: Conference Series*, 78(1):012069, 2007.

[14] T. Stix. *Waves in Plasmas*. American Institute of Physics, 1992.

[15] A. Taflove and S. Hagness. *Computational Electrodynamics: The Finite-Difference Time-Domain Method*. Artech House, 2005.

[16] W. Tierens and D. De Zutter. BOR-FDTD subgridding based on finite element principles. *Journal of Computational Physics*, pages 4519–4535, 2011.

[17] W. Tierens and D. De Zutter. Finite-temperature corrections to the time-domain equations of motion for perpendicular propagation in nonuniform magnetized plasmas. *Physics of Plasmas*, 19:1–9, 2012.

[18] W. Tierens and D. De Zutter. An unconditionally stable time-domain discretization on cartesian meshes for the simulation of nonuniform magnetized cold plasma. *Journal of Computational Physics*, pages 5144–5156, 2012.

[19] J.L. Young. A full finite difference time domain implementation for radio wave propagation in a plasma. *Radio Science*, pages 1513–1522, 1994.

[20] Y. Yu. An E-J collocated 3-D FDTD model of electromagnetic wave propagation in magnetized cold plasma. *IEEE transactions on Antennas and Propagation*, 58(2):469–478, 2010.

List of Symbols

Symbols relating to the hot plasma dielectric tensor

v_{th}	the thermal velocity
$k_{\parallel}$	wavenumber in the direction of propagation, assumed to be the x-direction
$k_{\perp}$	wavenumber perpendicular to the direction of propagation
$\lambda = \frac{k_x^2 v_{th}^2}{2\varOmega^2}$	a second-order partial differential operator related to the Larmor radius, where ik_x corresponds to $\frac{\partial}{\partial x}$ in space
$\mathcal{I}_n(x)$	Modified Bessel function of the first kind of order n
$\varOmega_s$	cyclotron frequency for particle specie s
ω_s	plasma frequency for particle specie s
$Z(\zeta)$	the plasma dispersion function

See section 2.2 for more details.

Matrices and vectors

$\mathfrak{F}$	The discrete Fourier transform operator/matrix
$M^{\dagger}$	Conjugate transpose of the matrix M
I_n	Unit matrix of size $n \times n$
$\mathrm{diag}(a, b, c, \ldots)$	Diagonal matrix with on the diagonal (numbers) $a, b, c, \ldots$
$\mathrm{blkdiag}(a, b, c, \ldots)$	Block-diagonal matrix with on the diagonal (square matrices) $a, b, c, \ldots$
$\vec{1}_x, \vec{1}_y, \vec{1}_z$	Unit vector in the x, y, z direction

Other

$T_{x,n}[f]$	nth order Taylor approximation in x of f, around $x = 0$
$\simeq$	Asymptotic expansion

List of Publications

Articles in international journals

- W. Tierens and D. De Zutter, “BOR-FDTD subgridding based on finite element principles.” *Journal of Computational Physics* (2011).
- W. Tierens and D. De Zutter, “An unconditionally stable time-domain discretization on cartesian meshes for the simulation of nonuniform magnetized cold plasma.” *Journal of Computational Physics* (2012).
- W. Tierens and D. De Zutter, “Finite-temperature corrections to the time-domain equations of motion for perpendicular propagation in nonuniform magnetized plasmas.” *Physics of Plasmas* (2012).
- W. Tierens and D. De Zutter, “Implicit local refinement for evanescent layers combined with classical FDTD.” *accepted for publication in IEEE Wireless Components and Microwave letters* (2013).

Articles in conference proceedings

- W. Tierens, D. De Zutter and K. Cools, “A new approach to BOR-FDTD Subgridding.” *2011 IEEE International Symposium on Antennas and Propagation (APSURSI)*, p. 2300-2302.
- W. Tierens and D. De Zutter, “Time-domain formulation of cold plasma based on mass-lumped finite elements” *2011 AIP Conference Proceedings*, p. 381-384.
- W. Tierens and D. De Zutter, “A time-domain discretisation of Maxwell’s equations in nontrivial media using collocated fields.” *2012 IEEE Antennas and Propagation Society International Symposium (APSURSI)*, p. 1-2.

Scientific award

- Laureate of the “Marianne De Leenheer”-prize, Ghent University, 2008

Finite Element and Finite Difference Based Approaches for the Time-Domain Simulation of Plasma-Wave Interactions

1

General introduction

1.1 Situation

In this work we consider the problem of calculating the interaction between electromagnetic waves and magnetized plasmas, a problem relevant to astrophysics [8, 3] as well as fusion science [6, 11, 1, 4, 2, 5].

We also apply the developed algorithms to somewhat more down-to-earth problems, including the propagation of electromagnetic waves through thin metal sheets.

1.1.1 Computational electrodynamics in cold plasmas

The auxiliary differential equation for magnetized cold plasma is (see chapter 2)

$$\frac{\partial \vec{J}_s}{\partial t} = \epsilon_0 \omega_s^2 \vec{E} - \vec{\Omega}_s \times \vec{J}_s \tag{1.1}$$

It gives the time evolution of the current associated with specie s as a function of the electric field and the current itself (Lorentz-force due to the background magnetic field). The most natural discretisation of this equation requires spatial collocation of the components of $\vec{J}_s$, while Maxwell's equations are usually discretized on staggered grids. Solutions to this problem usualy introduce a form of interpolation [9, 15, 16] from staggered to collocated quantities or vice versa.

Furthermore, the variety of wave phenomena supported even by cold plasma include waves that are much slower than the vacuum wave speed c [9, 11, 6, 4]. Explicit time-domain approaches have a limited maximum time step determined by c, and modeling these slow waves requires extremely dense sampling in time to get waves which are decently resolved in space.

In chapter 3, a discretisation of Maxwell's equations is constructed which is spatially collocated and unconditionally stable.

1.1.2 Computational electrodynamics in warm plasmas

The cold plasma description, while it is the only one commonly found in FDTD-like time-domain computations, does not contain all wave phenomena that occur in hot magnetized plasmas.

Numerical simulation of wave interactions in plasmas where finite-temperature effects are important can be done using direct discretisation of the (often but not always linearized) Vlasov equation as in [17], or by particle-level simulation as in particle-in-cell methods [7].

Time-domain descriptions of warm plasmas based on the auxiliary differential equation (ADE) approach, which has proven successful for cold plasmas, have been rare or non-existent [10]. Indeed, deriving such ADEs is by no means a trivial task. In chapter 2, we derive such ADEs for the case of perpendicular propagation, i.e. the wavevector $\vec{k}$ is perpendicular to the applied background magnetic field.

1.2 Overview of the PhD work

- Chapter 2 discusses time-domain descriptions of magnetized plasmas, including the well-known cold plasma [9] description and finite-temperature corrections. It generalizes the warm plasma descriptions of [13].
- Chapter 3 contains the collocated fully implicit algorithm of [14], and generalizes it to non-uniform grids.
- Chapter 4 contains the majority of the numerical examples in this thesis. Many have been published before [14, 13].
- Chapter 5 discusses earlier and somewhat tangential work on BOR FDTD refinement [12]. It also shows how to construct a hybridised FDTD/fully implicit algorithm.

Bibliography

[1] M. Brambilla. *Kinetic theory of plasma waves*. Clarendon Press, 1998.

[2] D. Van Eester and R. Koch. A variational principle for studying fast-wave mode conversion. *Plasma Physics and Controlled Fusion*, 40(11):1949, 1999.

[3] DA Gurnett, WS Kurth, A. Roux, SJ Bolton, and CF Kennel. Evidence for a magnetosphere at ganymede from plasma-wave observations by the Galileo spacecraft. *Nature*, 384(6609):535–537, 1996.

[4] Y. Kazakov, I. Pavlenko, D. Van Eester, B. Weyssow, and I. Girka. Enhanced ICRF (ion cyclotron range of frequencies) mode conversion efficiency in plasmas with two mode conversion layers. *Plasma Physics and Controlled Fusion*, 52(11):115006, 2010.

[5] H. P. Laqua. Electron Bernstein wave heating and diagnostic. *Plasma Physics and Controlled Fusion*, 49(4):1–42, 2007.

[6] M.J. Mantsinen, M.-L. Mayoral, and D. Van Eester. Localized bulk electron heating with ICRF mode conversion in the JET tokamak. *Nuclear Fusion*, 44(1):33–46, 2004.

[7] M. Nunami and K. Nishihara. Numerical analysis of laser produced plasma expansion with large ion larmor radius via 3d pic simulation. *Journal of Plasma and Fusion Research*, 8, 2008.

[8] H. Oya. Origin of jovian decameter wave emissions-conversion from the electron cylotron plasma wave to the ordinary mode electromagnetic wave. *Planetary and Space Science*, 22(5):687–708, 1974.

[9] D. N. Smithe. Finite-difference time-domain simulation of fusion plasmas at radiofrequency time scales. *Physics of Plasmas*, 14(14):2537–2549, Apr. 2007.

[10] D. N. Smithe. Time domain modeling of plasmas at RF time-scales. *Journal of Physics: Conference Series*, 78(1):012069, 2007.

[11] T. Stix. *Waves in Plasmas*. American Institute of Physics, 1992.

[12] W. Tierens and D. De Zutter. BOR-FDTD subgridding based on finite element principles. *Journal of Computational Physics*, pages 4519–4535, 2011.

[13] W. Tierens and D. De Zutter. Finite-temperature corrections to the time-domain equations of motion for perpendicular propagation in nonuniform magnetized plasmas. *Physics of Plasmas*, 19:1–9, 2012.

[14] W. Tierens and D. De Zutter. An unconditionally stable time-domain discretization on cartesian meshes for the simulation of nonuniform magnetized cold plasma. *Journal of Computational Physics*, pages 5144–5156, 2012.

[15] J.L. Young. A full finite difference time domain implementation for radio wave propagation in a plasma. *Radio Science*, pages 1513–1522, 1994.

[16] Y. Yu. An E-J collocated 3-D FDTD model of electromagnetic wave propagation in magnetized cold plasma. *IEEE transactions on Antennas and Propagation*, 58(2):469–478, 2010.

[17] T. Zhou, Y. Gue, and C. Shu. Numerical study on Landau damping. *Physica D*, 157(4):322–333, 2001.

2

Warm and cold magnetized plasma descriptions

★ ★ ★

In this chapter we will construct and discuss time-domain equations describing cold [9, 14] and warm plasmas [13], starting from the hot plasma dielectric tensor [11, 2] which we introduce in section 2.2. In constructing the warm plasma descriptions, we use rational rather than polynomial approximations, avoiding some but not all problems associated with Finite-Larmor-Radius (FLR) approximations [1].

2.1 Cold, warm, and hot plasmas

In this context, the difference between cold, warm, and hot plasmas is the extent to which finite Larmor radius effects (effects of the thermal velocity) are taken into account. In cold plasmas, finite Larmor radius effects are neglected entirely (section 2.3). In hot plasmas, an exact mathematical solution is used, valid for arbitrarily large Larmor radii (section 2.2). In warm plasmas, a finite-order approximation in $\lambda = \frac{k_x^2 v_{th}^2}{2\Omega^2}$ is used (usually second-order [1]). Which of these is the proper description for a given plasma depends not only on the plasma parameters themselves (notably the temperature), but also on the kind of wave under consideration.

2.2 Hot plasma

The dielectric tensor for a spatially uniform hot Maxwellian plasma, with background magnetic field $\vec{B}_0$ along the z direction and propagation direction along the x direction, is [11, 2]

$$\epsilon_r = \begin{bmatrix} 1 & 0 & 0 \\ 0 & 1 & 0 \\ 0 & 0 & 1 \end{bmatrix} + \sum_s \sum_{n=-\infty}^{+\infty} \begin{bmatrix} t_{xx} & it_{xy} & t_{xz} \\ -it_{xy} & t_{yy} & it_{yz} \\ t_{xz} & -it_{yz} & t_{zz} \end{bmatrix} \tag{2.1}$$

where

$$t_{xx} = -\frac{\omega_s^2}{\omega^2}\frac{n^2}{\lambda_s}\mathcal{I}_n(\lambda_s)\exp(-\lambda_s)(-x_{0s}Z(x_{ns})) \tag{2.2}$$

$$t_{xy} = -\frac{\omega_s^2}{\omega^2}n(\mathcal{I'}_n(\lambda_s) - \mathcal{I}_n(\lambda_s))\exp(-\lambda_s)(-x_{0s}Z(x_{ns})) \tag{2.3}$$

$$t_{xz} = -\frac{1}{2}n_\parallel n_\perp \frac{\omega_s^2}{\omega\Omega_s}\frac{v_{th}^2}{c^2}\frac{n}{\lambda_s}\mathcal{I}_n(\lambda_s)\exp(-\lambda_s)(x_{0s}^2 Z'(x_{ns})) \tag{2.4}$$

$$t_{yy} = -\frac{\omega_s^2}{\omega^2}\left(\frac{n^2}{\lambda_s}\mathcal{I}_n(\lambda_s) - 2\lambda_s(\mathcal{I'}_n(\lambda_s) - \mathcal{I}_n(\lambda_s))\right)\exp(-\lambda_s)(-x_{0s}Z(x_{ns})) \tag{2.5}$$

$$t_{yz} = \frac{1}{2}n_\parallel n_\perp \frac{\omega_s^2}{\omega\Omega_s}\frac{v_{th}^2}{c^2}(\mathcal{I'}_n(\lambda_s) - \mathcal{I}_n(\lambda_s))\exp(-\lambda_s)(x_{0s}^2 Z'(x_{ns})) \tag{2.6}$$

$$t_{zz} = -\frac{\omega_s^2}{\omega^2}\mathcal{I}_n(\lambda_s)\exp(-\lambda_s)(x_{0s}Z'(x_{ns})) \tag{2.7}$$

The symbols used are

- v_{th}: the thermal velocity.
- $k_\parallel$: wavenumber along the confining magnetic field $\vec{B}_0$.
- $n_\parallel = k_\parallel \frac{c}{\omega}$
- $k_\perp$: wavenumber in the x-direction. Attempts to generalize to inhomogeneous cases will focus on inhomogeneity in this direction.
- $n_\perp = k_\perp \frac{c}{\omega}$
- $\lambda = \frac{k_x^2 v_{th}^2}{2\Omega^2}$: a second-order partial differential operator related to the Larmor radius, where ik_x corresponds to $\frac{\partial}{\partial x}$ in space.
- $\mathcal{I}_n$: modified Bessel functions of the first kind of order n. $\mathcal{I'}_n$ is the derivative of such a function.
- Ω_s : cyclotron frequency for particle specie s.

- ω_s : plasma frequency for particle specie s.
- $x_{ns} = \frac{\omega - n\Omega_s}{k_{\|} v_{th}}$.
- $Z(\zeta) = 2i\exp(-\zeta)\int_{-\infty}^{i\zeta}\exp(-t^2)dt$ is the plasma dispersion function.

The plasma dispersion function $Z(\zeta)$ may be expressed in closed form using either the error function $\mathrm{erf}(x) = 2/\sqrt{\pi}\int_0^x \exp(-t^2)dt$

$$Z(\zeta) = i\exp(-\zeta^2)\sqrt{\pi}(1 + \mathrm{erf}(i\zeta)) \tag{2.8}$$

or the Dawson integral $F(x) = \exp(-x^2)\int_0^x \exp(t^2)dt$

$$Z(\zeta) = i\exp(-\zeta^2)\sqrt{\pi} - 2F(\zeta) \tag{2.9}$$

2.3 Cold plasma

A "cold" plasma description may be obtained from the hot plasma description by letting $\lambda_s \to 0$, i.e. by assuming the Larmor radius to be very small. Then the dielectric tensor becomes

$$\epsilon_r = \begin{bmatrix} 1 & 0 & 0 \\ 0 & 1 & 0 \\ 0 & 0 & 1 \end{bmatrix} - \sum_s \begin{bmatrix} \frac{\omega_s^2}{\omega^2-\Omega^2} & \left(\frac{\Omega_s}{-i\omega}\right)\frac{\omega_s^2}{\omega^2-\Omega^2} & 0 \\ \left(\frac{\Omega_s}{i\omega}\right)\frac{\omega_s^2}{\omega^2-\Omega^2} & \frac{\omega_s^2}{\omega^2-\Omega^2} & 0 \\ 0 & 0 & \frac{\omega_s^2}{\omega^2} \end{bmatrix} \tag{2.10}$$

This dielectric tensor is equivalent to the time-domain constitutive differential equations for currents in the plasma associated with specie s [9, 10]

$$\frac{\partial \vec{J}_s}{\partial t} = \epsilon_0 \omega_s^2 \vec{E} - \vec{\Omega}_s \times \vec{J}_s \tag{2.11}$$

This equation has a straightforward physical interpretation. Since $\vec{J}_s = \vec{v}_s n_s q_s$

$$\frac{\partial \vec{v}_s n_s q_s}{\partial t} = \epsilon_0 \left(\frac{n_s q_s^2}{m_s \epsilon_0}\right)\vec{E} - \vec{\Omega}_s \times \vec{v}_s n_s q_s \tag{2.12}$$

$$\frac{\partial m_s \vec{v}_s n_s q_s}{\partial t} = n_s q_s^2 \vec{E} - \vec{\Omega}_s \times m_s \vec{v}_s n_s q_s \tag{2.13}$$

Noting that $\vec{\Omega}_s = q_s \vec{B}_0 / m_s$

$$m_s \frac{\partial \vec{v}_s}{\partial t} = q_s \vec{E} - q_s \vec{B}_0 \times \vec{v}_s \tag{2.14}$$

which is Newton's second law under the electrostatic force and the Lorentz force due to the background magnetic field $\vec{B}_0$.

That (2.10) follows from (2.11) is fairly straightforward. In the frequency domain

$$i\omega \vec{J}_s = \epsilon_0 \omega_s^2 \vec{E} - \vec{\Omega}_s \times \vec{J}_s \tag{2.15}$$

Interpreting the cross product as a matrix, with $\vec{\Omega}$ in the z direction, (2.15) becomes

$$i\omega \vec{J}_s = \epsilon_0 \omega_s^2 \vec{E} - \begin{bmatrix} 0 & -\Omega & 0 \\ \Omega & 0 & 0 \\ 0 & 0 & 0 \end{bmatrix} \vec{J}_s \tag{2.16}$$

$$\begin{bmatrix} i\omega & -\Omega & 0 \\ \Omega & i\omega & 0 \\ 0 & 0 & i\omega \end{bmatrix} \vec{J}_s = \epsilon_0 \omega_s^2 \vec{E} \tag{2.17}$$

$$\vec{J}_s = \epsilon_0 \omega_s^2 \begin{bmatrix} i\omega & -\Omega & 0 \\ \Omega & i\omega & 0 \\ 0 & 0 & i\omega \end{bmatrix}^{-1} \vec{E} \tag{2.18}$$

Inserting this in Maxwell's equations

$$\epsilon_0 i\omega \vec{E} + \sum_s \vec{J}_s = i\omega\epsilon_0\epsilon_r \vec{E} = \frac{1}{\mu_0} \vec{\nabla} \times \vec{B} \tag{2.19}$$

$$\left(\epsilon_0 i\omega + \sum_s \epsilon_0 \omega_s^2 \begin{bmatrix} i\omega & -\Omega & 0 \\ \Omega & i\omega & 0 \\ 0 & 0 & i\omega \end{bmatrix}^{-1} \right) \vec{E} = i\omega\epsilon_0\epsilon_r \vec{E} \tag{2.20}$$

$$1 + \frac{1}{i\omega\epsilon_0} \sum_s \epsilon_0 \omega_s^2 \begin{bmatrix} i\omega & -\Omega & 0 \\ \Omega & i\omega & 0 \\ 0 & 0 & i\omega \end{bmatrix}^{-1} = \epsilon_r \tag{2.21}$$

$$1 - \sum_s \begin{bmatrix} \frac{\omega_s^2}{\omega^2-\Omega^2} & \left(\frac{\Omega_s}{-i\omega}\right) \frac{\omega_s^2}{\omega^2-\Omega^2} & 0 \\ \left(\frac{\Omega_s}{i\omega}\right) \frac{\omega_s^2}{\omega^2-\Omega^2} & \frac{\omega_s^2}{\omega^2-\Omega^2} & 0 \\ 0 & 0 & \frac{\omega_s^2}{\omega^2} \end{bmatrix} = \epsilon_r \tag{2.22}$$

which is precisely (2.10).

However, we would like to have a more general way of obtaining (2.11) from (2.10), hoping to obtain time-domain descriptions of more complicated materials whose behaviour approximates more closely that of hot plasma (2.2). We will do so in section 2.4.

It is possible to rescale the currents and electric and magnetic fields to obtain Maxwell's equations and the cold plasma constitutive equation (2.11) in a more convenient anti-symmetric form. To this end we introduce

$$\vec{\mathcal{B}} = \frac{1}{\sqrt{\mu_0}}\vec{B} \tag{2.23}$$

$$\vec{\mathcal{E}} = \sqrt{\epsilon_0}\vec{E} \tag{2.24}$$

$$\vec{\mathcal{J}}_s = \epsilon_0^{3/2}\omega_s\vec{J}_s \tag{2.25}$$

$$\frac{\partial \vec{\mathcal{B}}}{\partial t} = -c\vec{\nabla} \times \vec{\mathcal{E}} \tag{2.26}$$

$$\frac{\partial \vec{\mathcal{E}}}{\partial t} = -\sum_s \omega_s \vec{\mathcal{J}}_s + c\vec{\nabla} \times \vec{\mathcal{B}} \tag{2.27}$$

$$\frac{\partial \vec{\mathcal{J}}_s}{\partial t} = \omega_s \vec{\mathcal{E}} - \vec{\Omega}_s \times \vec{\mathcal{J}}_s \tag{2.28}$$

This anti-symmetric form relates to conservation laws: any linear system of differential equations

$$\frac{\partial}{\partial t}\vec{V} = m\vec{V} \tag{2.29}$$

where m may be a square matrix, has the solution

$$\vec{V}(t) = \exp(mt)\vec{V}(0) \tag{2.30}$$

in the sense of a matrix exponential, i.e. if λ is an eigenvalue of m with eigenvector v, then $\exp(\lambda)$ is an eigenvalue of $\exp(m)$ with the same eigenvector v. Thus, if m has only purely imaginary eigenvalues (a consequence of being anti-hermitian), then $\exp(m)$ has only eigenvalues of unit norm, and $\exp(mt)$ will neither decay to 0, nor diverge to ∞, as $t \to \infty$. When discretizing these equations to obtain equations which are useful for computation, we will attempt to preserve properties such as this. Often it will turn out that we can discretize the original equations (2.10), and find a discrete version of the rescalings (2.23)-(2.25). However, this is not always the case, see section 4.1.2.

Constitutive equations similar to (2.11) are not unique to plasmas. For example, in ferrites the magnetization can obey the Gilbert equation [8, 6]

$$\frac{\partial \vec{m}}{\partial t} = -\gamma \left(\mu \vec{M}_s \times \vec{h} - \vec{m} \times \mu \left(\vec{H}_0 + \vec{h}\right)\right) \tag{2.31}$$

$$\vec{\nabla} \times \vec{h} = \epsilon \frac{\partial \vec{E}}{\partial t} + \sigma \vec{E} \tag{2.32}$$

$$\vec{\nabla} \times \vec{E} = -\mu \frac{\partial \vec{h}}{\partial t} - \mu \frac{\partial \vec{m}}{\partial t} \tag{2.33}$$

where $\vec{M}_s$ is the saturation magnetization, $\vec{H}_0$ is a biasing background magnetic field, $\gamma \approx 1.761 s^{-1}T^{-1}$ is the gyromagnetic ratio of an electron, and μ and ϵ may be anisotropic.

2.4 Warm plasma

2.4.1 From dielectric tensors to time-domain descriptions

Maxwell's "macroscopic" equations are

$$\vec{\nabla} \times \vec{E} = -\frac{\partial \vec{B}}{\partial t} \tag{2.34}$$

$$\frac{1}{\mu_0} \vec{\nabla} \times \vec{B} = \frac{\partial \vec{D}}{\partial t} \tag{2.35}$$

$$\vec{D} = \epsilon_0 \epsilon_r \cdot \vec{E} \tag{2.36}$$

where ϵ_r is a 3×3 tensor.

In plasmas we generally have

$$\epsilon_r = 1 + \sum_{\text{specie } s} \epsilon_{r,s} \tag{2.37}$$

The 'microscopic' equivalent of (2.35) is

$$\frac{1}{\mu_0} \vec{\nabla} \times \vec{B} = \epsilon_0 \frac{\partial \vec{E}}{\partial t} + \sum_{\text{specie } s} \vec{J}_s \tag{2.38}$$

hence

$$\epsilon_0 \frac{\partial \vec{E}}{\partial t} + \sum_{\text{specie } s} \vec{J}_s = \frac{\partial \vec{D}}{\partial t} = \epsilon_0 \left(1 + \sum_{\text{specie } s} \epsilon_{r,s} \right) \cdot \frac{\partial \vec{E}}{\partial t} \tag{2.39}$$

$$\sum_{\text{specie } s} \vec{J}_s = \sum_{\text{specie } s} \epsilon_0 \epsilon_{r,s} \cdot \frac{\partial \vec{E}}{\partial t} \tag{2.40}$$

If currents in a material are given by

$$\vec{J}_s = \epsilon_0 \epsilon_{r,s} \cdot \frac{\partial \vec{E}}{\partial t} \tag{2.41}$$

then (2.40) holds and the dielectric tensor is given by (2.37).

The summation index in (2.37) need not be a specie index. In (2.2), for example, we can consider every term in the double summation individually.

Methods similar to this one have been used to model a variety of materials including Lorentz and Debeye materials [7], though usually only scalar (isotropic) dielectrics.

2.4.2 Perpendicular propagation ($k_{\|} = 0$) in warm plasmas

$\vec{E} \perp \vec{B}_0$ case

We want to construct constitutive equations for "warm" plasma as an approximation to full "hot" plasma (2.2). This approximation will be second-order in the Larmor radius, or first-order in $\lambda = \frac{k_x^2 v_{th}^2}{2\Omega^2}$. We start by considering only perpendicular propagation, $k_{\|} = 0$, and we consider the mode where $\vec{E} \perp \vec{B}_0$. Thus, we only need to use the 2×2 xy part of the dielectric tensor. Retaining only terms up to $|n| = 2$ because the $|n| > 2$ terms have zeros of order > 1 at $\lambda = 0$ and thus give no contribution to a first-order approximation, this first-order approximation in λ of the dielectric tensor becomes

$$\epsilon = \epsilon_0 \left(1 + \sum_s (p_0 + p_1 + p_2) \right) \tag{2.42}$$

$$p_0 = \begin{bmatrix} 0 & 0 \\ 0 & \frac{e^{-\lambda}\omega_p^2\left(-2\lambda^2\mathcal{I}_0(\lambda)+2\lambda^2\mathcal{I}_1(\lambda)\right)}{\omega^2\lambda} \end{bmatrix} \tag{2.43}$$

$$p_1 = \begin{bmatrix} -\frac{2e^{-\lambda}\omega_p^2\mathcal{I}_1(\lambda)}{\lambda(\omega^2-\Omega^2)} & -\frac{ie^{-\lambda}\omega_p^2\Omega(\mathcal{I}_0(\lambda)-2\mathcal{I}_1(\lambda)+\mathcal{I}_2(\lambda))}{\omega(\omega^2-\Omega^2)} \\ \frac{ie^{-\lambda}\omega_p^2\Omega(\mathcal{I}_0(\lambda)-2\mathcal{I}_1(\lambda)+\mathcal{I}_2(\lambda))}{\omega(\omega^2-\Omega^2)} & \frac{2e^{-\lambda}\omega_p^2\left(2\lambda^2\mathcal{I}_0(\lambda)-(1+2\lambda(1+\lambda))\mathcal{I}_1(\lambda)\right)}{\lambda(\omega^2-\Omega^2)} \end{bmatrix} \tag{2.44}$$

$$p_2 = \begin{bmatrix} -\frac{8e^{-\lambda}\omega_p^2\mathcal{I}_2(\lambda)}{\lambda(\omega^2-4\Omega^2)} & -\frac{4ie^{-\lambda}\omega_p^2\Omega(\mathcal{I}_1(\lambda)-2\mathcal{I}_2(\lambda)+\mathcal{I}_3(\lambda))}{\omega(\omega^2-4\Omega^2)} \\ \frac{4ie^{-\lambda}\omega_p^2\Omega(\mathcal{I}_1(\lambda)-2\mathcal{I}_2(\lambda)+\mathcal{I}_3(\lambda))}{\omega(\omega^2-4\Omega^2)} & \frac{4e^{-\lambda}\omega_p^2\left(\lambda^2\mathcal{I}_1(\lambda)-(2+\lambda(2+\lambda))\mathcal{I}_2(\lambda)\right)}{\lambda\left(\omega^2-4\Omega^2\right)} \end{bmatrix} \tag{2.45}$$

It would seem that the way to proceed is to make a Taylor-approximation of the p_i, interpret all $i\omega$ as $\frac{\partial}{\partial t}$ and use (2.41) to obtain a time-domain description. Alas, doing so does not result in a conservative (anti-hermitizable for all real k) set of equations. A more careful approach based on rational rather than Taylor approximations is needed.

In the $\lambda \to 0$ limit, only p_1 is nonzero. We will approximate p_0 and p_2 to first-order in λ (i.e. $a + b\lambda$, where $a = 0$ for p_0 and p_2). To start, p_1 is approximated in the same way:

$$p_1 = p_{1,0} + p_{1,1}\lambda + O(\lambda^2) \tag{2.46}$$

However, this approximation is modified as follows

$$p_{1,\text{approx}} = p_{1,0} + (1 - p_{1,1}p_{1,0}^{-1}\lambda)^{-1}p_{1,1}\lambda \tag{2.47}$$

$p_{1,\text{approx}}$ is the simplest rational expression which at $\lambda = 0$ obeys

$$p_{1,\text{approx}} = p_1 \tag{2.48}$$

$$\frac{\partial}{\partial\lambda}p_{1,\text{approx}} = \frac{\partial}{\partial\lambda}p_1 \tag{2.49}$$

and, at $\lambda = \infty$

$$p_{1,\text{approx}} = p_1 = 0 \tag{2.50}$$

Note that

$$p_{1,\text{approx}} i\omega = \left(\underbrace{i\omega \begin{bmatrix} (1+\lambda) & 0 \\ 0 & (1+3\lambda) \end{bmatrix}}_{\text{Corrected } \frac{\partial}{\partial t}} + \underbrace{\begin{bmatrix} 0 & (1+2\lambda)\Omega \\ -(1+2\lambda)\Omega & 0 \end{bmatrix}}_{\text{Self-interaction, no } \omega} \right)^{-1} \omega_p^2 \epsilon_0 \tag{2.51}$$

Thanks to this convenient factorisation, (2.41) used with $p_{1,\text{approx}}$ gives a fairly simple first-order (in t) differential equation

$$\begin{aligned} i\omega \begin{bmatrix} (1+\lambda) & 0 \\ 0 & (1+3\lambda) \end{bmatrix} \begin{bmatrix} J_{1,x} \\ J_{1,y} \end{bmatrix} = \omega_p^2 \epsilon_0 \begin{bmatrix} E_x \\ E_y \end{bmatrix} \\ - \begin{bmatrix} 0 & (1+2\lambda)\Omega \\ -(1+2\lambda)\Omega & 0 \end{bmatrix} \begin{bmatrix} J_{1,x} \\ J_{1,y} \end{bmatrix} \end{aligned} \tag{2.52}$$

Note that (2.51) has a matrix “numerator” of zeroth-order in ω and a matrix “denominator” of first order in ω, even though $p_1 i\omega$ itself contains numerators of second order and denominators of first order in ω. The problem of factorizing rational matrices into a matrix “numerator” and “denominator” with no common factors is known in control theory as coprime factorization [5]. If the numerator and denominator factors must be polynomial (as opposed to rational), it is known as “Polynomial right comprime factorization”, and algorithms to find such factorizations exist [15].

From p_0 and p_2, the following differential equations can be constructed

$$i\omega \begin{bmatrix} J_{2,x} \\ J_{2,y} \end{bmatrix} = \omega_p^2 \epsilon_0 \lambda \begin{bmatrix} E_x \\ E_y \end{bmatrix} - \begin{bmatrix} 0 & 2\Omega \\ -2\Omega & 0 \end{bmatrix} \begin{bmatrix} J_{2,x} \\ J_{2,y} \end{bmatrix} \tag{2.53}$$

$$i\omega J_{0,y} = 2\omega_p^2 \epsilon_0 \lambda E_y \tag{2.54}$$

In fact, the approximation (2.47) can also be obtained as follows:

$$p_{1,\text{approx}} = \left(T_{\lambda,1} \left[\left(p_{1,0} + p_{1,1}\lambda \right)^{-1} \right] \right)^{-1} \tag{2.55}$$

where $T_{\lambda,1}[f]$ is the first-order Taylor approximation in λ of f.

In [13], rational approximations for p_0 and p_2 were also constructed. Doing so slightly improves the behaviour of the lowest-order Bernstein root, but is not necessary for stability.

If we collect all fields in a single vector $V = [E_x, E_y, B_z, J_{2,x}, J_{2,y}, J_{1,x}, J_{1,y}, J_{0,y}]^T$, and replace $i\omega$ by $\frac{\partial}{\partial t}$ the resulting equations are

$$\frac{\partial}{\partial t} A_L V = A_R V \tag{2.56}$$

$$A_L = \begin{bmatrix} 1 & 0 & 0 & 0 & 0 & 0 & 0 & 0 \\ 0 & 1 & 0 & 0 & 0 & 0 & 0 & 0 \\ 0 & 0 & 1 & 0 & 0 & 0 & 0 & 0 \\ 0 & 0 & 0 & 1 & 0 & 0 & 0 & 0 \\ 0 & 0 & 0 & 0 & 1 & 0 & 0 & 0 \\ 0 & 0 & 0 & 0 & 0 & 1+\lambda & 0 & 0 \\ 0 & 0 & 0 & 0 & 0 & 0 & 1+3\lambda & 0 \\ 0 & 0 & 0 & 0 & 0 & 0 & 0 & 1 \end{bmatrix} \tag{2.57}$$

$$A_R = \begin{bmatrix} 0 & 0 & 0 & -1/\epsilon_0 & 0 & -1/\epsilon_0 & 0 & 0 \\ 0 & 0 & ik_x/(\epsilon_0\mu_0) & 0 & -1/\epsilon_0 & 0 & -1/\epsilon_0 & -1/\epsilon_0 \\ 0 & ik_x & 0 & 0 & 0 & 0 & 0 & 0 \\ \lambda\omega_p^2\epsilon_0 & 0 & 0 & 0 & -2\Omega & 0 & 0 & 0 \\ 0 & \lambda\omega_p^2\epsilon_0 & 0 & 2\Omega & 0 & 0 & 0 & 0 \\ \omega_p^2\epsilon_0 & 0 & 0 & 0 & 0 & 0 & -(1+2\lambda)\Omega & 0 \\ 0 & \omega_p^2\epsilon_0 & 0 & 0 & 0 & (1+2\lambda)\Omega & 0 & 0 \\ 0 & 2\lambda\omega_p^2\epsilon_0 & 0 & 0 & 0 & 0 & 0 & 0 \end{bmatrix} \tag{2.58}$$

$A_L^{-1} A_R$ becomes anti-hermitian after the rescaling (2.59), namely (2.60)

$$\begin{aligned} &\vec{\mathcal{E}} = \sqrt{\epsilon_0}\vec{E} && \vec{\mathcal{B}} = \frac{1}{\sqrt{\mu_0}}\vec{B} && \vec{\mathcal{J}}_2 = \frac{i}{\omega_p\sqrt{\epsilon_0}\sqrt{\lambda}}\vec{J}_2 \\ &\vec{\mathcal{J}}_{1,x} = \frac{\sqrt{1+\lambda}}{\omega_p\sqrt{\epsilon_0}}\vec{J}_{1,x} && \vec{\mathcal{J}}_{1,y} = \frac{\sqrt{1+3\lambda}}{\omega_p\sqrt{\epsilon_0}}\vec{J}_{1,y} && \vec{\mathcal{J}}_{0,y} = \frac{1}{\sqrt{2}\omega_p\sqrt{\epsilon_0}\sqrt{\lambda}}\vec{J}_{0,y} \end{aligned} \tag{2.59}$$

$$\begin{bmatrix} 0 & 0 & 0 & i\omega_p\sqrt{\lambda} & 0 & -\frac{\omega_p}{\sqrt{1+\lambda}} & 0 & 0 \\ 0 & 0 & ick_x & 0 & i\omega_p\sqrt{\lambda} & 0 & -\frac{\omega_p}{\sqrt{1+3\lambda}} & -\sqrt{2}\omega_p\sqrt{\lambda} \\ 0 & ick_x & 0 & 0 & 0 & 0 & 0 & 0 \\ i\omega_p\sqrt{\lambda} & 0 & 0 & 0 & -2\Omega & 0 & 0 & 0 \\ 0 & i\omega_p\sqrt{\lambda} & 0 & 2\Omega & 0 & 0 & 0 & 0 \\ \frac{\omega_p}{\sqrt{1+\lambda}} & 0 & 0 & 0 & 0 & 0 & -\frac{(1+2\lambda)\Omega}{\sqrt{1+\lambda}\sqrt{1+3\lambda}} & 0 \\ 0 & \frac{\omega_p}{\sqrt{1+3\lambda}} & 0 & 0 & 0 & \frac{(1+2\lambda)\Omega}{\sqrt{1+\lambda}\sqrt{1+3\lambda}} & 0 & 0 \\ 0 & \sqrt{2}\omega_p\sqrt{\lambda} & 0 & 0 & 0 & 0 & 0 & 0 \end{bmatrix} \tag{2.60}$$

$$\begin{bmatrix} 0 & 0 & 0 & \frac{ik_x v_{th}\omega_p}{\sqrt{2}\Omega} & 0 & -\omega_p + \frac{k_x^2 v_{th}^2\omega_p}{4\Omega^2} & 0 & 0 \\ 0 & 0 & ick_x & 0 & \frac{ik_x v_{th}\omega_p}{\sqrt{2}\Omega} & 0 & -\omega_p + \frac{3k_x^2 v_{th}^2\omega_p}{4\Omega^2} & \frac{ik_x v_{th}\omega_p}{\Omega} \\ 0 & ick_x & 0 & 0 & 0 & 0 & 0 & 0 \\ \frac{ik_x v_{th}\omega_p}{\sqrt{2}\Omega} & 0 & 0 & 0 & -2\Omega & 0 & 0 & 0 \\ 0 & \frac{ik_x v_{th}\omega_p}{\sqrt{2}\Omega} & 0 & 2\Omega & 0 & 0 & 0 & 0 \\ \omega_p - \frac{k_x^2 v_{th}^2\omega_p}{4\Omega^2} & 0 & 0 & 0 & 0 & 0 & -\Omega & 0 \\ 0 & \omega_p - \frac{3k_x^2 v_{th}^2\omega_p}{4\Omega^2} & 0 & 0 & 0 & \Omega & 0 & 0 \\ 0 & \frac{ik_x v_{th}\omega_p}{\Omega} & 0 & 0 & 0 & 0 & 0 & 0 \end{bmatrix} \tag{2.61}$$

This last expression is of little practical use because of the presence of (the Fourier-domain equivalent of) fractional differential operators. It can be Taylor-approximated in λ which removes all unpractical terms (2.61) but has detrimental effects on the large-λ behaviour of the associated dispersion relation.

The thus-obtained set of equations has certain advantages which make it more suited to time-domain simulations than the standard FLR approach, most notably the unconditional stability and relatively well-behaved Bernstein root (figure 2.1), but it also shares some of the problems. As Brambilla [1] writes

> *Even more important is, however, the fact that the system of ordinary differential wave equations thus obtained is not uniquely defined, since there is no way of knowing the correct position of space derivatives with respect to space-dependent equilibrium quantities in the hot plasma terms.*

Indeed, the dielectric tensor (2.2) was obtained assuming uniform plasma, and therefore does not contain information about the physics in the spatially non-uniform case. No approach which starts from this dielectric tensor will give information about non-uniform physics.

Of course, starting from the Vlasov equation itself which does contain the non-uniform physics, rigorous non-uniform FLR descriptions can and have been constructed [1, 4, 12]. Attempts have also been made to derive a dielectric tensor for non-uniform plasmas [16]. In this work, we used the following approach

$$\begin{array}{ccccc} \text{Vlasov equation} & \rightarrow & \text{Dielectric tensor} = f(k,\omega) & \rightarrow & \text{Time-domain} \\ & & \text{(discards non-uniform physics)} & & \text{description} \end{array}$$

Some information about the non-uniform operator ordering may afterwards be obtained from e.g. energy considerations, but that does not suffice for a unique description.

An alternative approach which does not use the dielectric tensor, and does not discard the non-uniform physics, would look as follows

$$\begin{array}{ccccc} \text{Vlasov equation} & \rightarrow & \text{rigorous FLR approximation} & \rightarrow & \text{Time-domain} \\ & & \text{(keeps non-uniform physics)} & & \text{description (???)} \end{array}$$

To what extent obtaining time-domain descriptions from these rigorous FLR approximations is feasible, and if so, what sort of time-domain descriptions follow from them, are questions which are not explored in this work.

$\vec{E} \parallel \vec{B}_0$ case

The $\vec{E} \parallel \vec{B}_0$ case was not discussed in [13]. Not surprisingly, it too can be constructed from (2.41), and it too requires some rational approximations in order to guarantee unconditional stability.

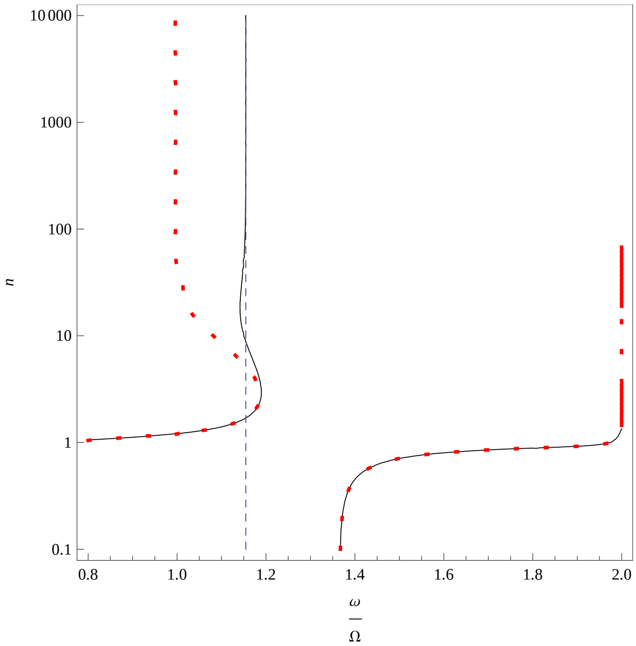

Figure 2.1: Continuous dispersion relation for hot plasma (red dotted) and warm plasma ((2.57)-(2.58), black). At high n, the Bernstein root approximates $\omega/\Omega = 2/\sqrt{3} \approx 1.15$, as opposed to $\omega/\Omega = 1$ in the exact case.

To first order in λ, the zz term of the dielectric tensor is

$$\epsilon_{zz} = p_0 + p_1 \tag{2.62}$$

$$p_0 = \frac{\omega_p^2(-1+\lambda)}{\omega^2} \tag{2.63}$$

$$p_1 = -\frac{\omega_p^2\lambda}{\omega^2 - \Omega^2} \tag{2.64}$$

p_0 gives rise to (Taylor approximation)

$$i\omega j_0 = \omega_p^2(1-\lambda)\epsilon_0\vec{E}_z \tag{2.65}$$

which should be replaced by a rational approximation as in (2.47), see figure 2.2

$$j_0 = \left(-\frac{\omega_p^2}{\omega^2} + \frac{\omega_p^2\lambda}{\omega^2(1+\lambda)}\right) i\omega\epsilon_0\vec{E}_z \tag{2.66}$$

$$i\omega(1+\lambda)j_0 = \omega_p^2\epsilon_0\vec{E}_z \tag{2.67}$$

(It is precisely the presence of the always-positive $1+\lambda$ in (2.67) as opposed to $1-\lambda$ in (2.65) which will guarantee stability even at high λ. In the anti-hermitizing transformation (2.76), it will give rise to always-real $\sqrt{1+\lambda}$ terms as opposed to possibly-complex $\sqrt{1-\lambda}$ terms which would occur otherwise).

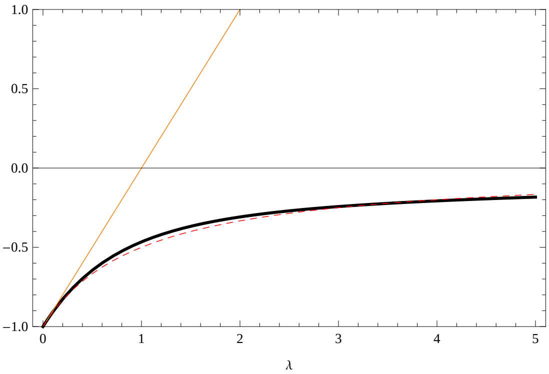

Figure 2.2: Exact (black), Taylor (orange), and rational (red dashed) approximation to ϵ_{zz} at $n=0$

p_1 gives rise to

$$i\omega\left(1+\frac{\Omega^2}{(i\omega)^2}\right) j_1 = \omega_p^2\lambda\epsilon_0\vec{E}_z \tag{2.68}$$

The quantities in brackets correspond in time-domain to j_1 and $\int dt \int^t j_1(\tau)d\tau$.

Let us group the degrees of freedom as $V=[\vec{B}_y,\vec{E}_z,j_0,\int dt\int^t j_1(\tau)d\tau,\int j_1 dt, j_1]$. Then

$$i\omega A_L V = A_R V \tag{2.69}$$

$$A_L = \begin{bmatrix} 1 & 0 & 0 & 0 & 0 & 0 \\ 0 & 1 & 0 & 0 & 0 & 0 \\ 0 & 0 & 1+\lambda & 0 & 0 & 0 \\ 0 & 0 & 0 & 1 & 0 & 0 \\ 0 & 0 & 0 & 0 & 1 & 0 \\ 0 & 0 & 0 & \Omega^2 & 0 & 1 \end{bmatrix} \tag{2.70}$$

$$A_R = \begin{bmatrix} 0 & ik & 0 & 0 & 0 & 0 \\ \frac{ik}{\mu_0\epsilon_0} & 0 & -1/\epsilon_0 & 0 & 0 & -1/\epsilon_0 \\ 0 & \epsilon_0\omega_p^2 & 0 & 0 & 0 & 0 \\ 0 & 0 & 0 & 0 & 1 & 0 \\ 0 & 0 & 0 & 0 & 0 & 1 \\ 0 & \epsilon_0\omega_p^2\lambda & 0 & 0 & 0 & 0 \end{bmatrix} \tag{2.71}$$

As usual, we need to verify the systems' conservativity by constructing an anti-hermitizing transformation for $A_L^{-1}A_R$.

$$A_L^{-1}A_R = \begin{bmatrix} 0 & ik & 0 & 0 & 0 & 0 \\ \frac{ik}{\epsilon_0\mu_0} & 0 & -1/\epsilon_0 & 0 & 0 & -1/\epsilon_0 \\ 0 & \frac{\omega_p^2\epsilon_0}{1+\lambda} & 0 & 0 & 0 & 0 \\ 0 & 0 & 0 & 0 & 1 & 0 \\ 0 & 0 & 0 & 0 & 0 & 1 \\ 0 & \omega_p^2\epsilon_0\lambda & 0 & 0 & -\Omega^2 & 0 \end{bmatrix} \tag{2.72}$$

After this multiplication by A_L^{-1}, we see that the $\int dt \int^t j_1(\tau)d\tau$ degree of freedom is not needed (there is no equation which depends on it, the 4th column of (2.72) is 0). We reduce the degrees of freedom to $V = [\vec{B}_y, \vec{E}_z, J_{0,z}, \int J_{1,z}dt, J_{1,z}]$. Now we have

$$A_L^{-1}A_R = \begin{bmatrix} 0 & ik & 0 & 0 & 0 \\ \frac{ik}{\epsilon_0\mu_0} & 0 & -1/\epsilon_0 & 0 & -1/\epsilon_0 \\ 0 & \frac{\omega_p^2\epsilon_0}{1+\lambda} & 0 & 0 & 0 \\ 0 & 0 & 0 & 0 & 1 \\ 0 & \omega_p^2\epsilon_0\lambda & 0 & -\Omega^2 & 0 \end{bmatrix} \tag{2.73}$$

$$A_L = \begin{bmatrix} 1 & 0 & 0 & 0 & 0 \\ 0 & 1 & 0 & 0 & 0 \\ 0 & 0 & 1+\lambda & 0 & 0 \\ 0 & 0 & 0 & 1 & 0 \\ 0 & 0 & 0 & 0 & 1 \end{bmatrix} \tag{2.74}$$

$$A_R = \begin{bmatrix} 0 & ik & 0 & 0 & 0 \\ \frac{ik}{\epsilon_0\mu_0} & 0 & -1/\epsilon_0 & 0 & -1/\epsilon_0 \\ 0 & \omega_p^2\epsilon_0 & 0 & 0 & 0 \\ 0 & 0 & 0 & 0 & 1 \\ 0 & \omega_p^2\epsilon_0\lambda & 0 & -\Omega^2 & 0 \end{bmatrix} \tag{2.75}$$

Now the desired anti-hermitizing transformation is fairly straightforward

$$\begin{array}{ll} \vec{\mathcal{E}}_z = \sqrt{\epsilon_0}\vec{E}_z & \vec{\mathcal{B}}_y = \frac{1}{\sqrt{\mu_0}}\vec{B}_y \quad \mathcal{J}_0 = \frac{\sqrt{1+\lambda}}{\omega_p\sqrt{\epsilon_0}}j_0 \\ \int \mathcal{J}_1 dt = \frac{\Omega}{\omega_p\sqrt{\epsilon_0}\sqrt{\lambda}}\int j_1 dt & \mathcal{J}_1 = \frac{1}{\omega_p\sqrt{\epsilon_0}\sqrt{\lambda}}j_1 \end{array} \tag{2.76}$$

2.4.3 Analysis of system size

$\vec{E} \perp \vec{B}_0$ case

For the mode where $k_{\|} = 0$ and $\vec{E} \perp \vec{B}_0$, the cold plasma description of section 2.3 yields

$$i\omega \begin{bmatrix} \mathcal{E}_x \\ \mathcal{E}_y \\ \mathcal{B}_z \\ \mathcal{J}_x \\ \mathcal{J}_y \end{bmatrix} = \underbrace{\begin{bmatrix} 0 & 0 & 0 & -\omega_p & 0 \\ 0 & 0 & ikc & 0 & -\omega_p \\ 0 & ikc & 0 & 0 & 0 \\ \omega_p & 0 & 0 & 0 & -\Omega \\ 0 & \omega_p & 0 & \Omega & 0 \end{bmatrix}}_{5\times 5} \begin{bmatrix} \mathcal{E}_x \\ \mathcal{E}_y \\ \mathcal{B}_z \\ \mathcal{J}_x \\ \mathcal{J}_y \end{bmatrix} \tag{2.77}$$

which involves a 5 × 5 matrix. This means that at any given k, 5 waves are supported (5 possible ω). Indeed, the eigenvalues of this matrix are precisely the 5 possible $i\omega$. These ω are symmetric around 0 : if ω if a solution, so is $-\omega$. The 5 solutions correspond to

- One uninteresting static solution (the full electro- and magneto-static solutions cannot be described using only Maxwell's "dynamic" equations (Ampère's and Faraday's laws), the static equations (Gauss' laws) are also needed. In numerical descriptions of wave phenomena, these last equations are often omitted, and static solutions, if there are any, do not generally correspond to true physical phenomena [3].)
- Four electrodynamic solutions, two at negative and two at positive ω

This is precisely what one would expect.

In the warm case (2.57)-(2.58), this matrix is 8 × 8, and we should investigate just what these 8 solutions are. If we set $v_{th} = 0$ in (2.57)-(2.58), the following solutions exist

- A double root at $\omega = 0$
- Four electrodynamic solutions, the same as in the cold plasma case
- A solution at $\omega = \pm 2\Omega$ (independent of k)

In figure 2.3, all these roots are shown.

When $v_{th} > 0$, the resonance at $(k \to \infty, \omega \to \sqrt{\omega_p^2 + \Omega^2})$ moves to $(k \to \infty, \omega \to \frac{2\Omega}{\sqrt{3}})$, creating an (approximated) first-order Bernstein root (the exact behaviour is $(k \to \infty, \omega \to \Omega)$). The solution at $\omega = \pm 2\Omega$ approximates, at sufficiently small λ, the second-order Bernstein root but diverges to $(k \to \infty, \omega \to \infty)$, as opposed to the exact $(k \to \infty, \omega \to 2\Omega)$.

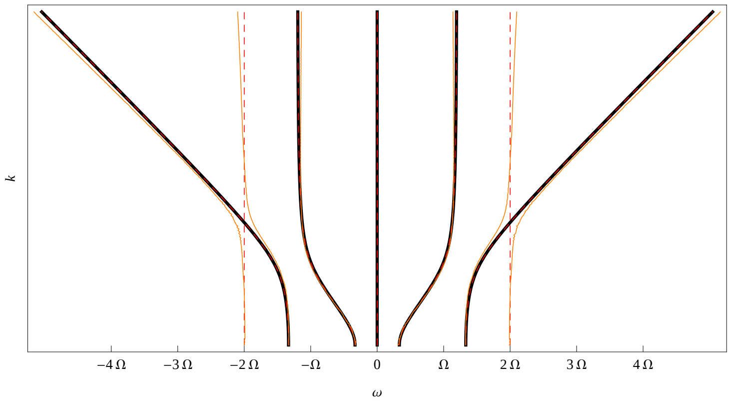

Figure 2.3: (ω, k)-roots in different approximations, $\vec{E} \perp \vec{B}_0$ case. Black: 5 cold roots. Red dashed: warm at $v_{th} = 0$, mimics cold but has additional roots at $\omega = \pm 2\Omega$. Orange: warm at $v_{th} > 0$.

$\vec{E} \parallel \vec{B}_0$ case

The warm description of section 2.4.2 yields a 5×5 matrix, corresponding to 5 possible frequencies at every k:

- A static solution
- The two cold plasma solutions (one at positive and one at negative ω)
- Two Bernstein roots with high-k limits at $\omega = \pm \frac{\sqrt{2}\Omega^2}{\sqrt{\frac{v_{th}^2 \omega_p^2 \epsilon}{c^2} + 2\Omega^2}}$

In the same case, cold plasma would require only a 3×3 matrix, with degrees of freedom $[B_z, E_y, J_y]$. These roots are shown in figure 2.4.

2.5 Conclusion

In this chapter we discussed the well-known cold plasma constitutive equation, and constructed "warm" plasma constitutive equations suitable for time-domain simulations, equations which are stable and capable of describing the lowest-order Bernstein root. We extended the results of [13] to include both the $\vec{E} \parallel \vec{B}_0$ and the $\vec{E} \perp \vec{B}_0$ case, though we are still limited to $k_{\parallel} = 0$. We expect that a more general result, valid to some nonzero order in $k_{\parallel}$, can be obtained by adding interaction terms between the $\vec{E} \parallel \vec{B}_0$ and the $\vec{E} \perp \vec{B}_0$ case.

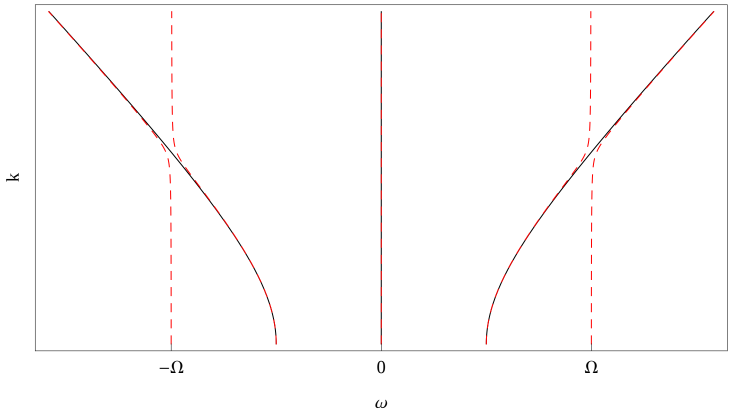

Figure 2.4: (ω, k)-roots in different approximations, $\vec{E} \parallel \vec{B}_0$ case. Black: 3 cold roots. Red dashed: 5 warm roots.

Bibliography

[1] M. Brambilla. Finite Larmor radius wave equations in tokamak plasmas in the ion cyclotron frequency range. *Plasma Physics and Controlled Fusion*, 31(5):123–151, 1989.

[2] M. Brambilla. *Kinetic theory of plasma waves*. Clarendon Press, 1998.

[3] R. A. Chilton. *H-, P- and T-refinement strategies for the finite-difference-time-domain (FDTD) method developed via finite-element (FE) principles*. PhD thesis, Ohio State University, 2008.

[4] P. Colestock and R. Kashuba. The theory of mode conversion and wave damping near the ion cyclotron frequency. *Nuclear fusion*, 23:763, 1983.

[5] P. Van Dooren. Rational and polynomial matrix factorization via recursive pole-zero cancellation. *Linear algebra and its applications*, 137:663–697, 1990.

[6] B. Guo and S. Ding. *Landau-Lifshitz equations*. World Scientific Publishing Co. Pte. Ltd., 2007.

[7] R. M. Joseph, S. C. Hagness, and A. Taflove. Direct time integration of Maxwell's equations in linear dispersive media with absorption for scattering and propagation of femtosecond electromagnetic pulses. *Optics Letters*, 16(18):1412–1414, May 1991.

[8] M. Nauta, M. Potter, and M. Okoniewski. FDTD on a Lebedev grid for analyzing magnetized ferrites. *IEEE APS conference paper*, pages 760–763, 2012.

[9] D. N. Smithe. Finite-difference time-domain simulation of fusion plasmas at radiofrequency time scales. *Physics of Plasmas*, 14(14):2537–2549, Apr. 2007.

[10] D. N. Smithe. Time domain modeling of plasmas at RF time-scales. *Journal of Physics: Conference Series*, 78(1):012069, 2007.

[11] T. Stix. *Waves in Plasmas*. American Institute of Physics, 1992.

[12] DG Swanson. Derivation of the mode conversion-tunneling equation from the vlasov equation. *Physics of Fluids*, 24(11):2035–2038, 1981.

[13] W. Tierens and D. De Zutter. Finite-temperature corrections to the time-domain equations of motion for perpendicular propagation in nonuniform magnetized plasmas. *Physics of Plasmas*, 19:1–9, 2012.

[14] W. Tierens and D. De Zutter. An unconditionally stable time-domain discretization on cartesian meshes for the simulation of nonuniform magnetized cold plasma. *Journal of Computational Physics*, pages 5144–5156, 2012.

[15] A. Varga. Computation of coprime factorizations of rational matrices. *Linear algebra and its applications*, 271(1):83–115, 1998.

[16] Luiz Fernando Ziebell and Ruth de Souza Schneider. The effective dielectric tensor for electromagnetic waves in inhomogeneous magnetized plasmas and the proper formulation in the electrostatic limit. *Brazilian journal of physics*, 34(3B):1211–1223, 2004.

3

Collocated approaches to the simulation of Maxwell's equations

★ ★ ★

Several approaches to collocated simulations of Maxwell's equations are presented and contrasted to the classical Yee cell, some relatively well-known (pseudospectral method), some lesser-known (Lebedev grids), and some developped by us. In this chapter we focus on Maxwell's equations in vacuum or scalar dielectrics, details on combining these methods with the plasma descriptions of chapter 2 will be discussed in chapter 4

3.1 The Yee cell

The Yee cell optimally exploits the structure of Maxwell's curl equations, resulting in a second-order accurate explicit discretisation: the extremely well-known Finite Difference Time Domain (FDTD) method [13]. It is a staggered structure which ensures every derivative (spatial and temporal) has a natural second-order accurate finite-difference analogon precisely where needed. In FDTD, Faraday's law is indeed enforced by obtaining the E-field spatial derivative by subtracting two spatially separated but simultaneous E-values and the B-field time-derivative by subtracting two temporarily separated but co-located B-values (figure 3.1, eq.

(3.1))

$$\frac{1}{\Delta_t}\left(B_z(x,t+\Delta_t)-B_z(x,t)\right)=\frac{1}{\Delta}\left(E_y(x+\Delta/2,t+\Delta_t/2)-E_y(x-\Delta/2,t+\Delta_t/2)\right) \tag{3.1}$$

A similar equation holds for Ampère's law.

Unfortunately, the Yee cell's staggered structure is ill-suited for differential equations involving cross products, which may require several components of a vector field at the same position. This fact has been pointed out in virtually all papers on the use of FDTD methods for magnetized plasmas [12, 15, 17, 18], and in several papers about other anisotropic materials [9]. The usual workaround involves some form of interpolation, in which case there are basically two possibilities

- Collocate all current and electric field components at Yee cell centers. The constitutive equation can be discretized without problems, but interpolations must be introduced in Maxwell's curl equations.

- Keep the Yee cell structure, and locate the current components at the same position as the corresponding electric field components (E_x and J_x, E_y and J_y, E_z and J_z). Then, Maxwell's curl equations can be discretized without problems, but the constitutive equations require some form of interpolation.

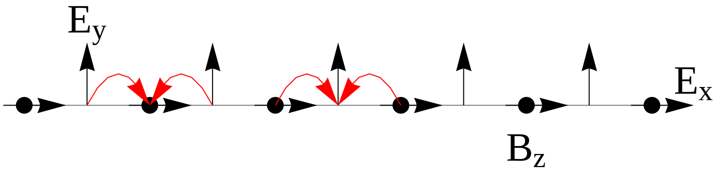

Figure 3.1: A typical 1D Yee grid. In vacuum, the E_x component would be zero and would not be shown on this figure, but in magnetized plasmas, it will be essential. Note how the staggered structure allows the central-difference derivative of E_y to be known at the B_z discretisation points and vice versa. Note also that the structure does *not* allow straightforward calculation of quantities which require all components of a field at the same position.

3.1.1 Stability

Like all time-domain methods, the FDTD method may be studied in terms of a time-stepping operator / amplification matrix. All discretized physical quantities, either electric field components, magnetic field components, currents, or any other quantities needed in the material description, are grouped together in a single large column vector V_t. Then, these quantities one time step in the future V_{t+1} can be described by

$$V_{t+1} = M V_t \tag{3.2}$$

where M is the time-stepping operator. It is usually desirable that the time-stepping operator is stable, i.e. that its eigenvalues lie on the unit circle in the complex plane. If there are losses, either due to lossy materials or due to radiation leaving the simulation region, some or all eigenvalues may be inside the unit circle. Only in rare cases (gain media) can the eigenvalues be outside the unit circle. If there are eigenvalues outside the unit circle, the associated solution will increase exponentially with time. Usually, this renders the results useless and it must be avoided [4, 2].

The FDTD method is explicit and conditionally stable : only if the time step Δ_t is sufficiently small will the eigenvalues be on the unit circle. In 1D ,

$$\Delta_t < \Delta / c \tag{3.3}$$

This is known as the Courant condition, or sometimes the Courant-Friedrichs-Lewy condition.

The eigenvalues relate to time-harmonic $\exp(i\omega t)$ solutions. If the system is in a state corresponding to an eigenvector $\mathcal{V}$ with eigenvalue λ, then the amount of time steps it takes to reach this state again is $2\pi/\arg(\lambda)$. The associated period is $2\pi\Delta_t/\arg(\lambda)$, the frequency is $\arg(\lambda)/(2\pi\Delta_t)$ and the angular frequency is $\omega = \arg(\lambda)/\Delta_t$. Clearly, λ values near 1, with small $\arg(\lambda)$ correspond to temporally well-resolved phenomena (many Δ_t per period, central difference approximation is well-justified), while λ values near -1 with large $\arg(\lambda)$ correspond to temporally ill-resolved phenomena (few Δ_t per period, central difference approximation is not well-justified).

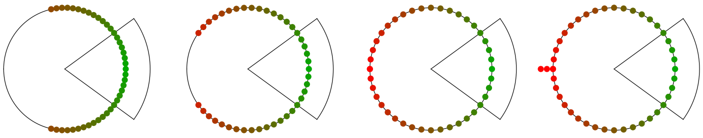

Figure 3.2: Typical behaviour of eigenvalues of the explicit FDTD time-stepping operator. When $\Delta_t < \Delta/c$ (left), the eigenvalues are on the unit circle away from -1. As Δ_t increases, some eigenvalues approach -1, then reach it, and eventually, when $\Delta_t > \Delta/c$, they leave the unit circle and the algorithm becomes unstable. The circle sector indicates temporally well-resolved eigenvalues, i.e. those with many Δ_t per period.

3.1.2 Dispersion relation in 1D

Wavenumber vs. frequency

Suppose

$$f(k,\omega)=0 \tag{3.4}$$

is the exact continuous dispersion relation of the medium, then

$$f(\sin(k\Delta/2)2/\Delta, \sin(\omega\Delta_t/2)2/\Delta_t)=0 \tag{3.5}$$

is the dispersion relation for the Yee cell discretisation. When the waves are well-resolved i.e. $k\Delta \ll \pi$ and $\omega\Delta_t \ll \pi$, the discrete dispersion relation approximates the continuous one: $\sin(k\Delta/2)2/\Delta \approx k$ and $\sin(\omega\Delta_t/2)2/\Delta_t \approx \omega$.

Eq. (3.5) only holds for sufficiently simple materials, notably classical dielectrics, where the Yee structure does not force the use of e.g. additional interpolations to include constitutive equations.

Vacuum solutions

Let

$$E_y = e_y \exp(ikx)\exp(-i\omega t) \tag{3.6}$$

$$B_z = b_z \exp(ikx)\exp(-i\omega t) \tag{3.7}$$

Using the discrete version of Faraday's law, we get

$$\frac{b_z}{e_y}=\frac{\Delta_t}{\Delta}\frac{\sin\left(\frac{\Delta k}{2}\right)}{\sin\left(\frac{\Delta_t\omega}{2}\right)}=\frac{k}{\omega}+O(\Delta^2)+O(\Delta_t^2) \tag{3.8}$$

In vacuum we have $\sin\left(\frac{\Delta k}{2}\right)\frac{2}{\Delta}=\frac{1}{c}\sin\left(\frac{\Delta_t\omega}{2}\right)\frac{2}{\Delta_t}$, which gives

$$k=\frac{2}{\Delta}\arcsin\left(\frac{\Delta}{c\Delta_t}\sin\left(\frac{\Delta_t\omega}{2}\right)\right)=\frac{\omega}{c}+O(\Delta^2)+O(\Delta_t^2) \tag{3.9}$$

combined with (3.8) we get

$$\frac{b_z}{e_y}=\frac{1}{c} \tag{3.10}$$

which is exact. In 1D FDTD in vacuum, the ratio of the amplitudes of the electric (E) and magnetic (B) fields equals the exact continuous result.

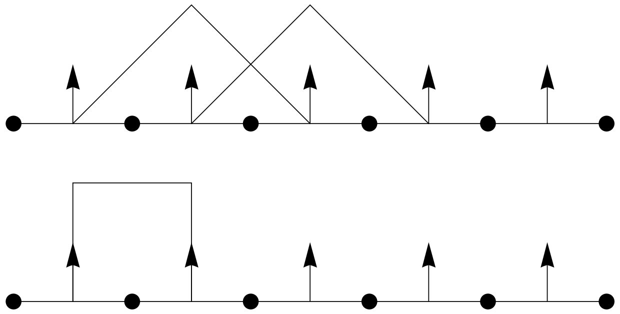

Figure 3.3: Top: Rooftop electric field basis-functions (which are also used as magnetic field test-functions). Bottom: pulse magnetic field basis-functions.

3.1.3 Finite element interpretation

Much insight into the FDTD method can be obtained by interpreting it as a mass-lumped finite element method (see also section 5.1). Specifically: the FDTD method can be derived as follows [2, 14]

- Write the electric fields as linear combinations of rooftop basis-functions.
- Write the magnetic fields as linear combinations of pulse basis-functions.
- The magnetic pulse basis-functions span the same space as the derivatives of the rooftop basis-functions. Consequently, Faraday's law can be satisfied exactly.
- The magnetic fields pulse basis-functions are insufficiently continuous to discretise Ampere's law. Therefore, Ampere's law is tested using electric field basis-functions as test-functions. If these integrals are "mass-lumped", i.e. if the integrals are approximated using trapezoidal integration with sampling points at the electric field discretisation points, the resulting equations are identical to the FDTD discretisation of Ampere's law.

The key property these basis- and test-functions must have is the "curl inclusion property", the magnetic field basis-functions must exactely span the vector-space spanned by the curl of the electric field basis-functions [2], which enables Faraday's law to be satisfied exactly. It is also this property which enables generalisation to non-Cartesian coordinate grids as in section 5.2.

3.2 The Pseudospectral method (PSTD)

One of the better-known time-domain discretisations of Maxwell's equations with collocated discretisation points is the pseudospectral time-domain method [6].

Spatial derivatives are approximated not by a local operator, as in the FDTD central-difference case, but by a global operator based on the discrete Fourier transform

$$\frac{\partial}{\partial x} f(x) = \mathfrak{F}^{-1}(i k_x \mathfrak{F}) \tag{3.11}$$

To the extent that $f(x)$ is band-limited $k_{max} = \pi/\Delta$, eq. (3.11) is exact. While in FDTD, it is necessary to ensure there are sufficiently many discretisation lengths per wavelength (typically about 10Δ per λ, though much more may be needed for accurate modeling of materials which support waves with strongly different phase velocities [6]) to get reliable results, in PSTD 2Δ per λ suffices. The time-stepping is usually done using the same second-order accurate finite-difference approximation as in FDTD.

3.2.1 Dispersion relation in 1D

If

$$f(k, \omega) = 0 \tag{3.12}$$

is the exact continuous dispersion relation of the medium, then

$$f(k, \sin(\omega \Delta_t/2)2/\Delta_t) = 0 \tag{3.13}$$

is the dispersion relation for the pseudo-spectral method. When the waves are well-resolved i.e. $k\Delta \leq \pi$ and $\omega\Delta_t \ll \pi$, the discrete dispersion relation approximates the continuous one: $k = k$ is exact and $\sin(\omega\Delta_t/2)2/\Delta_t \approx \omega$.

3.3 The Lebedev grid

The Lebedev grid has the staggered spatial structure of the Yee grid, but at every electric field discretisation point the full $\vec{E}$-vector is stored (as opposed to one component of $\vec{E}$), and at every magnetic field discretisation point the full $\vec{B}$-vector is stored. The update equations are based on standard FDTD central differences. For isotropic materials this method decouples into several independent Yee grids [9, 10], and care must be taken to excite all grids in the same way. In those types of materials which encourage the use of collocated methods (magnetized plasmas, ferrites), the grids tend to be at least weakly coupled. This approach is explicit in time and remains bound by the Courant condition. The discrete dispersion relation is similar to that of FDTD, but care must be taken to coalesce the fields on the Yee grids into a single result.

3.4 Upwind/downwind differencing

In [5, 7], another approach to collocated discretisations of Maxwell's equations is discussed. The electric and magnetic field vectors are spatially (but not temporaly) collocated. In this approach, a forward-difference operator is used to model the spatial derivative in Faraday's law, and a backward-difference operator is used for Ampère's law. While neither operator is second-order accurate, this combination turns out to be equivalent to a second-order accurate central difference on a finer grid [5]. Time stepping is done by the standard FDTD leapfrog technique.

3.5 A fully implicit method

3.5.1 Introduction

In [15], we constructed a method with the following properties

- Fully collocated, enabling the discretisation of the constitutive equations in their natural form, without undue interpolations.
- Stable even for $\Delta_t \gg \Delta/c$, enabling us to efficiently study phenomena whose wavelength is much smaller than the vacuum wavelength c/f at the same frequency. It has been pointed out repeatedly that the explicit FDTD Courant condition is prohibitively restrictive for simulating certain plasma waves [12, 1, 15], which justifies the use of partially or completely implicit methods.
- Involving only local interactions / sparse matrices.

A way to discretise Maxwell's equations on a collocated grid without thereby running into the Lebedev grid's (section 3.3) decoupling issues is to use an implicit approach *in space*. The high required stability naturally suggests an implicit approach in time as well. We end up with a method best explained by a figure (figure 3.4).

Let us start with a 1D-example, involving a plane wave propagating in the x direction. Maxwell's equations are

$$\frac{\partial E_z}{\partial t} = \frac{\partial B_y}{\partial x} \tag{3.14}$$

$$\frac{\partial B_y}{\partial t} = \frac{\partial E_z}{\partial x} \tag{3.15}$$

We will often prefer to use rescaled versions of Maxwell's equations, in which their symmetries are more clear (see also (2.23)-(2.28)). This will simplify stability arguments later.

$$\vec{\mathcal{E}} = \sqrt{\epsilon_0}\vec{E} \tag{3.16}$$

$$\vec{\mathcal{B}} = \frac{1}{\sqrt{\mu_0}}\vec{B} \tag{3.17}$$

$$\frac{\partial \mathcal{E}_z}{\partial t} = c\frac{\partial \mathcal{B}_y}{\partial x} \tag{3.18}$$

$$\frac{\partial \mathcal{B}_y}{\partial t} = c\frac{\partial \mathcal{E}_z}{\partial x} \tag{3.19}$$

For simplicity, we use a spatialy uniform 1D grid and locate the E_z discretisation points at $x = 0, \Delta, 2\Delta, \ldots$ (we will show in section 3.5.5 that a uniform grid size is not required for the method to work). The B_y discretisation points are the same points $x = 0, \Delta, 2\Delta, \ldots$. The central-difference spatial derivatives ($\frac{\partial B_y}{\partial x}$ and $\frac{\partial E_z}{\partial x}$) are then naturally located at half-integer points $x = \frac{1}{2}\Delta, \frac{3}{2}\Delta, \frac{5}{2}\Delta, \ldots$.

Similarly, in time, our discretisation points are located at $t = 0, \Delta_t, 2\Delta_t, \ldots$. The time derivatives are then located at half-integer points $t = \frac{1}{2}\Delta_t, \frac{3}{2}\Delta_t, \frac{5}{2}\Delta_t, \ldots$.

To enforce a discrete version of Maxwell's equations (3.14)-(3.15), we need to interpolate the temporal derivatives in space, and the spatial derivatives in time. Then, both end up at half-integer coordinates in both space and time. Figure 3.4 clarifies this.

It is neither necessary nor desirable to insert interpolators in directions along which the to-be-discretized scalar PDE does not contain derivatives. For example, in a 2D TM case (figures 3.5,3.6,3.7)

$$\frac{\partial}{\partial t}E_x = \frac{1}{\epsilon_0\mu_0}\frac{\partial}{\partial y}B_z \tag{3.20}$$

$$\frac{\partial}{\partial t}E_y = -\frac{1}{\epsilon_0\mu_0}\frac{\partial}{\partial x}B_z \tag{3.21}$$

$$\frac{\partial}{\partial t}B_z = \frac{\partial}{\partial y}E_x - \frac{\partial}{\partial x}E_y \tag{3.22}$$

the single magnetic field component relates to the two electric field components through a differential equation containing spatial derivatives in two directions, and correspondingly, its discretized version will contain interpolators in two spatial directions. The two electric field components, on the other hand, obey differential equations which contain only one spatial derivative, and their discretized versions need only contain an interpolator in this one spatial direction. Later, we will couple this method with the cold plasma constitutive equations from chapter 2, which contain no spatial derivatives at all, and the corresponding discretized equations will not contain any interpolators.

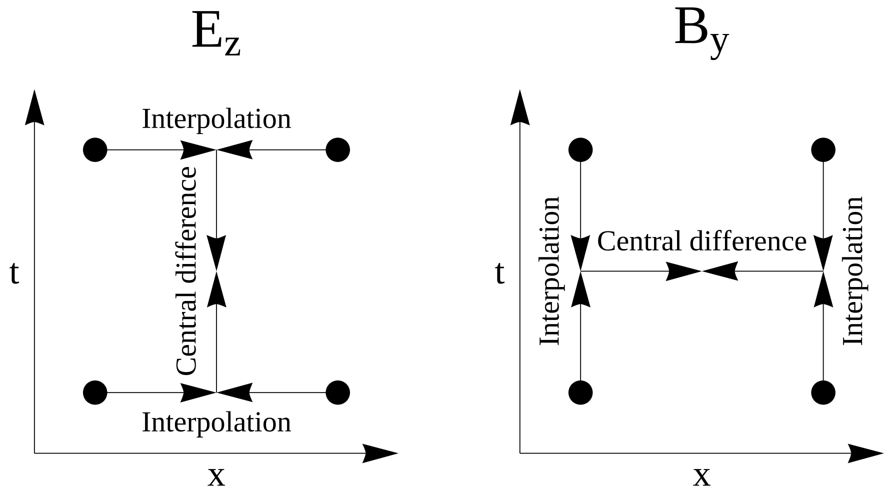

Figure 3.4: Discretisation of one of Maxwell's equations in 1D using a spatiotemporally implicit method.

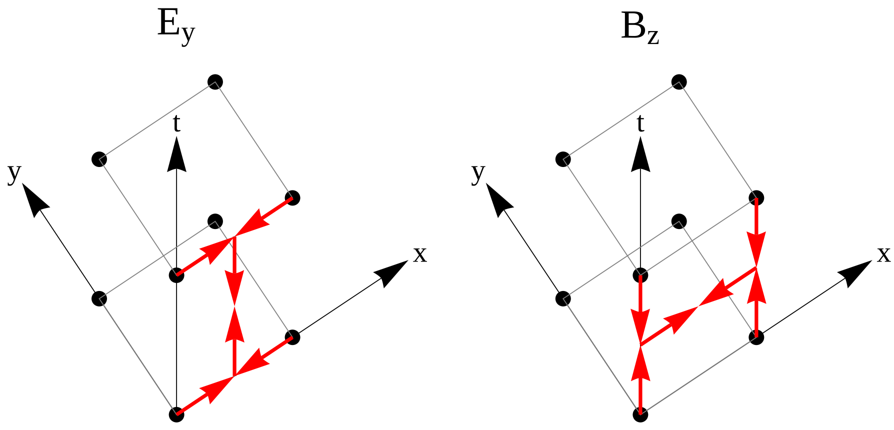

Figure 3.5: Discretisation of (3.20) in 2D. This equation contains only one spatial derivative and thus only one spatial interpolation. It is essentialy equivalent to the 1D case.

3.5.2 Practical expressions

All of Maxwell's equations contain temporal derivatives. If we collect all field components at time t in a single vector $V_t = [E_x, E_y, E_z, B_x, B_y, B_z]^T$, then the

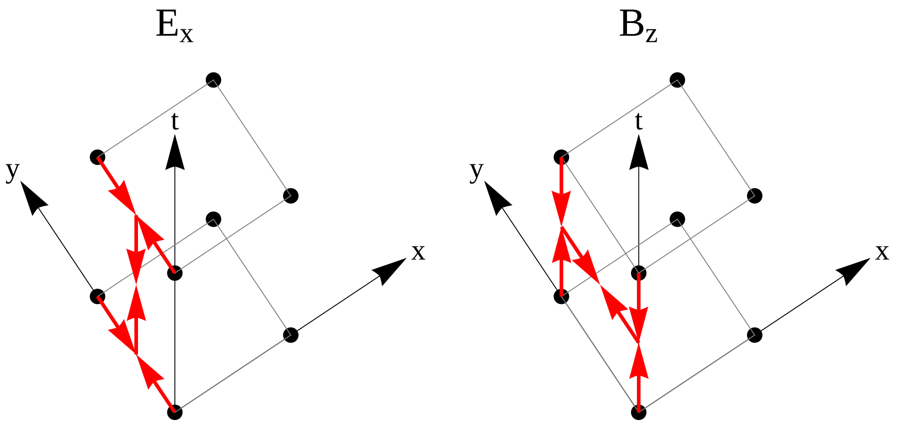

Figure 3.6: Discretisation of (3.21) in 2D. This equation contains only one spatial derivative and thus only one spatial interpolation. It is essentialy equivalent to the 1D case.

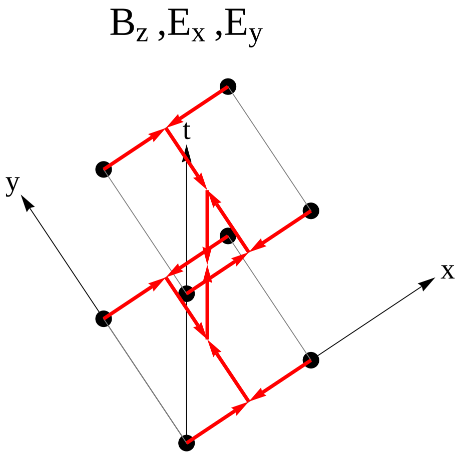

Figure 3.7: Only the third equation (3.22) in 2D contains 2 spatial derivatives and hence two spatial interpolators. Only this one differs essentially from the 1D case.

general equation for V_{t+1} as a function of V_t is

$$\frac{1}{\Delta_t} S_A \left(V_{t+1} - V_t\right) = \frac{1}{2} S_D \left(V_{t+1} + V_t\right) \tag{3.23}$$

where S_A is an interpolator which interpolates the fields to the desired positions, and S_D contains a mixture of spatial interpolators and spatial (finite-difference) differentiators.

A more explicit expression is

$$\left(\frac{1}{\Delta_t}S_A - \frac{1}{2}S_D\right)V_{t+1} = \left(\frac{1}{\Delta_t}S_A + \frac{1}{2}S_D\right)V_t \tag{3.24}$$

$$V_{t+1} = \left(S_A - \frac{\Delta_t}{2}S_D\right)^{-1}\left(S_A + \frac{\Delta_t}{2}S_D\right)V_t \tag{3.25}$$

Consider, for example, the 1D case (3.18)-(3.19), using periodic boundary conditions (N points, field values at position $x = N\Delta$ are equal to field values at position $x = 0$). In that case, the spatial interpolators and differentiators become

$$M_{int} = \frac{1}{2}\begin{bmatrix} 1 & 1 & 0 & 0 & 0 & \dots \\ 0 & 1 & 1 & 0 & 0 & \dots \\ & & \vdots & & & \ddots \\ 1 & 0 & 0 & \dots & 0 & 1 \end{bmatrix} \tag{3.26}$$

$$M_{der} = \frac{1}{\Delta}\begin{bmatrix} 1 & -1 & 0 & 0 & 0 & \dots \\ 0 & 1 & -1 & 0 & 0 & \dots \\ & & \vdots & & & \ddots \\ -1 & 0 & 0 & \dots & 0 & 1 \end{bmatrix} \tag{3.27}$$

The operators S_A and S_D are

$$S_A = \begin{bmatrix} M_{int} & 0 \\ 0 & M_{int} \end{bmatrix} \tag{3.28}$$

$$S_D = \begin{bmatrix} 0 & cM_{der} \\ cM_{der} & 0 \end{bmatrix} \tag{3.29}$$

If $\Delta = c\Delta_t$, the matrix $\left(S_A - S_D\frac{\Delta_t}{2}\right)$ is orthogonal: $\left(S_A - S_D\frac{\Delta_t}{2}\right)^{-1} = \left(S_A - S_D\frac{\Delta_t}{2}\right)^T$, and the time-stepping operator

$$\left(S_A - S_D\frac{\Delta_t}{2}\right)^{-1}\left(S_A + S_D\frac{\Delta_t}{2}\right) = \left(S_A - S_D\frac{\Delta_t}{2}\right)^T\left(S_A + S_D\frac{\Delta_t}{2}\right) \tag{3.30}$$

is an Nth root of unity:

$$\left(\left(S_A - S_D\frac{\Delta_t}{2}\right)^T\left(S_A + S_D\frac{\Delta_t}{2}\right)\right)^N = I_N \tag{3.31}$$

3.5.3 Dispersion relation in 1D

Wavenumber vs. frequency

If

$$f(k,\omega) = 0 \tag{3.32}$$

is the exact continuous dispersion relation of the medium, then

$$f(\tan(k\Delta/2)2/\Delta, \tan(\omega\Delta_t/2)2/\Delta_t) = 0 \tag{3.33}$$

is the dispersion relation for this fully implicit discretisation. When the waves are well-resolved i.e. $k\Delta \ll \pi$ and $\omega\Delta_t \ll \pi$, the discrete dispersion relation approximates the continuous one: $\tan(k\Delta/2)2/\Delta \approx k$ and $\tan(\omega\Delta_t/2)2/\Delta_t \approx \omega$.

(3.33) holds for all material descriptions found in chapter 2.

Vacuum solutions

Let

$$E_y = e_y \exp(ikx)\exp(-i\omega t) \tag{3.34}$$

$$B_z = b_z \exp(ikx)\exp(-i\omega t) \tag{3.35}$$

Using the discrete version of Faraday's law, we get

$$\frac{b_z}{e_y} = \frac{\Delta_t}{\Delta}\frac{\tan\left(\frac{\Delta k}{2}\right)}{\tan\left(\frac{\Delta_t\omega}{2}\right)} = \frac{k}{\omega} + O(\Delta^2) + O(\Delta_t^2) \tag{3.36}$$

In vacuum we have $\tan\left(\frac{\Delta k}{2}\right)\frac{2}{\Delta} = \frac{1}{c}\tan\left(\frac{\Delta_t\omega}{2}\right)\frac{2}{\Delta_t}$, which gives

$$k = \frac{2}{\Delta}\arctan\left(\frac{\Delta}{c\Delta_t}\tan\left(\frac{\Delta_t\omega}{2}\right)\right) = \frac{\omega}{c} + O(\Delta^2) + O(\Delta_t^2) \tag{3.37}$$

combined with (3.36) we get

$$\frac{b_z}{e_y} = \frac{1}{c} \tag{3.38}$$

which is exact. In the 1D fully implicit method in vacuum, the ratio of the amplitudes of the electric (E) and magnetic (B) fields equals the exact continuous result.

The discrete vacuum dispersion relation $\tan\left(\frac{\Delta k}{2}\right)\frac{2}{\Delta} = \frac{1}{c}\tan\left(\frac{\Delta_t\omega}{2}\right)\frac{2}{\Delta_t}$ has real (k,ω) solutions even when $c\Delta_t \gg \Delta$, and is thus stable even when Δ_t is much larger than the FDTD Courant limit. However, solutions in this case are inacurate. The Courant limit $c\Delta_t = \Delta$ is precisely the point where waves obeying the vacuum dispersion relation $k = \omega/c$ are equally well-resolved spatially and temporaly: the same amount of Δ per wavelength $\lambda = 2\pi/k$ and Δ_t per period $P = 2\pi/\omega$.

$$\left.\begin{aligned} k &= \omega/c \\ c\Delta_t &= \Delta \end{aligned}\right\} \implies \frac{\lambda}{\Delta} = \frac{P}{\Delta_t} \tag{3.39}$$

Approximation errors are dominated by $\min\left(\frac{\lambda}{\Delta}, \frac{P}{\Delta_t}\right)$, and in practice results are only considered acceptable if this number is above some lower bound, usually

10 but sometimes more. If $\frac{\lambda}{\Delta} \neq \frac{P}{\Delta_t}$, the wave is better resolved in space than in time or vice versa, but this does not correspond to improved accuracy since the error is still dominated by the worst resolved part. Because of this, deviating from the Courant limit is fairly pointless in vacuum, it becomes useful only when the wave phenomenon under consideration differs stronyly from the vacuum $k = \omega/c$ waves.

3.5.4 Image theory and boundary conditions

Under periodic boundary conditions, the interpolation and differentiation matrices are trivially square. With PEC boundary conditions, this is no longer so: some field components exist on the PEC boundary, others do not. The total amount of discretisation points for any given field component is no longer the same.

The proper way to enforce PEC boundary conditions is shown in figure 3.8. The interpolator for the electric field component, which has no corresponding discretisation point on the left PEC boundary, is

$$\frac{1}{2}\begin{bmatrix} 1 & 0 & 0 & 0 & 0 & \dots \\ 1 & 1 & 0 & 0 & 0 & \dots \\ 0 & 1 & 1 & 0 & 0 & \dots \\ & & \vdots & & & \ddots \\ 0 & 0 & 0 & \dots & 1 & 1 \end{bmatrix} \tag{3.40}$$

which is square and conveniently lower-triangular. There is no interpolation towards the right PEC boundary (where the field is zero anyway). The interpolator for the magnetic field component, which does have a discretisation point on the left PEC boundary, is

$$\frac{1}{2}\begin{bmatrix} 1 & 1 & 0 & 0 & 0 & \dots \\ 0 & 1 & 1 & 0 & 0 & \dots \\ & & \vdots & & & \ddots \\ 0 & 0 & 0 & \dots & 1 & 1 \\ 0 & 0 & 0 & \dots & 0 & 2 \end{bmatrix} \tag{3.41}$$

which is square and conveniently upper-triangular. The last row corresponds to interpolation to the right PEC boundary, and is what we would get by assuming that the field extends symmetrically beyond the PEC boundary (i.e. by using image theory).

Note that, while (3.40) and (3.41) are both square, they do not have the same dimension. Two different, non-square, derivative operators must also be defined before we can write down the full time-stepping operator. The spatial derivative operator acting on the electric field is

$$\frac{1}{\Delta}\begin{bmatrix} 1 & 0 & 0 & 0 & 0 & \dots \\ -1 & 1 & 0 & 0 & 0 & \dots \\ & & \vdots & & & \ddots \\ 0 & 0 & 0 & \dots & -1 & 1 \\ 0 & 0 & 0 & \dots & 0 & -2 \end{bmatrix} \tag{3.42}$$

where the last row is obtained by assuming this electric field component is anti-symmetric w.r.t. the right PEC boundary - again an assumption justified by image theory. The spatial derivative operator acting on the magnetic field is

$$\frac{1}{\Delta}\begin{bmatrix} -1 & 1 & 0 & 0 & 0 & \dots \\ 0 & -1 & 1 & 0 & 0 & \dots \\ & & \vdots & & & \ddots \\ 0 & 0 & 0 & \dots & -1 & 1 \end{bmatrix} \tag{3.43}$$

Here, there is no derivative defined at the right PEC boundary, because there is no interpolated electric field there which needs to know this derivative, and because that derivative is zero anyway.

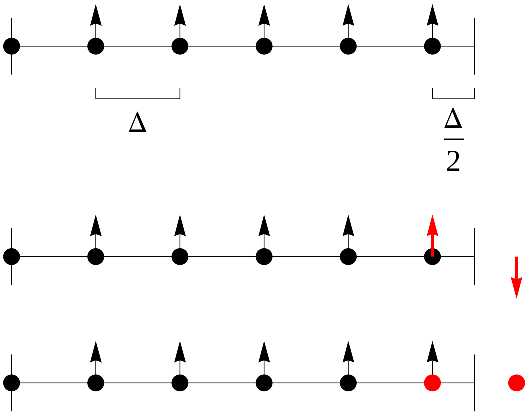

Figure 3.8: PEC boundary conditions. The length of the simulation domain is a half-integer times the discretisation length Δ. The field quantities outside the simulation domain, needed for both interpolation and differentiation, are obtained from symmetry considerations. Arrows represent an electric field component which is zero tangential to the PEC. Dots represent a magnetic field component which does not have to be zero at the PEC.

3.5.5 Stability proofs

Periodic boundary conditions

A proof of the stability of the discretisation put forward above was given in [15]. Here, we will present a somewhat more general case: consider a *non-uniform* 1D grid with n points and cell lengths Δ_i. The operators are

$$M_{int} = \frac{1}{2}\begin{bmatrix} 1 & 1 & 0 & 0 & 0 & \dots \\ 0 & 1 & 1 & 0 & 0 & \dots \\ & & \vdots & & & \ddots \\ 1 & 0 & 0 & \dots & 0 & 1 \end{bmatrix} \tag{3.44}$$

$$m_{\pm 1} = \begin{bmatrix} 1 & -1 & 0 & 0 & 0 & \dots \\ 0 & 1 & -1 & 0 & 0 & \dots \\ & & \vdots & & & \ddots \\ -1 & 0 & 0 & \dots & 0 & 1 \end{bmatrix} \tag{3.45}$$

$$m_\Delta = \mathrm{diag}(\Delta_1, \Delta_2, \dots, \Delta_n) \tag{3.46}$$

$$M_{der} = m_\Delta^{-1} m_{\pm 1} \tag{3.47}$$

Because M_{int} and $m_{\pm 1}$ are circulant, they are diagonalized in the $\mathfrak{F}$ basis. This basis is

$$\mathfrak{F}_{j,k} = \frac{1}{\sqrt{n}} \exp\left(\frac{-2\pi i}{n}(j-1)(k-1)\right) \tag{3.48}$$

where the factor $\frac{1}{\sqrt{n}}$ is chosen such that $\mathfrak{F}^{-1} = \mathfrak{F}^\dagger$, the inverse is the conjugate transpose.

The jth eigenvalue of a circulant $n \times n$ matrix with elements $m_{i,j}$ is

$$\lambda_j = \sum_{k=1}^{n} m_{1,k} \exp\left(\frac{2\pi i}{n} j(k-1)\right) \tag{3.49}$$

Therefore, the eigenvalues of M_{int} are $\lambda_j = \frac{1}{2}\left(1 + \exp(\frac{2\pi i}{n} j)\right)$ or $\exp(\frac{-j\pi i}{n})\lambda_j = \cos(\pi j/n)$ (Note that a zero eigenvalue exists only if n is even. M_{int} is invertible if n is odd.) The eigenvalues of $m_{\pm 1}$ are $\lambda_j = 1 - \exp(\frac{2\pi i}{n} j)$ or $\exp(\frac{-j\pi i}{n})\lambda_j = 2i\sin(\pi j/n)$.

$$m_{exp} = \mathrm{diag}(\exp(\frac{-0\pi i}{n}), \exp(\frac{-1\pi i}{n}), \dots, \exp(\frac{-(n-1)\pi i}{n})) \tag{3.50}$$

$$m_{cos} = \mathrm{diag}(\cos(0\pi/n), \cos(1\pi/n), \dots, \cos((n-1)\pi/n)) \tag{3.51}$$

$$m_{sin} = \mathrm{diag}(\sin(0\pi/n), \sin(1\pi/n), \dots, \sin((n-1)\pi/n)) \tag{3.52}$$

$$\mathfrak{F} M_{int} \mathfrak{F}^{-1} = m_{exp}^{-1} m_{cos} \tag{3.53}$$

$$\mathfrak{F} M_{\pm 1} \mathfrak{F}^{-1} = 2i(m_{exp}^{-1} m_{sin}) \tag{3.54}$$

m_{exp}, m_{cos} and m_{sin} are diagonal and thus they commute.

Consider $M_{int}^{-1} M_{der} = M_{int}^{-1} m_{\Delta}^{-1} m_{\pm 1}$ in the Fourier basis

$$\mathfrak{F} M_{int}^{-1} m_{\Delta}^{-1} m_{\pm 1} \mathfrak{F}^{-1} = m_{cos}^{-1} m_{exp} \mathfrak{F} m_{\Delta}^{-1} \mathfrak{F}^{-1} 2i (m_{exp}^{-1} m_{sin}) \tag{3.55}$$

Now apply a similarity transform : left-multiply by $m_{\Delta}^{1/2} \mathfrak{F}^{-1} m_{cos} m_{exp}^{-1}$, and right-multiply by its inverse

$$2i \left(m_{\Delta}^{-1/2} \mathfrak{F}^{-1} m_{sin} m_{cos}^{-1} \mathfrak{F} m_{\Delta}^{-1/2} \right) \tag{3.56}$$

Noting that $\mathfrak{F}^{-1} = \mathfrak{F}^{\dagger}$

$$\begin{aligned} &\left((2i) \left(m_{\Delta}^{-1/2} \mathfrak{F}^{\dagger} m_{sin} m_{cos}^{-1} \mathfrak{F} m_{\Delta}^{-1/2} \right) \right)^{\dagger} = \\ &(-2i) \left(m_{\Delta}^{-1/2} \mathfrak{F}^{\dagger} m_{sin} m_{cos}^{-1} \mathfrak{F} m_{\Delta}^{-1/2} \right) \end{aligned} \tag{3.57}$$

Thus, (3.56) is anti-hermitian, and its eigenvalues (and with it the eigenvalues of $M_{int}^{-1} M_{der}$) are purely imaginary. Call the basis that diagonalizes $M_{int}^{-1} M_{der}$, $\mathfrak{G}$. Unlike in the constant Δ case, we do not explicitly construct $\mathfrak{G}$, it suffices to know that it exists.

We need to show that the eigenvalues of the time-stepping operator (3.25) are on the unit circle. If the number of discretisation points is odd, S_A is invertible and we can write

$$\left(S_A - \frac{\Delta_t}{2} S_D \right)^{-1} \left(S_A + \frac{\Delta_t}{2} S_D \right) = \left(1 - \frac{\Delta_t}{2} S_A^{-1} S_D \right)^{-1} \left(1 + \frac{\Delta_t}{2} S_A^{-1} S_D \right) \tag{3.58}$$

Suppose we have an eigenvector $\mathcal{V}$ of $S_A^{-1} S_D$, with eigenvalue λ

$$S_A^{-1} S_D \mathcal{V} = \lambda \mathcal{V} \tag{3.59}$$

then

$$(1 + \frac{\Delta_t}{2} S_A^{-1} S_D) \mathcal{V} = (1 + \frac{\Delta_t}{2} \lambda) \mathcal{V} \tag{3.60}$$

$$(1 - \frac{\Delta_t}{2} S_A^{-1} S_D) \mathcal{V} = (1 - \frac{\Delta_t}{2} \lambda) \mathcal{V} \tag{3.61}$$

$$\left(1 - \frac{\Delta_t}{2} S_A^{-1} S_D \right)^{-1} \left(1 + \frac{\Delta_t}{2} S_A^{-1} S_D \right) \mathcal{V} = \frac{1 + \frac{\Delta_t}{2} \lambda}{1 - \frac{\Delta_t}{2} \lambda} \mathcal{V} \tag{3.62}$$

Clearly, $\frac{1 + \frac{\Delta_t}{2} \lambda}{1 - \frac{\Delta_t}{2} \lambda}$ is an eigenvalue of the time-stepping operator. It lies on the unit circle if λ is purely imaginary. To show that λ is indeed purely imaginary, we use the basis $\mathfrak{G}$ to turn $S_A^{-1}S_D$ into an anti-hermitian operator

$$\begin{bmatrix}\mathfrak{G} & 0\\ 0 & \mathfrak{G}\end{bmatrix}\begin{bmatrix}M_{int} & 0\\ 0 & M_{int}\end{bmatrix}^{-1}\begin{bmatrix}0 & cM_{der}\\ cM_{der} & 0\end{bmatrix}\begin{bmatrix}\mathfrak{G} & 0\\ 0 & \mathfrak{G}\end{bmatrix}^{-1} = \begin{bmatrix}0 & c\mathfrak{G}M_{int}^{-1}M_{der}\mathfrak{G}^{-1}\\ c\mathfrak{G}M_{int}^{-1}M_{der}\mathfrak{G}^{-1} & 0\end{bmatrix} \tag{3.63}$$

This is anti-hermitian because $\mathfrak{G}M_{int}^{-1}M_{der}\mathfrak{G}^{-1}$ is diagonal and purely imaginary, so the eigenvalues of $S_A^{-1}S_D$ are indeed purely imaginary.

This proof extends trivially to nonconstant ϵ_r and even nonconstant Δ_t.

In this proof, we assumed the amount of discretisation points is odd (equivalently, that the interpolator S_A is invertible). In 1D, this assumption is not needed: the relevant matrices remain invertible even when the interpolator itself is not. In 2D, however, configurations with periodic boundary conditions and an even number of discretisation points in both spatial directions give rise to a non-invertible system due to the existence of checkerboard-like configurations which are simultaneousely in the nullspace of S_A and S_D. In [15], we gave a 2D example that was odd×odd, in which case the required inverse does exist. This is not as problematic as it seems at first sight: as we pointed out in section 3.5.4, for PEC boundary conditions the interpolator (being block-diagonal with either upper- or lower-triangular blocks) is always invertible. Indeed, in section 3.5.5 we will see that configurations with PEC boundary conditions are always equivalent to twice as large configurations with periodic boundary conditions with odd amounts of discretisation points.

The possibility of running this algorithm on non-uniform grids at no Δ_t cost (still stable at arbitrarily large Δ_t), nor reduced approximation accuracy (still 2nd-order accurate interpolations and differentiations), stands in contrast to FDTD. In classical FDTD, non-uniform grids reduce the time step to the time step imposed by the smallest spatial step. This seems to be unavoidable without resorting to implicit techniques. No fully explicit provably stable multi-rate FDTD scheme seems to be known, despite [2]'s attempts to construct one (many existing multi-rate FDTD schemes are partly implicit [3, 11]). Furthermore, in FDTD, approximation accuracy is reduced where Δ changes [2, 8, 14], though in 1D this can be remedied by using a continuous mapping to a uniform grid [16].

PEC boundary conditions

Consider a vacuum configuration with periodic boundary conditions and an odd amount of discretisation points n and discretisation length Δ_x. On this configuration, we can consider solutions of the form $B_y \propto \cos(\alpha x)$, where α is such that B_y is symmetric w.r.t. both $x = 0$ and $x = (n/2)\Delta_x$, and $E_z \propto \sin(\alpha x)$, which is anti-symmetric w.r.t. both $x = 0$ and $x = (n/2)\Delta_x$. If these are eigenvectors of the periodic system (which remains to be shown), then we can exploit the symmetry properties to discard half of the degrees of freedom and replace them by the

PEC boundary conditions of 3.5.4, which would immediately imply stability of the thus-constructed system with PEC boundary conditions.

In vacuum, we can construct these PEC/standing wave eigenvectors from known periodic/propagating eigenvectors, for which $B_y \propto \exp(\pm i\alpha x)$, $E_z \propto \exp(\pm i\alpha x)$. A left- and a right-propagating eigenvector exist at the same eigenvalue $\lambda = \exp(i\omega\Delta_t)$ (as well as at $\lambda = \exp(-i\omega(\alpha)\Delta_t)$). There is a two-dimensional eigenspace associated with these eigenvalues, any element of which (any linear combination of these left- and right-propagating eigenvectors) is itself an eigenvector. Since the PEC boundary condition-obeying standing-wave solutions are linear combinations of left- and right-propagating solutions, they are indeed eigenvectors of the periodic system, which implies the stability of the PEC system.

3.5.6 A finite-element interpretation

Our method may be interpreted, like FDTD, as a mass-lumped finite element method. The basis-functions are rooftop functions centered on discretisation points. The test-functions are pulse-functions on cells.

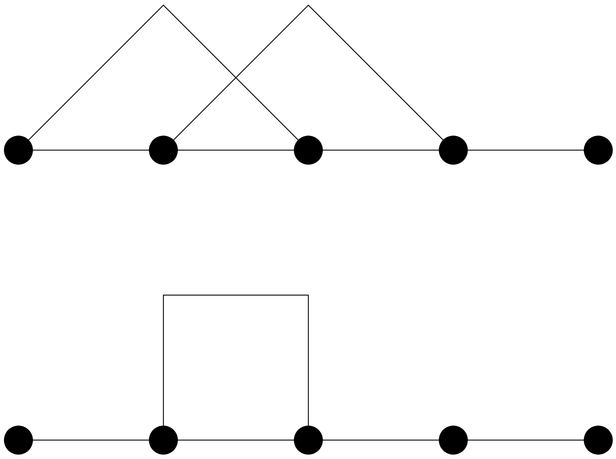

Figure 3.9: Basis- and test-functions for the finite-element interpretation of the fully implicit method.

Let us define the rooftop functions $R(x, x_0)$ as continuous piecewise linear functions which are 1 at $x = x_0$ and 0 when $x \leq x_0 - \varDelta$ or $x \geq x_0 + \varDelta$. Similarly, let the pulse functions $P(x, x_0)$ be piecewise constant, 1 when $x \in [x_0, x_0 + \varDelta]$, and 0 otherwise.

Next, consider a field expressed as a linear combination of basis-functions, i.e. a linear combination of $R(x, x_0)$

$$f = \sum_i \alpha_i R(x, i\Delta) \tag{3.64}$$

"testing", i.e. multiplying by a test-function P and integrating over space, gives

$$\begin{aligned}
\int P(x, j\Delta) f \, dx &= \int P(x, j\Delta) \sum_i \alpha_i R(x, i\Delta) dx && (3.65)\\
&= \int P(x, j\Delta) \sum_{i=j,j+1} \alpha_i R(x, i\Delta) dx && (3.66)\\
&= \frac{\Delta}{2}(\alpha_j + \alpha_{j+1}) && (3.67)
\end{aligned}$$

which corresponds, up to the factor Δ which will be divided away later, to an interpolation.

Similarly, testing a derivative of a field expressed as a linear combination of basis-functions will give us the classical central-difference derivative

$$\begin{aligned}
f &= \sum_i \alpha_i R(x, i\Delta) && (3.68)\\
\frac{\partial f}{\partial x} &= \sum_i \frac{\alpha_i}{\Delta} \left(P(x, i\Delta) - P(x, (i+1)\Delta)\right) && (3.69)\\
\int P(x, j\Delta) \frac{\partial f}{\partial x} dx &= \int P(x, j\Delta) \sum_i \frac{\alpha_i}{\Delta} \left(-P(x, i\Delta) + P(x, (i-1)\Delta)\right) dx && (3.70)\\
&= \int P(x, j\Delta) \sum_{i=j,j+1} \frac{\alpha_i}{\Delta} \left(P(x, i\Delta) - P(x, (i+1)\Delta)\right) dx && (3.71)\\
&= \alpha_{i+1} - \alpha_i && (3.72)
\end{aligned}$$

which corresponds to a derivative (the missing factor $1/\Delta$ will be provided when we divide by Δ later).

To put this all together, we take one of Maxwell's equations (3.14)

$$\frac{\partial E_z}{\partial t} = \frac{\partial B_y}{\partial x} \tag{3.73}$$

We expand the fields in rooftop basis-functions in space and time

$$\frac{\partial}{\partial t} \sum_j \sum_i e_{i,j} R(x, i\Delta) R(t, j\Delta_t) = \frac{\partial}{\partial x} \sum_j \sum_i b_{i,j} R(x, i\Delta) R(t, j\Delta_t) \tag{3.74}$$

and test with a test-function in space and time

$$\int P(x,k\Delta)P(t,l\Delta_t)\frac{\partial}{\partial t}\sum_j\sum_i e_{i,j}R(x,i\Delta)R(t,j\Delta_t)dxdt =$$
$$\int P(x,k\Delta)P(t,l\Delta_t)\frac{\partial}{\partial x}\sum_j\sum_i b_{i,j}R(x,i\Delta)R(t,j\Delta_t)dxdt \tag{3.75}$$

which gives

$$\Delta_x\left(\frac{1}{2}(e_{k,l+1}+e_{k+1,l+1})-\frac{1}{2}(e_{k,l}+e_{k+1,l})\right) =$$
$$\Delta_t\left(\frac{1}{2}(b_{k+1,l}+e_{k+1,l+1})-\frac{1}{2}(b_{k,l}+e_{k,l+1})\right) \tag{3.76}$$

dividing by $\Delta_x\Delta_t$ gives the expected expression

$$\frac{1}{\Delta_t}\left(\frac{1}{2}(e_{k,l+1}+e_{k+1,l+1})-\frac{1}{2}(e_{k,l}+e_{k+1,l})\right) =$$
$$\frac{1}{\Delta_x}\left(\frac{1}{2}(b_{k+1,l}+e_{k+1,l+1})-\frac{1}{2}(b_{k,l}+e_{k,l+1})\right) \tag{3.77}$$

3.6 Conclusion

In this chapter we discussed and generalized the discretisation of Maxwell's equation which we derived in [15]. The unconditional stability and collocated nature of this discretisation make it well-suited for modeling plasma-wave interactions as described in chapter 2. In chapter 4 we will combine this discretisation with these plasma descriptions and give numerical examples.

Bibliography

[1] K. Bowers. Implicit methods of solving the maxwell equations suitable for particle-in-cell simulation of low temperature plasmas. 2001. Available as `http://ptsg.berkeley.edu/~kbowers/doc/imp.pdf`.

[2] R. A. Chilton. *H-, P- and T-refinement strategies for the finite-difference-time-domain (FDTD) method developed via finite-element (FE) principles*. PhD thesis, Ohio State University, 2008.

[3] F. Collino, T. Fouquet, and P. Joly. Conservative space-time mesh refinement methods for the FDTD solution of Maxwell's equations. *Journal of Computational Physics*, pages 9–35, 2005.

[4] B. Denecker. *The subdomain FDTD method*. PhD thesis, Ghent University, 2003.

[5] R. Janaswamy and Y. Liu. An unstaggered colocated finite-difference scheme for solving time-domain maxwell's equations in curvilinear coordinates. *IEEE Transactions on Antennas and Propagation*, 45(11):1584–1591, 1997.

[6] T. Lee and S. Hagness. Pseudospectral time-domain methods for modeling optical wave propagation in second-order nonlinear materials. *Journal of the Optical Society of America*, 21(2):330–342, 2004.

[7] Y. Liu. Fourier analysis of numerical algorithms for the maxwell equations. *Journal of Computational Physics*, 124(68):396–416, 1999.

[8] P. Monk. Subgridding FDTD schemes. *Applied Computational Electromagnetics Journal*, 11(1):37–46, 1996.

[9] M. Nauta. FDTD method on a Lebedev grid for anisotropic materials. *IEEE APS conference paper*, 2012.

[10] M. Nauta, M. Potter, and M. Okoniewski. FDTD on a Lebedev grid for analyzing magnetized ferrites. *IEEE APS conference paper*, pages 760–763, 2012.

[11] S. Piperno. Symplectic local time-stepping in non-dissipative DGTD methods applied to wave propagation problems. *RAIRO Model Math. Anal. Numer*, pages 3–30, 2005.

[12] D. N. Smithe. Finite-difference time-domain simulation of fusion plasmas at radiofrequency time scales. *Physics of Plasmas*, 14(14):2537–2549, Apr. 2007.

[13] A. Taflove and S. Hagness. *Computational Electrodynamics: The Finite-Difference Time-Domain Method*. Artech House, 2005.

[14] W. Tierens and D. De Zutter. BOR-FDTD subgridding based on finite element principles. *Journal of Computational Physics*, pages 4519–4535, 2011.

[15] W. Tierens and D. De Zutter. An unconditionally stable time-domain discretization on cartesian meshes for the simulation of nonuniform magnetized cold plasma. *Journal of Computational Physics*, pages 5144–5156, 2012.

[16] M. Tong and V. Krozer. A non-uniform pseudo-spectral time domain (pstd) method in one-dimensional applications. *General Assembly of International Union of Radio Science*, 2002. Available as `http://www.ursi.org/Proceedings/ProcGA02/papers/p0393.pdf`.

[17] J.L. Young. A full finite difference time domain implementation for radio wave propagation in a plasma. *Radio Science*, pages 1513–1522, 1994.

[18] Y. Yu. An E-J collocated 3-D FDTD model of electromagnetic wave propagation in magnetized cold plasma. *IEEE transactions on Antennas and Propagation*, 58(2):469–478, 2010.

4

Numerical simulations of magnetized plasmas

★ ★ ★

This chapter contains most numerical results in this thesis. First, we combine the fully implicit collocated discretisation of Maxwell's equations from chapter 3 with the magnetized plasma constitutive differential equations from chapter 2. We also include numerical examples relating to the hybrid algorithm from chapter 5, which enables the FDTD calculation of transmission coefficients of very thin material layers without having to change Δ_t.

4.1 Time-stepping operator for cold plasma

4.1.1 Simplest case

As a first example, consider a plane wave propagating through a magnetized cold plasma with $\vec{k} \perp \vec{B}_0$. Specifically, consider the solution where $\vec{E}_{\|} = 0$ (the component of the electric field parallel to the background magnetic field). In that case, only two electric field components, one magnetic field component, and $2n_s$ current components play a role, where n_s is the amount of species.

With periodic boundary conditions and only one particle specie, the operators S_A

and S_D become

$$S_A = \begin{pmatrix} 1 & 0 & 0 & 0 & 0 \\ 0 & M_{int} & 0 & 0 & 0 \\ 0 & 0 & 1 & 0 & 0 \\ 0 & 0 & 0 & 1 & 0 \\ 0 & 0 & 0 & 0 & M_{int} \end{pmatrix} \tag{4.1}$$

$$S_D = \begin{pmatrix} 0 & 0 & \omega_p & 0 & 0 \\ 0 & 0 & 0 & M_{int}\omega_p & \frac{c}{\Delta}M_{der} \\ -\omega_p & 0 & 0 & \Omega & 0 \\ 0 & -\omega_p & -\Omega & 0 & 0 \\ 0 & \frac{c}{\Delta}M_{der} & 0 & 0 & 0 \end{pmatrix} \tag{4.2}$$

where M_{int} and M_{der} were defined in (3.26)-(3.27).

Here, we recognize the structure of the anti-symmetrized cold plasma equations (2.26)-(2.28). We also see that no spatial interpolation is used in those equations which contain no spatial derivatives (corresponding to the 1 blocks in S_A), which was pointed out in chapter 3.

4.1.2 A note on discretisation and anti-hermitisation

The matrices which encode the (possibly position-dependent) plasma frequency and cyclotron frequency, ω_p and Ω, can be obtained from the finite-element interpretation of section 3.5.6, i.e. by “testing” triangular basis-functions with triangular test-functions in the case of the constitutive equation, or by testing triangular basis-functions with pulse test-functions in the case of Ampères law. In [10], we “mass lumped” this operation, i.e. we used trapezoidal integration to approximate these integrals. By doing so, the matrices ω_p and Ω become diagonal, with their value $\Omega_{i,i}$ being the cyclotron frequency at the ith discretisation point.

As we pointed out in [10], this mass lumping is not necessary: (4.1)-(4.2) give rise to a stable set of equations when ω_p is real and symmetric, it need not be diagonal. However: suppose instead of starting from the anti-symmetrized cold plasma equations (2.26)-(2.28), we start from the non-rescaled cold plasma equation (2.11). We can discretize this equation and attempt to verify stability by contructing a rescaling to an anti-symmetric form after discretisation. This requires that $\vec{\Omega}\times$ commutes with ω_p, which is trivially true in the continuous case, also true when Ω and ω_p are diagonal (discretized using mass-lumping), but no longer true without mass lumping.

Let us order the degrees of freedom by position : $[E_{x,1}, E_{y,1}, E_{x,2}, E_{y,2}, \ldots]$. In the mass-lumped case, the question is “does (4.3) commute with (4.4)?”

$$\operatorname{blkdiag}\left(\begin{bmatrix} 0 & 0 & \Omega_1 \\ 0 & 0 & 0 \\ -\Omega_1 & 0 & 0 \end{bmatrix}, \begin{bmatrix} 0 & 0 & \Omega_2 \\ 0 & 0 & 0 \\ -\Omega_2 & 0 & 0 \end{bmatrix}, \dots\right) \tag{4.3}$$

$$\operatorname{blkdiag}\left(\omega_{p,1} I_3, \omega_{p,2} I_3, \dots\right) \tag{4.4}$$

The answer is obviousely yes, because the scalar blocks of (4.4), being scalar, commute with everything.

In the non-lumped case on the other hand, the discrete ω_p becomes tridiagonal and is no longer guaranteed to commute with the discrete $\vec{\Omega}\times$. This is an example of what we pointed out in chapter 2 : that the possibility of constructing a rescaling to an anti-symmetric form in the continuous case does not guarantee the same possibility in the discretized equations, which is why we have tended to prefer taking care of the the anti-symmetrisation before the discretisation in [10, 9].

4.1.3 General case

The most general 1D wave propagation in magnetized cold plasmas is more complex. The wavevctor $\vec{k}$ need not be perpendicular to the background magnetic field and, in general, all components of the electric and magnetic field may be nonzero. Still in 1D, let x be the discretized direction , i.e. the direction in which the material parameters may change, and y be the direction perpendicular to the x direction such that $(\vec{x} \times \vec{y}) \cdot \vec{k} = 0$. Then we can write k using k_x, k_y nonzero and $k_z = 0$. The fields in general may then be written as linear combinations of $f_s(x)\sin(k_y y)$ and $f_c(x)\cos(k_y y)$. To fully modell this, we need to write the equations in $f_s(x)$ and $f_c(x)$, and discretize both. Thus, we will need 6 degrees of freedom per discretisation point per vectorfield (as opposed to the usual 3). The discretized Cartesian curl operator in this general case is

$$\vec{E} = [E_{s,x}, E_{s,y}, E_{s,z}, E_{c,x}, E_{c,y}, E_{c,z}]^T \tag{4.5}$$

$$\vec{\nabla}\times = \begin{bmatrix} 0 & 0 & 0 & 0 & 0 & -k_y \\ 0 & 0 & -M_{der} & 0 & 0 & 0 \\ 0 & M_{der} & 0 & M_{int}k_y & 0 & 0 \\ 0 & 0 & k_y & 0 & 0 & 0 \\ 0 & 0 & 0 & 0 & 0 & -M_{der} \\ -M_{int}k_y & 0 & 0 & 0 & M_{der} & 0 \end{bmatrix} \tag{4.6}$$

The corresponding part of the interpolator is

$$M_{int,E} = M_{int,B} = \begin{bmatrix} 1 & 0 & 0 & 0 & 0 & 0 \\ 0 & M_{int} & 0 & 0 & 0 & 0 \\ 0 & 0 & M_{int} & 0 & 0 & 0 \\ 0 & 0 & 0 & 1 & 0 & 0 \\ 0 & 0 & 0 & 0 & M_{int} & 0 \\ 0 & 0 & 0 & 0 & 0 & M_{int} \end{bmatrix} \tag{4.7}$$

The interpolator then contains an interpolator for the electric field, one for the magnetic field, and one for each of the n_s particle species.

$$S_A = \mathrm{diag}(M_{int,E}, M_{int,B}, \underbrace{1, \ldots, 1}_{n_s}) \tag{4.8}$$

The corresponding S_D matrix is

$$S_D = \begin{bmatrix} 0 & c\vec{\nabla}\times & M_{int,E}\omega_1 & \ldots & M_{int,E}\omega_{n_s} \\ c\vec{\nabla}\times & 0 & 0 & \ldots & 0 \\ \omega_1 & 0 & \vec{\Omega}_1\times & 0 & \ldots 0 \\ \vdots & \vdots & \vdots & \vdots & \ddots \\ \omega_{n_s} & 0 & 0 & \ldots & \vec{\Omega}_{n_s}\times \end{bmatrix} \tag{4.9}$$

The matrices ω_i are diagonal, such that $(\omega_i)_{j,j}$ is the plasma frequency of particle specie i at discretisation point j. The structure of the $\vec{\Omega}_i\times$ is also straightforward

$$\vec{\Omega}_i\times = \begin{bmatrix} 0 & [\vec{\Omega}_{i,z}] & -[\vec{\Omega}_{i,y}] & 0 & 0 & 0 \\ -[\vec{\Omega}_{i,z}] & 0 & [\vec{\Omega}_{i,x}] & 0 & 0 & 0 \\ [\vec{\Omega}_{i,y}] & -[\vec{\Omega}_{i,x}] & 0 & 0 & 0 & 0 \\ 0 & 0 & 0 & 0 & [\vec{\Omega}_{i,z}] & -[\vec{\Omega}_{i,y}] \\ 0 & 0 & 0 & -[\vec{\Omega}_{i,z}] & 0 & [\vec{\Omega}_{i,x}] \\ 0 & 0 & 0 & [\vec{\Omega}_{i,y}] & -[\vec{\Omega}_{i,x}] & \end{bmatrix} \tag{4.10}$$

where $[\vec{\Omega}_{i,x}], [\vec{\Omega}_{i,y}], [\vec{\Omega}_{i,z}]$ are diagonal matrices whose element (j,j) is the $x-$, $y-$ or $z-$ component of the vectorial cyclotron frequency associated with particle specie i at discretisation point j.

The thus-discretized equations allow for the time-domain numerical solution of any 1D problem in cold plasma theory, including plasma wave beaches, Budden tunneling and mode conversion.

4.1.4 Exploiting the constitutive equation's exact discrete locality

Let us partition $(S_A - S_D\Delta_t/2)$ as follows

$$\begin{pmatrix} EB & JE \\ EJ & JJ \end{pmatrix} \tag{4.11}$$

Submatrix EB contains all electric/magnetic interactions, JE and EJ all electric/current interactions, and JJ the current-current interactions due to the background magnetic field. Thanks to mass lumping, the JJ part is purely local and hence block-diagonal implying that $(JJ)^{-1}$ can easily be calculated explicitly. The inverse of $(S_A - S_D \Delta_t/2)$ can then be expressed using the Schur complement $S = EB - (JE)(JJ)^{-1}(EJ)$:

$$\begin{pmatrix} EB & JE \\ EJ & JJ \end{pmatrix}^{-1} = \begin{pmatrix} S^{-1} & -S^{-1}(JE)(JJ)^{-1} \\ -(JJ)^{-1}(EJ)S^{-1} & (JJ)^{-1} + (JJ)^{-1}(EJ)S^{-1}(JE)(JJ)^{-1} \end{pmatrix} \tag{4.12}$$

Note that the dimension of S (say $m \times m$) is already smaller than that of S_A or S_D. The size of S is independent of the number of particle species N_s, while the number of elements of S_A and S_D increases proportional to N_s^2. In practice, a sparse LU decomposition [2] of the Schur complement is found to contain only $O(m)$ nonzero elements, i.e. $Sx = y$ can be solved for x in $O(m)$ if the LU decomposition is known. A direct solver based on formula (4.12) and an LU decomposition of the Schur complement runs orders of magnitude faster than a naive stabilized biconjugate gradient method to solve $(S_A - S_D \Delta_t/2)x = y$. This is especially true for $c\Delta_t \gg \Delta$. For increasing $c\Delta_t$ the condition number of $(S_A - S_D \Delta_t/2)$ increases and hence the amount of iterations needed for an iterative solution. However, this increase of $c\Delta_t$ barely influences the time needed for a direct solution using (4.12) and $Sx = y$ at all. We will come back to this point in Section 4.2.3, providing some data to illustrate the above considerations.

4.2 Cold plasma numerical examples

4.2.1 A plasma wave beach

The simplest phenomenon which exists in plasmas but not in vacuum or other simpler dielectrics, is that cold 1-specie unmagnetized plasmas will only support waves whose frequency is higher than the plasma frequency ω_p. Simple examples can be constructed in which a wave propagates through a plasma of increasing density. At a certain point, it reaches the cutoff condition $\omega_p = \omega$ and stops propagating.

In figure 4.1, we show the eigenvalues of the time-stepping operator for a uniform unmagnetized 1-specie cold plasma. As expected, there are no eigenvectors with frequencies below the plasma frequency.

In figure 4.2, typical plasma wave beach behaviour is shown. The wave stops propagating when the plasma becomes sufficiently dense.

4.2.2 Numerical reproduction of a dispersion curve

Using periodic boundary conditions, the eigenvectors of the time-stepping operator are complex exponentials (real k) for every field component. The corresponding eigenvalues correspond to frequencies $\omega = \arg(\lambda)/\Delta_t$.
Thus, every (eigenvector,eigenvalue)-pair corresponds to a (k, ω)-pair. In this way, we can obtain the full numerical dispersion relation from numerically-obtained

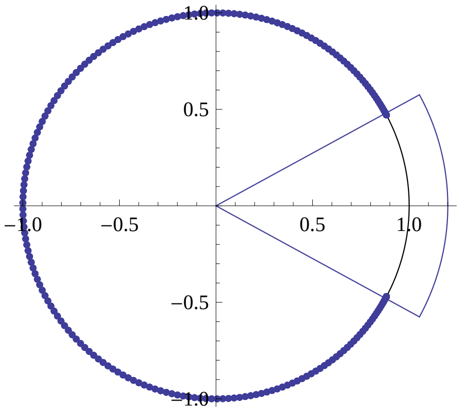

Figure 4.1: Eigenvalues for a uniform unmagnetized cold plasma. Note how no solutions exist in the region below the plasma frequency, when $|\arg(\lambda)|/\Delta_t < \omega_p$.

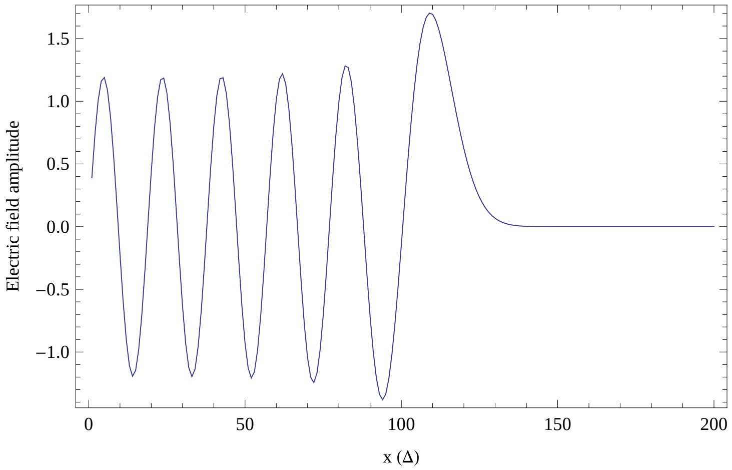

Figure 4.2: Electric field behaviour in a plasma wave beach. The density increases towards the right.

eigenvectors and eigenvalues of the time-stepping operator. Using a modification of this technique, numerical dispersion relations involving complex k-values can also be obtained, see section 4.4.

In Fig. 4.3, the numerical dispersion relation for a uniform magnetized 4-specie plasma like that to the high-field side (far left) of Fig. 4.5 (parameters specified in section 4.2.3) is shown as a function of the circular frequency ω. For comparison, the real roots of the exact continuous dispersion relation are shown too, as well as the expected roots of the discrete dispersion relation (3.33) which should - and do - match the numerical results exactly. The precise mapping to achieve this is

$$\omega_{\text{effective}} = \arctan\left(\frac{\omega_{\text{exact}}\Delta_t}{2}\right)\frac{2}{\Delta_t} \tag{4.13}$$

$$k_{\text{effective}} = \arctan\left(\frac{k_{\text{exact}}\Delta}{2}\right)\frac{2}{\Delta} \tag{4.14}$$

and is shown in figure 4.4.

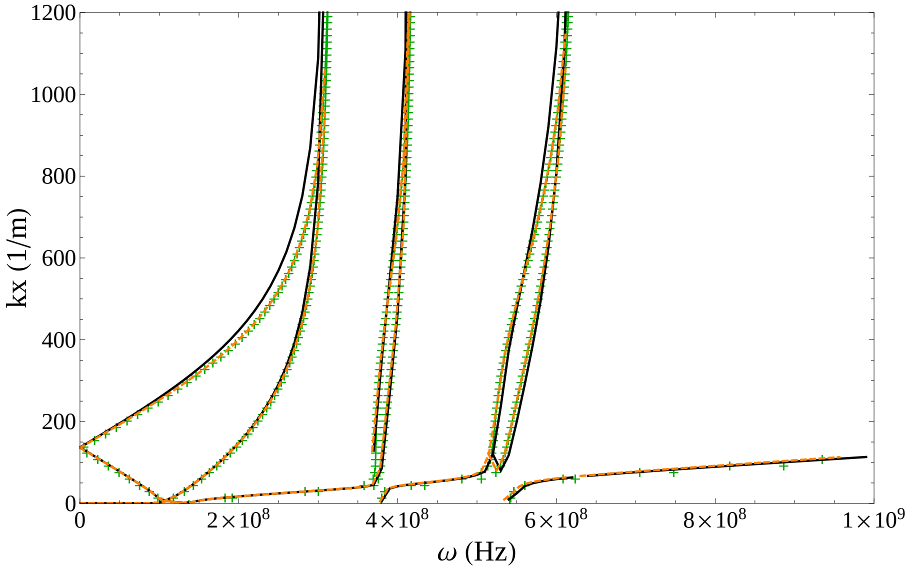

Figure 4.3: Green : Numerical value of $|k_x|$ versus ω obtained by calculating the eigenvectors of the system matrix and Fourier transforming them in space. The obtained k_x is always real. Black: Analytically determined $|k_x|$ for propagating (real k_x) solutions of the exact dispersion relation. Orange: Analytically predicted discrete dispersion relation by replacing ω and k_x by the relevant tangent functions in the continuous dispersion relation.

4.2.3 Mode conversion

Mode conversion from the fast wave to the ion-cyclotron wave is a phenomenon of interest for Ion-Cyclotron Resonance Heating (ICRH) [6, 4]. This 1D example is similar to the one used by Smithe [7].

The simulation has PEC boundary conditions and $k_y = 14.5m^{-1}$. The plasma itself has the following parameters:

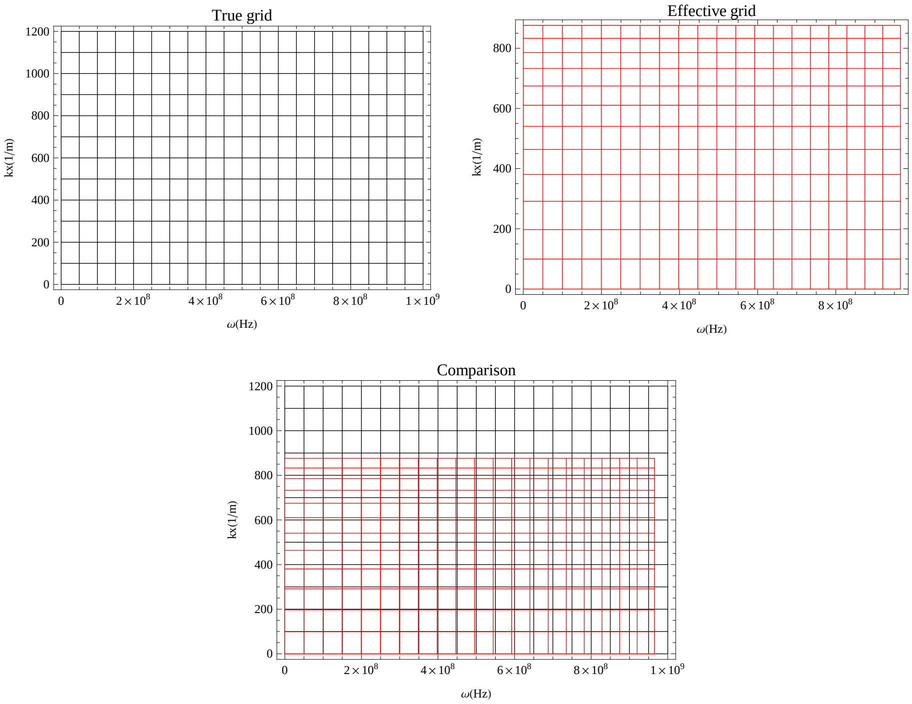

Figure 4.4: The mapping from the "exact" to the "effective" grid in this figure is precisely the mapping from the exact (black) curve in figure 4.3 to the analytically predicted discrete dispersion relation (orange in figure 4.3).

- $[B_{0x}, B_{0y}, B_{0z}](x) = [0.15B(x)\cos(\pi/4), B(x), 0.15B(x)\sin(\pi/4)]$ where $B(x)$ decreases like $1/x$ from $6.5T$ at the far left (High Field Side or HFS) of the simulation domain to $5.5T$ at the far right (Low Field Side or LFS). Further note that B_x and B_z cause coupling between the two modes
- Species: electrons ($n_e = 2 \cdot 10^{20} m^{-3}$), protons ($n_p/n_e = 0.33$), deuterons ($n_d/n_e = 0.44$), ^{3}He-nuclei ($n_{He3}/n_e = 0.115$).
- Frequency $80.5 \cdot 10^6$ Hz
- $\Delta_x = 8 \cdot 10^{-4} m$

To get a better understanding of the physics of the problem, Fig. 4.5 shows a *space-dependent* dispersion relation. It was obtained by substituting fields with a $\exp(ik_x x)\exp(ik_y y)\exp(i\omega t)$ dependence into the continuous equations (2.26)-(2.28) in a *uniform* plasma, and then finding the values of k_x for which a non-trivial solution exists (this involves solving a general quartic equation) with $k_y = 14.5m^{-1}$. At every position x, the plasma parameters are calculated and then

$k_x(x)$ is obtained by assuming a uniform plasma with these parameters. As such, Fig. 4.5 is an approximation; it tells us which wavelength(s) to expect but does not give us the exact information (as would be the case for a uniform plasma). As the waves propagate to the right (LFS), shorter wavelengths (higher k) are excited.
Due to the presence of a background magnetic field that is not purely toroidal ($B_x, B_z \neq 0$), the constitutive equation (2.28) enforces a relationship between all current components and as a consequence all cartesian components of the electric field, the magnetic field and currents are nonzero.

Despite there being only 200 discretization points in the $x-$direction, the time-step matrices are of size 7200×7200: there are 6 vector fields to consider (electric, magnetic and 4 currents of the 4-species), every field is described by 2 modes and has 3 scalar components. Thus, there are $2 \times 3 \times 200$ unknowns per field, or $36 \times 200 = 7200$ unknowns in total (36 degrees of freedom per discretization point).

In Fig. 4.6, by way of example, one of the eigenmodes of the studied configuration is shown at a frequency of $80.5 \cdot 10^6$ Hz. This result was obtained by calculating an eigenvector of the time-stepping operator $(S_A - S_D \Delta_t/2)^{-1}(S_A + S_D \Delta_t/2)$ (at $c\Delta_t = \Delta_x$). Fig. 4.7 was obtained using time-stepping and a sinusoidal source of $80.5 \cdot 10^6$ Hz multiplied with a Heaviside step at $t = 0$. In this figure, $c\Delta_t = 100\Delta_x$ which is far above the vacuum Courant condition (This choice of Δ_t corresponds to $46\Delta_t \approx P = 2\pi/\omega$. Obeying the vacuum Courant condition at the same Δ_r would require $4600\Delta_t \approx P$, i.e. vastly more time steps per period). Nonetheless the system remains stable as predicted. In both of the above figures we can clearly see the mode conversion from the fast to the ion-cyclotron wave, i.e. the appearance of short wavelength phenomena at the right.
For the above configuration we also investigated the efficiency of the algorithms for solving the sparse set of equations at every time step. Starting from a very crude discretization of 25 points in the $x-$direction, we gradually refined the discretization to 2500 points. We kept Δ_x constant and scaled the magnetic field variation such that $B(x)$ is always 6.5T at the left and 5.5T at the right, i.e. the magnetic field decrease is far steeper for a small amount of discretization points than for a large amount of discretization points. By doing this we ensure that λ/Δ_x remains in some sense constant. From Fig. 4.8, it is clear that the number of nonzero elements in the sparse LU-decomposition of the Schur complement S (see (4.12)) is linear in the amount of discretization points, and thus provides an efficient solution method. In Fig. 4.9 the time needed for a direct solution (for 71 discretization points in the $x-$direction) is compared to the time needed for an iterative solution (using the iterative solvers and LU decomposition algorithms available in Matlab and ran on an Intel Core 2Quad CPU Q9650 3GHz processor) and this as a function of $c\Delta_t/\Delta_x$. It is clear that the time for the iterative solution increases as the time step increases beyond the vacuum Courant limit while the time needed for the direct solution stays constant.

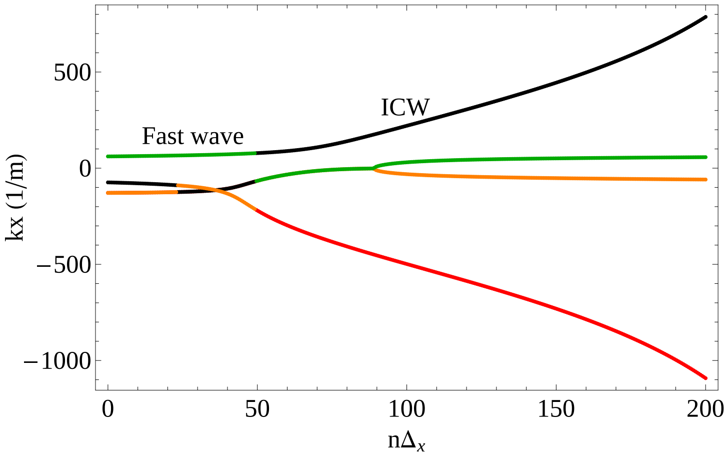

Figure 4.5: Space-dependent dispersion relation: $\Re(k_x)$ as a function of $n\Delta_x$ with mode conversion. Colours indicate the four solutions.

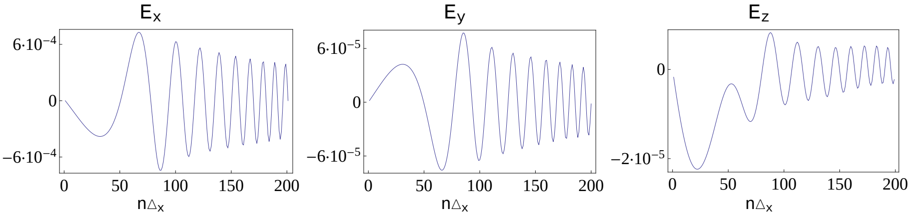

Figure 4.6: Real part of components of the electric field for an eigenmode of a plasma-filled cavity with mode conversion (at a frequency of $80.5 \cdot 10^6$ Hz).

4.2.4 Budden tunneling

The wave equation

$$\frac{\partial^2}{\partial x^2}E + k(x)^2 E = \frac{\partial^2}{\partial x^2}E + \left(\frac{\beta}{x} + \frac{\beta^2}{\eta^2}\right) E = 0 \tag{4.15}$$

can be solved exactly in terms of hypergeometric functions [8]. This is known as Budden tunneling. $k_\infty^2 = \frac{\beta^2}{\eta^2}$ is the asymptotic (large $|x|$) wavenumber. The distance between the zero $k(x) = 0$ and the singularity is $\Delta = \frac{\eta^2}{\beta}$, from which $\eta = |k_\infty \Delta|$ relates to the amount of asymptotic wavelengths between the zero and the singularity.

Analytical expressions for reflection- and transmission-coefficients are known. In particular, the absolute value of the transmission coefficient for a left-moving wave

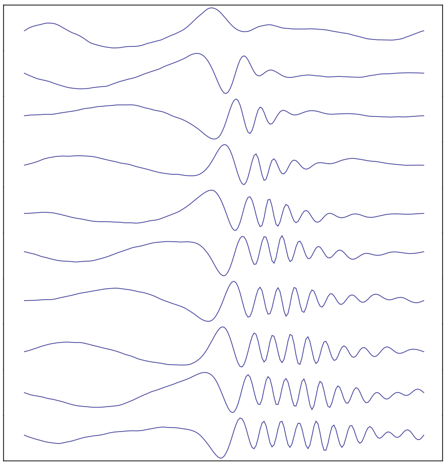

Figure 4.7: E_x after 1000 (top),2000,...,10000 (bottom) time steps, at $c\Delta_t = 100\Delta_x$. No attempt was made to filter out the desired mode at one particular frequency. This plot contains contributions of all resolvable frequencies in the Heaviside$(t)\sin(\omega t)$ source.

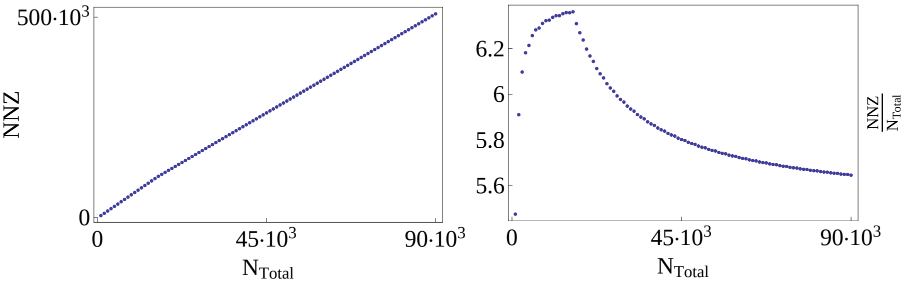

Figure 4.8: Absolute number of nonzero (NNZ) elements in the sparse LU decomposition of the Schur complement of $(SA - SD\Delta_t/2)$ versus total amount of unknowns N_{total} (left) and relative number (right).

is

$$|T| = \exp\left(-\frac{1}{2}\pi\eta\right) \tag{4.16}$$

In plasma physics, Budden tunneling is usually an approximation [5]. It is possible to construct the space-dependence of the density and the background magnetic field in such a way that the cold plasma wave equation becomes the Budden equation (4.15) exactly (at a specific frequency ω). In figure 4.10, we have modeled such a plasma ($\beta = 1, \eta = 1$). The resulting numerical transmission coefficient is indeed close to the predicted one.

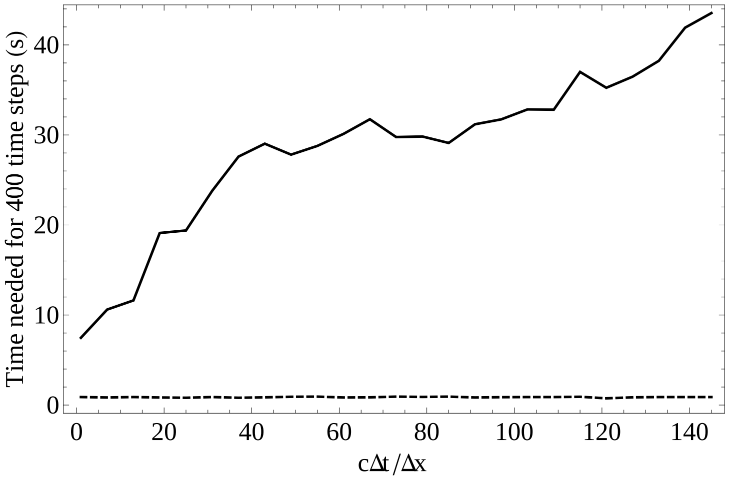

Figure 4.9: Time needed for a direct solution (dashed) vs. a naive stabilized biconjugate gradient (solid). (configuration of section 4.2.3, 71 discretization points). Initialisation time needed to calculate the LU decomposition of the Schur complement (direct case) or an incomplete LU preconditionner (iterative case) is not included on this graph.

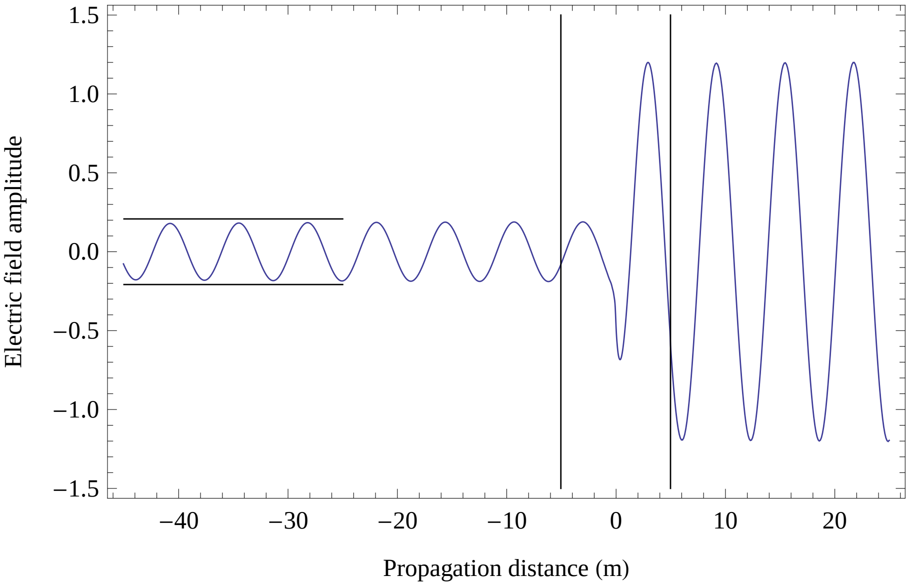

Figure 4.10: Budden tunneling. The wave is traveling from right to left. Vertical black lines indicate the refined implicit region near the zero and singularity of the non-uniform wave equation. Horizontal black lines indicate the analytically expected amplitude of the transmitted wave based on Budden theory.

4.3 Time-stepping operator for warm plasma

In [9], we started from the anti-Hermitized set of equations (2.61), mostly for the reasons pointed out in section 4.1.2. However, it would be better to start directly from (2.57)-(2.58), if this is possible. To do this, we must carefully verify the existence of a discrete analogon to the rescaling (2.59), noting that the position-dependent quantities may not commute with the spatial derivative operators. Indeed, demanding that such a rescaling exists will give some, though possibly not all, information about what the correct order of the non-commuting operators should be in the first place [3].

Note that position-dependent quantities, discretized as real diagonal (and thus symmetric) matrices, correspond to hermitian matrices in the Fourier basis:

$$\mathfrak{F}\omega_p\mathfrak{F}^{-1} = \mathfrak{F}\omega_p\mathfrak{F}^{\dagger} \tag{4.17}$$

$$\left(\mathfrak{F}\omega_p\mathfrak{F}^{\dagger}\right)^{\dagger} = \mathfrak{F}\omega_p\mathfrak{F}^{\dagger} \tag{4.18}$$

Consider the matrix function $\sqrt{1+\lambda}$, which we expect to encounter based on (2.59). If λ is hermitian and positive definite, then λ can be diagonalized by an orthogonal basis $\mathfrak{U}$, and has real positive eigenvalues Λ

$$\lambda = \mathfrak{U}\Lambda\mathfrak{U}^{\dagger} \tag{4.19}$$

then

$$\sqrt{1+\lambda} = \mathfrak{U}\sqrt{1+\Lambda}\mathfrak{U}^{\dagger} \tag{4.20}$$

is also hermitian and positive definite. The same holds for $\sqrt{1+3\lambda}$, which also occurs in (2.59).

λ is obviousely positive definite. We can make it hermitian in the Fourier basis by choosing a certain ordering (there are other possibilities)

$$\mathfrak{F}\lambda\mathfrak{F}^{-1} = \mathfrak{F}\frac{v_{th}}{\sqrt{2}\Omega}k^2\frac{v_{th}}{\sqrt{2}\Omega}\mathfrak{F}^{-1} \tag{4.21}$$

$$= \mathfrak{F}\frac{v_{th}}{\sqrt{2}\Omega}\mathfrak{F}^{-1}\mathfrak{F}k^2\mathfrak{F}^{-1}\mathfrak{F}\frac{v_{th}}{\sqrt{2}\Omega}\mathfrak{F}^{-1} \tag{4.22}$$

$\mathfrak{F}\frac{v_{th}}{\sqrt{2}\Omega}\mathfrak{F}^{-1}$ is hermitian. If $-k^2$ is the standard finite-difference second-order spatial derivative operator (4.23), $\mathfrak{F}k^2\mathfrak{F}^{-1}$ is real and diagonal, from which the hermiticity of (4.22) follows.

$$\frac{\partial^2}{\partial x^2}f(x) \approx \frac{f(x-\Delta) - 2f(x) + f(x+\Delta)}{\Delta^2} \tag{4.23}$$

The second-order differentiator k^2 was, in [9], discretized in a fully implicit way, complete with second-order spatial interpolators. This is necessary for the clean dispersion relation formula (3.33) to hold, but has no use other than that. Unlike the first-order spatial derivative, the second-order finite difference spatial derivative (4.23) is naturally collocated with the grid from which it is obtained. It is diagonalized by the Fourier basis just like the implicit operators, and its eigenvalues are real and negative (corresponding to $(ik)^2 = -k^2$).

If we consider only magnetic field and temperature variation, but not density variation, this suffices. Let us consider elements (7,2) and (2,7) in $A_L^{-1}A_R$ (2.57)-(2.58)

$$\begin{array}{cc} (1+3\lambda)^{-1}\omega_p^2\epsilon_0 & (7,2) \\ -1/\epsilon_0 & (2,7) \end{array} \tag{4.24}$$

The rescaling is

$$\begin{array}{cc} \frac{\sqrt{1+3\lambda}}{\omega_p\sqrt{\epsilon_0}}\left((1+3\lambda)^{-1}\omega_p^2\epsilon_0\right)\frac{1}{\sqrt{\epsilon_0}} & (7,2) \\ \sqrt{\epsilon_0}\left(-1/\epsilon_0\right)\omega_p\sqrt{\epsilon_0}\sqrt{1+3\lambda}^{-1} & (2,7) \end{array} \tag{4.25}$$

which simplifies to

$$\begin{array}{cc} \sqrt{1+3\lambda}^{-1}\omega_p & (7,2) \\ -\sqrt{1+3\lambda}^{-1}\omega_p & (2,7) \end{array} \tag{4.26}$$

which becomes anti-hermitian in the Fourier basis as we discussed above.

Now consider elements (7,6) and (6,7) in $A_L^{-1}A_R$ (2.57)-(2.58). Note the position of Ω.

$$\begin{array}{cc} (1+3\lambda)^{-1}(1+2\lambda)\Omega & (7,6) \\ -(1+\lambda)^{-1}\Omega(1+2\lambda) & (6,7) \end{array} \tag{4.27}$$

The rescaling is

$$\begin{array}{cc} \frac{\sqrt{1+3\lambda}}{\omega_p\sqrt{\epsilon_0}}(1+3\lambda)^{-1}(1+2\lambda)\Omega\sqrt{1+\lambda}^{-1}\omega_p\sqrt{\epsilon_0} & (7,6) \\ -\frac{\sqrt{1+\lambda}}{\omega_p\sqrt{\epsilon_0}}(1+\lambda)^{-1}\Omega(1+2\lambda)\sqrt{1+3\lambda}^{-1}\omega_p\sqrt{\epsilon_0} & (6,7) \end{array} \tag{4.28}$$

which simplifies to

$$\begin{array}{cc} \sqrt{1+3\lambda}^{-1}(1+2\lambda)\Omega\sqrt{1+\lambda}^{-1} & (7,6) \\ -\sqrt{1+\lambda}^{-1}\Omega(1+2\lambda)\sqrt{1+3\lambda}^{-1} & (6,7) \end{array} \tag{4.29}$$

which becomes anti-hermitian in the Fourier basis as we discussed above. These two examples suffice, the other nonzero elements in $A_L^{-1}A_R$ follow the same pattern.

The full discrete equations for the case of section 2.4.2 become

$$S_A = \begin{bmatrix} I_n & 0 & 0 & 0 & 0 & 0 & 0 & 0 \\ 0 & M_{int} & 0 & 0 & 0 & 0 & 0 & 0 \\ 0 & 0 & M_{int} & 0 & 0 & 0 & 0 & 0 \\ 0 & 0 & 0 & I_n & 0 & 0 & 0 & 0 \\ 0 & 0 & 0 & 0 & I_n & 0 & 0 & 0 \\ 0 & 0 & 0 & 0 & 0 & I_n + \lambda_D & 0 & 0 \\ 0 & 0 & 0 & 0 & 0 & 0 & I_n + 3\lambda_D & 0 \\ 0 & 0 & 0 & 0 & 0 & 0 & 0 & I_n \end{bmatrix} \tag{4.30}$$

$$S_D = \begin{bmatrix} 0 & 0 & 0 & -I_n/\epsilon_0 & 0 & -I_n/\epsilon_0 & 0 & 0 \\ 0 & 0 & \frac{M_{der}}{\epsilon_0\mu_0} & 0 & \frac{-M_{int}}{\epsilon_0} & 0 & \frac{-M_{int}}{\epsilon_0} & \frac{-M_{int}}{\epsilon_0} \\ 0 & M_{der} & 0 & 0 & 0 & 0 & 0 & 0 \\ \omega_p\lambda_D\omega_p\epsilon_0 & 0 & 0 & 0 & -2\Omega & 0 & 0 & 0 \\ 0 & \omega_p\lambda_D\omega_p\epsilon_0 & 0 & 2\Omega & 0 & 0 & 0 & 0 \\ \omega_p^2\epsilon_0 & 0 & 0 & 0 & 0 & 0 & -\Omega(1+2\lambda_D) & 0 \\ 0 & \omega_p^2\epsilon_0 & 0 & 0 & 0 & (1+2\lambda_D)\Omega & 0 & 0 \\ 0 & 2\omega_p\lambda_D\omega_p\epsilon_0 & 0 & 0 & 0 & 0 & 0 & 0 \end{bmatrix} \tag{4.31}$$

$$\lambda_D = \frac{v_{th}}{\sqrt{2}\Omega} \left(-M_{\mathrm{der}^2,\ \mathrm{central\ difference}}\right) \frac{v_{th}}{\sqrt{2}\Omega} \tag{4.32}$$

$$\left(\frac{1}{\Delta_t} S_A - \frac{1}{2} S_D\right) V_{t+1} = \left(\frac{1}{\Delta_t} S_A + \frac{1}{2} S_D\right) V_t \tag{4.33}$$

where $M_{\mathrm{der}^2,\ \mathrm{central\ difference}}$ is the matrix corresponding to the operator (4.23).

4.4 Warm plasma numerical examples

In figure 4.11, we numerically calculated the warm plasma dispersion relation for the $k_{\|} = 0, \vec{E} \perp \vec{B_0}$ case, and compared it with the exact result. We used numerically determined eigenvectors and eigenvalues of the time-stepping operator to obtain the dispersion relation, in the same fashion as figure 4.3. As we pointed out before, periodic boundary conditions give rise to eigenvectors which are complex exponentials with real k, i.e. $n^2 > 0$. The $n^2 < 0$ solutions which also appear in figure 4.11 were calculated using different boundary conditions : (the fields at the left of the simulation region)=(the fields at the right of the simulation region)$\times \exp(-k_i L)$, where k_i is the desired imaginary part of k and L is the length of the simulation region. Using this boundary condition, the eigenvectors of the time-stepping operator become complex exponentials with given k_i, and the evanescent $n^2 < 0$ solutions can be found among them.

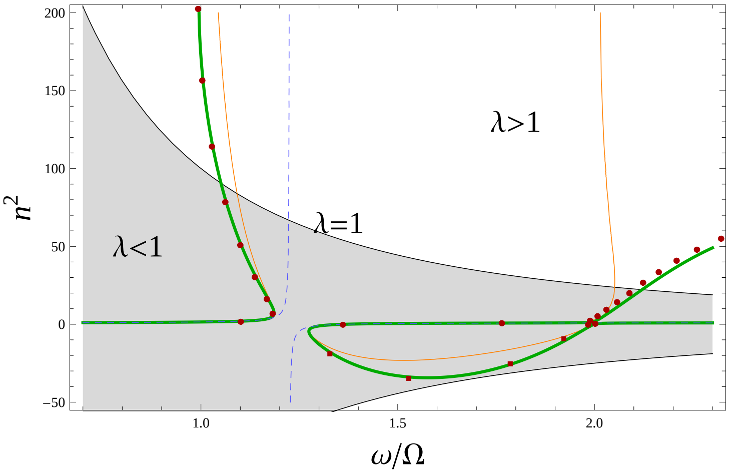

Figure 4.11: Exact hot plasma dispersion (orange line), rational approximation (green line), numerical result (red dots), and cold plasma dispersion (blue dashed).

4.5 Thin conducting layers

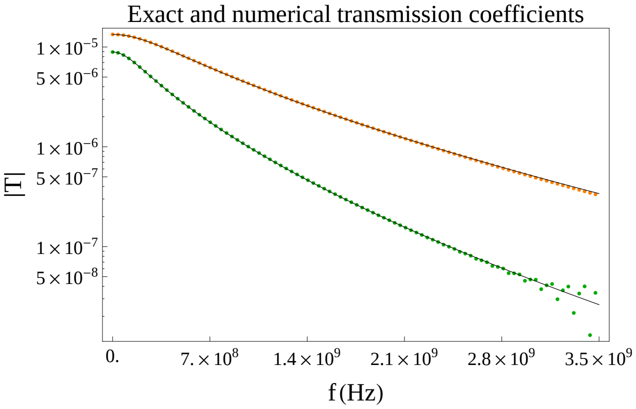

Figure 4.12: Exact and numerical transmission coefficient for waves propagating through a thin layer of copper (green) or a thin layer of material with parabolicaly varying conductivity (orange). See also figure 4.13

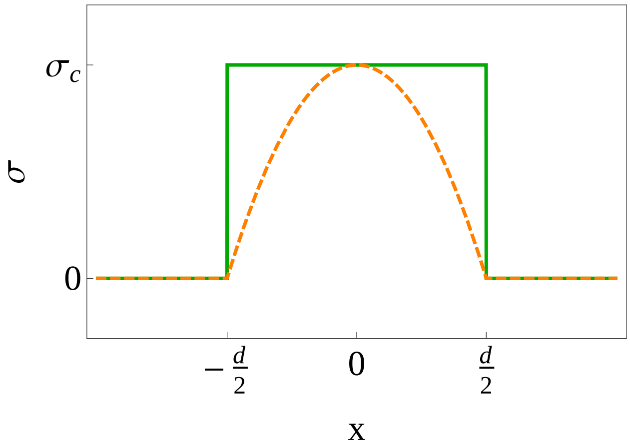

Figure 4.13: Conductivity profiles corresponding to figure 4.12.

The fully implicit method can be hybridized with the classical FDTD method (see section 5.3), enabling local refinement in FDTD without having to decrease the time step. This can be used to calculate electromagnetic phenomena involving thin evanescent layers, the most common of which are electromagnetic waves propagating through thin sheets of conducting material. Such evanescent behaviour in conductors stems from interaction between the electromagnetic wave and the high-ω_p electron plasma inside the conductor crystal.

We typically calculate the transmission coefficient for a wave traveling through a very thin layer of copper (figure 4.12). The thickness of the conductor is $d = 10\mu m = (13 \cdot 10^{-5})\Delta_{FDTD}$, far smaller than the FDTD discretisation length. There are 50 implicit points inside this thin conducting layer. The entire algorithm runs at the FDTD courant limit. The size of the set of equations to be solved only depends on the amount of discretisation point inside the conductor. In this example, $\Delta_{FDTD} = 75mm$. For well-resolved wavelengths, the analytical and numerical solution are nearly equal. As the frequency increases, the waves become ill-resolved in either the FDTD part or the implicit part, and the results become inaccurate.

We also calculated the transmission coefficient through a thin conducting layer with parabolic σ variation, ($\sigma = \sigma_{copper}(1 - (2x/d)^2)$ where d is still the layer thickness). The exact solution can still be calculated in terms of parabolic cylinder functions [1], the solutions to the so-called Weber equation (4.34) (figure 4.14).

$$\frac{\partial^2 f}{\partial x^2} - \left(\nu + \frac{1}{2} - \frac{1}{4}x^2\right) f = 0 \tag{4.34}$$

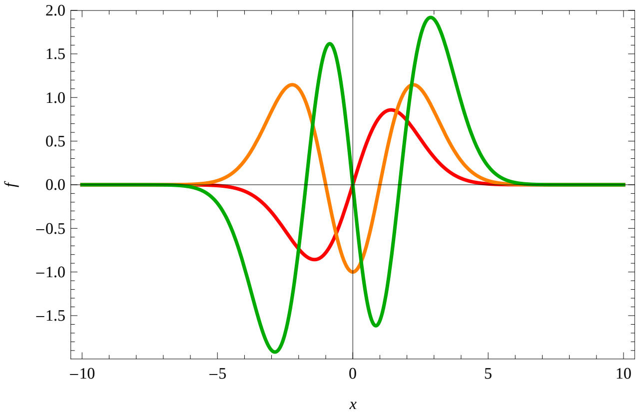

Figure 4.14: Parabolic cylinder function for $\nu = 1, 2, 3$.

4.6 Conclusion

This chapter contains the majority of numerical examples in this doctoral thesis. We showed that our method is capable of modeling (in cold plasma) plasma wave beaches, mode conversion and Budden tunneling. We also numerically produced a warm plasma dispersion relation which includes a Bernstein wave. More down-to-earth examples included wave propagation through thin layers of conducting material, where our method is capable of calculating transmission coefficients with great accuracy, and without the problems usually associated with thin layers in FDTD.

Bibliography

[1] M. Abramowitz and I. Stegun. *Handbook of Mathematical Functions with Formulas, Graphs, and Mathematical Tables*. Dover Publications, 1964.

[2] M. Bolhoffer and Olaf Schenk. Combinatorial aspects in sparse elimination methods. *GAMM Mitteilungen*, 29:342–367, 2006.

[3] M. Brambilla. Finite Larmor radius wave equations in tokamak plasmas in the ion cyclotron frequency range. *Plasma Physics and Controlled Fusion*, 31(5):123–151, 1989.

[4] Y. Kazakov, I. Pavlenko, D. Van Eester, B. Weyssow, and I. Girka. Enhanced ICRF (ion cyclotron range of frequencies) mode conversion efficiency in plasmas with two mode conversion layers. *Plasma Physics and Controlled Fusion*, 52(11):115006, 2010.

[5] Y. Kazakov, I. Pavlenko, and I. Girka. Propagation of the fast magnetosonic wave through the generalized Budden barrier. *ВОПРОСЫ АТОМНОЙ НАУКИ И ТЕХНИКИ*, pages 90–93, 2010.

[6] M.J. Mantsinen, M.-L. Mayoral, and D. Van Eester. Localized bulk electron heating with ICRF mode conversion in the JET tokamak. *Nuclear Fusion*, 44(1):33–46, 2004.

[7] D. N. Smithe. Finite-difference time-domain simulation of fusion plasmas at radiofrequency time scales. *Physics of Plasmas*, 14(14):2537–2549, Apr. 2007.

[8] T. Stix. *Waves in Plasmas*. American Institute of Physics, 1992.

[9] W. Tierens and D. De Zutter. Finite-temperature corrections to the time-domain equations of motion for perpendicular propagation in nonuniform magnetized plasmas. *Physics of Plasmas*, 19:1–9, 2012.

[10] W. Tierens and D. De Zutter. An unconditionally stable time-domain discretization on cartesian meshes for the simulation of nonuniform magnetized cold plasma. *Journal of Computational Physics*, pages 5144–5156, 2012.

5

Advantages of finite-element interpretations

★ ★ ★

The finite-element interpretation of the FDTD method has led to a variety of improvements including local spatial refinement, local higer-order approximations, and extensions thereof to different geometries. In this chapter we provide a short introduction to Finite Element methods, and show how they can be used for local refinement in toroidal geometries and to hybridize the fully implicit method of chapter 3 with the classical FDTD method.

5.1 A short introduction to Finite Element methods

Consider a differential equation, for example

$$\frac{\partial}{\partial x} f(x) = g(x) f(x) \tag{5.1}$$

Finite Element methods discretize linear partial differential equations by writing the unknown function $f(x)$ as a linear combination of basis-functions $b_i(x)$.

$$f(x) = \sum_{i=1}^{n} \alpha_i b_i(x) \tag{5.2}$$

If n basis-functions are used, n equations must be constructed which can be solved for the n unknown expansion coefficients α_i. This is done by “testing” the differential equation with n so-called test-functions $t_j(x)$, i.e. multiplying both sides of the differential equation with $t_j(x)$ and integrating over x

$$\sum_{i=1}^{n} \alpha_i \frac{\partial}{\partial x} b_i(x) = g(x) \sum_{i=1}^{n} \alpha_i b_i(x) \tag{5.3}$$

$$\int t_j(x) \left(\sum_{i=1}^{n} \alpha_i \frac{\partial}{\partial x} b_i(x) \right) dx = \int t_j(x) \left(g(x) \sum_{i=1}^{n} \alpha_i b_i(x) \right) dx \tag{5.4}$$

For every j, this gives a linear equation in the unknown coefficients α_i. This set of equations may be solved for the coefficients α_i, and then (5.2) is an approximation to the true solution of the differential equation.

If the test-functions and the basis-functions are the same, this is also known as a Galerkin method. If they are not, this is also known as a Petrov-Galerkin method [4].

5.2 Local refinement in toroidal geometries

In the next pages we include our paper [26], where we constructed an explicit and unconditionally stable subgridding technique in cylindrical coordinates. We have not been able to use this technique for local refinement in plasmas, due to the difficulty of combining the cold plasma constitutive equation (2.11) with the staggered basis-functions of FDTD [7]. However, it can still be used for other purposes, notably the numeric calculation of eigenfrequencies of an electromagnetic Body-Of-Revolution cavity with sharp internal features. In [26], we calculated the resonant frequencies of an Alvarez-type particle accelerator [5, 23] in this fashion.

5.2.1 BOR-FDTD Subgridding Based on Finite Element Principles

Originally published: W. Tierens and D. De Zutter. “BOR-FDTD subgridding based on finite element principles.” *Journal of Computational Physics* 230.12 (2011): 4519-4535.

In this paper a recently developed provably passive and stable 3D FDTD subgridding technique, based on finite elements principles, is extended to Body-Of-Revolution (BOR) FDTD. First, a suitable choice of basis functions is presented together with the mechanism to assemble them into an overall mesh consisting of coarse and fine mesh cells. Invoking appropriate mass-lumping concepts then leads to an explicit leapfrog time stepping algorithm for the amplitudes of the basis functions. Attention is devoted to provide the reader with insight into the updating equations, in particular at a subgridding boundary. Stability, grid reflection and dispersion are also discussed. Finally, some numerical examples for toroidal and cylindrical cavities demonstrate the stability and accuracy of the method.

5.2.2 Introduction

The Finite Difference Time Domain (FDTD) method [22] is one of the most powerful tools in electromagnetic modeling. It is massively parallelizable, matrix-free in contrast to finite-element (FE) techniques, does not require the knowledge of suitable Green’s functions, as is the case for integral equation methods and can handle complex geometries. In the past decades a lot of advances have been made with respect to absorbing boundary conditions, dispersion-relation preservation, subgridding, unstructured grids etc. For a review on these advances we refer to [24, 27] and the references therein and to the huge body of literature on these topics.

The work presented below was initially motivated by our interest in the complex phenomena that govern the behavior of Tokamak plasmas [20, 21] such as to be used in ITER [2, 19]. When using linearized plasma theory, an FDTD body of revolution (BOR-FDTD) approach can be used, to study each of the independent toroidal modes describing the plasma. In order to be able to predict all relevant wave phenomena, one must be able to correctly model transition regions where the solutions of the dispersion relation can change quite abruptly, involving the sudden and localized appearance of solutions with a wavelength many times shorter than the usual wavelength. This is the so-called *mode conversion* [21]. As a consequence of the different length scales of these wave phenomena, subgridding is indicated to alleviate the computational cost of maintaining an identical cell size over the complete problem space.

In this paper we report on our efforts to develop a suitable BOR-FDTD subgridding technique which can of course be used outside the context of plasma research. For an introduction to BOR-FDTD we refer to Chapter 12 of [22] and to e.g., [13, 9, 31, 12, 6]. Subgridding has been thoroughly investigated in the past

[25, 17, 29, 10, 7, 15, 14, 1, 30, 3, 11]. To develop BOR-FDTD subgridding, our starting point is the work of Chilton et. al. [7, 8] in which conservative, provably stable and explicit 3D FDTD subgridding methods are developed based on finite-element concepts.

This paper is organised as follows. Following the ideas put forward in [7, 8], Section 5.2.3 presents a new set of basis functions particularly tailored for BOR-FDTD, whereby electric field and magnetic induction basis functions explicitly satisfy Faraday's law. It is shown that, under certain assumptions, the classical BOR-FDTD update equations for a uniform grid [22] can be recovered. Section 5.2.4 introduces subgridding while Section 5.2.5 explains how to assemble a complete grid consisting of coarse and fine meshes. In Section 5.2.6 particular attention is devoted to the mass-lumping concepts that have to be introduced in order to obtain a provably stable and explicit method. Section 5.2.7 then presents the final leapfrog time stepping algorithm, taking care to provide insight on how the complete mathematical machinery leads to updating equations at the interfaces between coarse and fine meshes, update equations that are no longer intuitive. Section 5.2.8 presents some numerical results. First, stability, grid reflection and grid dispersion are discussed. Next, the field analysis in a toroidal perfectly conducting (PEC) cavity is used to illustrate the stability and accuracy of the subgridding. Finally, the resonance frequency of a reentrant cylindrical cavity as encountered in Alvarez-type particle accelerators, is calculated, showing that subgridding at the reentrant corner can substantially reduce simulation time and memory resources while retaining accuracy. The final section formulates a number of conclusions and future challenges.

5.2.3 BOR-FDTD discretisation of Maxwell's equations

Basis functions

As our starting point we take the classical BOR-FDTD representation of [22]. Fig. 5.1 shows a unit BOR-FDTD cell with material parameters ϵ and μ centered on the B_θ component, extending from $r = R_0$ to $r = R_0 + \Delta$ and from $z = Z_0$ to $z = Z_0 + \Delta$. For each angular mode M, the following 8 basis functions $\vec{E_n}$ for the electric field are introduced:

$$E_{ri} = \left(\begin{cases} \frac{z-Z_0}{\Delta} & i=0 \\ 1-\frac{z-Z_0}{\Delta} & i=1 \end{cases}\right)\cos(M\theta)\vec{1}_r \tag{5.5}$$

$$E_{\theta,ij} = \left(\begin{cases} \frac{z-Z_0}{\Delta} & i=0 \\ 1-\frac{z-Z_0}{\Delta} & i=1 \end{cases}\right)\cdot\left(\begin{cases} f_1(r) & j=0 \\ f_2(r) & j=1 \end{cases}\right)\sin(M\theta)\vec{1}_\theta \tag{5.6}$$

$$E_{zi} = \left(\begin{cases} \frac{r-R_0}{\Delta} & i=0 \\ 1-\frac{r-R_0}{\Delta} & i=1 \end{cases}\right)\cos(M\theta)\vec{1}_z \tag{5.7}$$

with $f_1(r) = \frac{R_0}{\Delta}\left(\frac{R_0+\Delta}{r}-1\right)$ and $f_2(r) = \frac{R_0+\Delta}{\Delta}\left(1-\frac{R_0}{r}\right)$. These basis functions are zero outside the considered cell. Their anchor points are also shown in Fig.

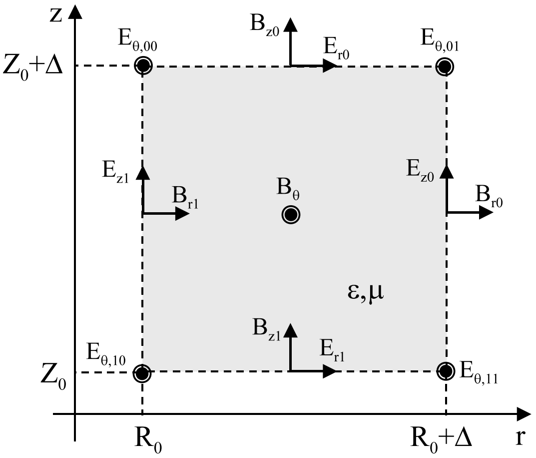

Figure 5.1: A Yee-like unit cell in BOR-FDTD showing the anchor points of the basis functions.

1. Each basis function is equal to one in its anchor point and zero in the other anchor points of corresponding field components, e.g. $E_{\theta,00}$ is equal to one in the upper left corner and zero in the three other corners. In BOR-FDTD calculations, the counterparts of (1)-(3) with $\cos(M\theta)$ replaced by $\sin(M\theta)$ and $\sin(M\theta)$ by $-\cos(M\theta)$ are also needed but will not be further discussed. At this point it should be remarked that the above defined basis functions are not curl conforming, but the grid assembling procedure described in Section 5.2.5 will result in the fact that the tangential component of the electric field becomes continuous everywhere. To be able to apply the procedures outlined in [8], the 5 basis functions $\vec{B_n}$ for the magnetic induction must satisfy the curl inclusion property: the curl of a linear combination of electric field basis functions must be a linear combination of magnetic induction basis functions. This is the case for (again see Fig. 1)

$$B_{ri} = \frac{(R_0+(1-i)\Delta)\sin(M\theta)}{r} \cdot \left(\begin{cases} \frac{r-R_0}{\Delta} & i=0 \\ 1-\frac{r-R_0}{\Delta} & i=1 \end{cases} \right) \vec{1}_r \tag{5.8}$$

$$B_\theta = \cos(M\theta)\vec{1}_\theta \tag{5.9}$$

$$B_{zi} = \frac{(R_0+\Delta/2)\sin(M\theta)}{r} \cdot \left(\begin{cases} \frac{z-Z_0}{\Delta} & i=0 \\ 1-\frac{z-Z_0}{\Delta} & i=1 \end{cases} \right) \vec{1}_z \tag{5.10}$$

Note that for $R_0 \gg \Delta$ all basis functions reduce to linear functions in $\alpha = (r - R_0)/\Delta$ and z, recovering the cartesian limit. Next, Faraday's law $\vec{\nabla} \times \vec{E} = -\frac{\partial \vec{B}}{\partial t}$ is discretized using the above defined basis functions, leading to its discrete counterpart

$$C\mathbf{e}(t) = -\frac{d\mathbf{b}(t)}{dt} \tag{5.11}$$

with $\mathbf{e}$ the column vector $[e_{r0}, e_{r1}, e_{\theta,00}, e_{\theta,01}, e_{\theta,10}, e_{\theta,11}, e_{z0}, e_{z1}]^T$ of electric field basis function amplitudes, $\mathbf{b} = [b_{r0}, b_{r1}, b_{\theta}, b_{z0}, b_{z1}]^T$ the corresponding magnetic induction basis function amplitudes and with C^T given by

$$\begin{bmatrix} 0 & 0 & \frac{1}{\Delta} & \frac{M}{R_0+\Delta/2} & 0 \\ 0 & 0 & \frac{-1}{\Delta} & 0 & \frac{M}{R_0+\Delta/2} \\ 0 & \frac{-1}{\Delta} & 0 & \frac{-R_0}{\Delta(R_0+\Delta/2)} & 0 \\ \frac{-1}{\Delta} & 0 & 0 & \frac{R_0+\Delta}{\Delta(R_0+\Delta/2)} & 0 \\ 0 & \frac{1}{\Delta} & 0 & 0 & \frac{-R_0}{\Delta(R_0+\Delta/2)} \\ \frac{1}{\Delta} & 0 & 0 & 0 & \frac{R_0+\Delta}{\Delta(R_0+\Delta/2)} \\ \frac{-M}{R_0+\Delta} & 0 & \frac{-1}{\Delta} & 0 & 0 \\ 0 & \frac{-M}{R_0} & \frac{1}{\Delta} & 0 & 0 \end{bmatrix} \tag{5.12}$$

Ampere's law $\vec{\nabla} \times \mu^{-1}\vec{B} = \epsilon\frac{\partial \vec{E}}{\partial t}$ is satisfied *weakly* by testing both sides with the electric field basis functions. This finally leads to

$$[\star_\epsilon]^{-1} C^T [\star_\mu^{-1}] \mathbf{b}(t) = \frac{d\mathbf{e}(t)}{dt} \tag{5.13}$$

where $[\star_\mu^{-1}]$ and $[\star_\epsilon]$ are the mass matrices obtained by integrating scalar products of basis functions over the whole problem volume.

$$[\star_\mu^{-1}]_{n,m} = \int \mu^{-1}\vec{B_n} \cdot \vec{B_m} dV \tag{5.14}$$

$$[\star_\epsilon]_{n,m} = \int \epsilon\vec{E_n} \cdot \vec{E_m} dV \tag{5.15}$$

The integration over θ is performed analytically, yielding a factor of π. The remaining integration over r and z could also be performed analytically. However, approximating these integrals using second-order accurate trapezoidal integration for both the integration over r and over z - so-called *mass lumping* [16] - makes these matrices diagonal with elements $[\star_\epsilon]_{n,n} = \frac{\epsilon\pi\Delta^2 R_0}{4}(2+\Delta', 2+\Delta', 1, 1+\Delta', 1, 1+\Delta', 2+2\Delta', 2)$, $[\star_\mu^{-1}]_{n,n} = \frac{\mu^{-1}\pi\Delta^2 R_0}{2}(1+\Delta', 1, 2+\Delta', 1+0.5\Delta', 1+0.5\Delta')$ and $\Delta' = \Delta/R_0$. The 8 electric field basis functions were ordered as follows: E_{r0}, E_{r1}, $E_{\theta,00}$, $E_{\theta,01}$, $E_{\theta,10}$, $E_{\theta,11}$, E_{z0}, E_{z1} and the 5 magnetic basis functions as B_{r0}, B_{r1}, B_θ, B_{z0}, B_{z1}. The above mentioned anchor point property of the basis functions is a necessary condition for the trapezoidal integration to lead to a diagonal matrix. The reader also notices that each entry of the mass matrices is proportional to the r-coordinate of the anchor point of the corresponding basis function.

However, when performing the calculations for the B_z components, the reader will find out that this is only the case provided terms of the order of $O(\Delta^4)$ are neglected, totally in line with the fact that the trapezoidal integration is only second order accurate in Δ. Although this proportionality with the radius of the anchor point is not strictly required, it turns out that in this way the mass-lumped finite element approach that we are using here, exactly recovers the classical BOR-FDTD update equations.

5.2.4 Subgridding basis functions

Starting from the above discretisation of Maxwell's equations for basis functions defined on a Δ by Δ grid, our aim is to obtain a conservative and stable subgridding procedure. Suppose that subgrids of size $\Delta/N \times \Delta/N$, with N an integer, are introduced. In order to be able to apply the theory put forward in [8], asserting that the resulting scheme is indeed conservative and stable, the basis functions on the $\Delta/N \times \Delta/N$ grid much be such that a linear combination of them yields the basis functions of the $\Delta \times \Delta$ grid. With this in mind, let us take a look at the four $E_{\theta,ij}$ functions defined in (2). In eq. 5.16 they are be cast in a matrix form. The r.h.s. coefficient matrix is non-singular and hence invertible. Consequently, 1 (the constant), z, z/r and $1/r$ (and all linear combinations thereof) can be written as linear combinations of the four E_θ basis functions.

$$\begin{bmatrix} E_{\theta,00} & E_{\theta,01} & E_{\theta,10} & E_{\theta,11} \end{bmatrix}^T = \frac{\sin(M\theta)}{\Delta^2}\cdot$$
$$\begin{bmatrix} 0 & -R_0 & R_0(R_0+\Delta) & 0 \\ 0 & R_0+\Delta & -R_0(R_0+\Delta) & 0 \\ -\Delta R_0 & R_0 & -R_0(R_0+\Delta) & \Delta R_0(R_0+\Delta) \\ \Delta(R_0+\Delta) & -(R_0+\Delta) & R_0(R_0+\Delta) & -\Delta R_0(R_0+\Delta) \end{bmatrix} \begin{bmatrix} 1 \\ z-Z_0 \\ \frac{z-Z_0}{r} \\ \frac{1}{r} \end{bmatrix} \tag{5.16}$$

We now define the E_θ subgrid basis functions on the $\Delta/N \times \Delta/N$ grid in the same way as in (2), replacing Δ by Δ/N for a subgrid cell extending from $r = R_0$ to $r = R_0 + \Delta/N$ and from $z = Z_0$ to $z = Z_0 + \Delta/N$ (and similarly if the origin of the cell is located elsewhere). It then follows that the E_θ basis functions on a coarse cell, being linear combinations of 1, z, z/r and $1/r$, can be written as linear combinations of the E_θ functions on the finer cells nested in the coarse cell. The same reasoning applies to the E_r basis functions which form a basis for all linear combinations of 1 and z, the E_z basis functions for 1 and r, the B_r basis functions for $1/r$ and 1, the B_z basis functions for $1/r$ and z/r and the B_θ functions for 1.

5.2.5 Grid assembling

Following [8], we now proceed to assemble cells into a complete mesh. The starting point is a coarse and a fine mesh that are still unconnected. Next, restriction operators that combine field quantities at each subgridding edge are introduced.

On the edges of the fine grid, only field quantities of the coarse grid are retained, as will become clear from a small example below. However, in order to guarantee stability, the restriction operators must obey certain commutation properties. Let A_E be the restriction operator for the electric fields and A_B for the magnetic inductions. Using these operators, the Maxwell curl equations for the *complete* mesh become

$$C_{joint}\mathbf{e}(t) = -\frac{d\mathbf{b}(t)}{dt} \tag{5.17}$$

$$[\star_\epsilon]^{-1} C^T_{joint} [\star_\mu^{-1}] \mathbf{b}(t) = \frac{d\mathbf{e}(t)}{dt} \tag{5.18}$$

$$[\star_\epsilon] = A_E [\star_\epsilon]_{disjoint} A_E^T \tag{5.19}$$

$$[\star_\mu^{-1}] = A_B [\star_\mu^{-1}]_{disjoint} A_B^T \tag{5.20}$$

$$C_{joint} = (A_B A_B^T)^{-1} A_B C_{disjoint} A_E^T \tag{5.21}$$

with $A_E C^T_{disjoint} = C^T_{joint} A_B$. The subscript *disjoint* indicates that the corresponding curl and mass matrices are those as derived in previous sections. Suppose the original disjoint grids have $N_{B,c}$ and $N_{B,f}$ magnetic field discretization points and $N_{E,c}$ and $N_{E,f}$ electric field discretization points. Subscripts c and f indicate coarse resp. fine grid cells. $N_{E,\cap}$ of the fine electric field discretization points and $N_{B,\cap}$ of the fine magnetic field discretization points are on the subgridding edge. For a rectangular subgrid, A_E is a $(N_{E,c} + N_{E,f} - N_{E,\cap}) \times (N_{E,c} + N_{E,f})$ matrix and A_B is a $(N_{B,c} + N_{B,f} - N_{B,\cap}) \times (N_{B,c} + N_{B,f})$ matrix.

To clarify the above concepts, the reader can of course consult [8], but as this paper deals with the BOR-FDTD case with its very specific arrangement of basis functions, let us take a look at a typical restriction process. We first consider the case in which a complete mesh consisting of identical cells is assembled, i.e. only coarse cells are present. Let us concentrate on the magnetic induction, the electric fields can be treated analogously. Fig. 5.2 shows a simple example consisting of two cells. To the left (Fig. 5.2a) the cells are shown separately and the positions of the B-field basis functions are indicated by the black dots. To the right (Fig. 5.2b) the cells have been assembled into "the mesh" and a global numbering is introduced. For this example we have that $N_{B,c} = 2 \times 5$ and $N_{B,\cap} = 1$. Collecting all the original magnetic induction basis functions in the 10×1 column vector $\mathbf{b}_{disjoint} = [b_1, ..., b_{10}]^T$ and the ones pertaining to the mesh of Fig. 5.2b in the 9×1 column vector $\mathbf{b}_{joint} = [b_1, ..., b_9]^T$, we have that $\mathbf{b}_{joint} = A_B \mathbf{b}_{disjoint}$ with A_B the 9×10 magnetic induction restriction matrix. The non-zero elements of this matrix are given by: $A_{B,1,1} = A_{B,1,8} = A_{B,2,2} = A_{B,3,3} = A_{B,4,4} = A_{B,5,5} = A_{B,6,6} = A_{B,7,7} = A_{B,8,9} = A_{B,9,10} = 1$. Note that all non-zero values are identical and equal to one. Of course, adding more cells will lead to additional couplings. Here only a coupling in a single point occurs. For the electric fields the same example leads to three coupled basis functions and with an analogous notation as above we have that $\mathbf{e}_{joint} = A_E \mathbf{e}_{disjoint}$ with $\mathbf{e}_{disjoint}$ a 16×1 column vector, $\mathbf{e}_{joint}$ a 13×1 column vector and A_E the 13×16 electric field restriction matrix (with 16 non-zero entries equal to one).

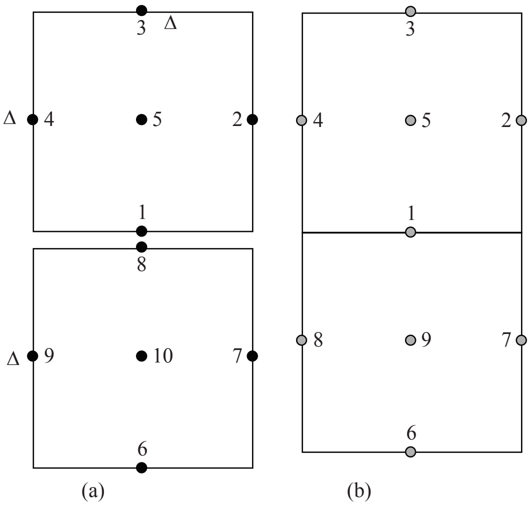

Figure 5.2: (a) two cells with anchor points and numbering for the magnetic induction basis functions. (b) assembled cells with global numbering.

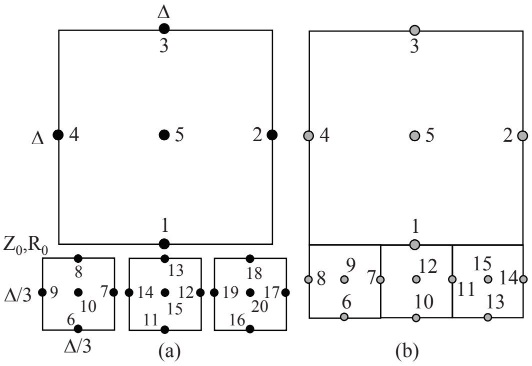

Figure 5.3: (a) one coarse mesh cell and 3 fine mesh cells with numbering for the magnetic induction basis functions. (b) assembled cells with global numbering.

Let us now turn to a subgridding example. Fig. 5.3a shows a single coarse cell and 3 fine mesh cells ($N = 3$) before fusing them together. Fig. 5.3b displays the resulting connected mesh. Note that in the connected mesh only coarse mesh field values are used at the edge connecting the coarse and the fine mesh. For this subgridding example we now have that $N_{B,c} = 5$, $N_{B,f} = 3 \times 5$ and $N_{B,\cap} = 3+1+1$, i.e. the 3 fine mesh points labeled $8, 13$ and 18 and 2 points to connect the fine mesh cells between them, the points labeled 7 and 12. For points 1, 8, 13 and 18 the corresponding expansion functions of interest, leaving out the $\sin(M\theta)$ factor, are:

$$B_{z,c} = \frac{(R_0 + \Delta/2)}{r}\left(1 - \frac{z - Z_0}{\Delta}\right) \tag{5.22}$$

$$B_{z,fi} = \frac{(R_0 + (i-1/2)\Delta/3)\sin(M\theta)}{r}\left(1 + 3\frac{z - Z_0}{\Delta}\right) \tag{5.23}$$

with $i = 1, 2, 3$, for resp. points 8, 13 and 18. From the above it is clear that the coarse cell basis function at $z = Z_0$, i.e. at the subgridding edge, can be written as the following linear combination of fine cell functions:

$$B_{z,c}\Big|_{z=Z_0} = \\ \left(\frac{R_0 + \Delta/2}{R_0 + \Delta/6}B_{z,f1} + B_{z,f2} + \frac{R_0 + \Delta/2}{R_0 + 5\Delta/6}B_{z,f3}\right)\Bigg|_{z=Z_0} \tag{5.24}$$

This is a simply illustration of the general properties announced in Section 5.2.4. Note that (18) guarantees pointwise B_z flux continuity along the subgridding edge. In this subgridding example the 15×20 magnetic induction restriction matrix A_B again satisfies $\mathbf{b}_{joint} = A_B\mathbf{b}_{disjoint}$, with $\mathbf{b}_{joint}$ resp. $\mathbf{b}_{disjoint}$ a 15×1 resp. 20×1 column vector. The 20 non-zero elements of A_B for this case are given by: $A_{B,1,1} = A_{B,2,2} = A_{B,3,3} = A_{B,4,4} = A_{B,5,5} = A_{B,6,6} = A_{B,7,7} = A_{B,7,14} = A_{B,8,9} = A_{B,9,10} = A_{B,10,11} = A_{B,11,12} = A_{B,11,19} = A_{B,12,15} = A_{B,13,16} = A_{B,14,17} = A_{B,15,20} = 1$, $A_{B,1,8} = \frac{R_0+\Delta/2}{R_0+\Delta/6}$, $A_{B,1,13} = 1$ and $A_{B,1,18} = \frac{R_0+\Delta/2}{R_0+5\Delta/6}$. The last three elements correspond to the basis functions coefficients in the r.h.s. of (18) or, put differently, the first row of A_B enforces identity (18).

5.2.6 Mass lumping

By now, the grid assembly process should be clear. However, before turning to the time-stepping part of the algorithm, special attention has to be devoted to the mass matrices $[\star_\epsilon]$ and $[\star_\mu^{-1}]$ in (14). Although the original mass matrices for a single BOR-FDTD cell are diagonal (see the end of Section 5.2.3) the assembly operators can reintroduce non-diagonal elements and here again some type of mass lumping will have to be introduced if we want to preserve the diagonal character and hence the explicit time-stepping properties. Let us again look at an elucidating example in which the assembly process leads to a non-diagonal $[\star_\epsilon]$ matrix. Fig. 5.4 shows a single coarse cell and, for the sake of simplicity, two fine mesh cells, before and

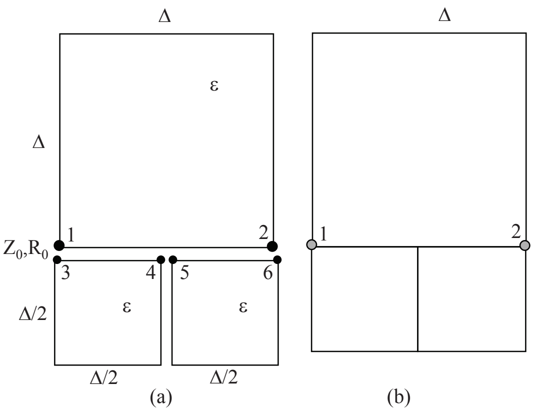

Figure 5.4: Relevant to mass lumping for $\vec{E}_\theta$: (a) one coarse mesh cell and 2 fine mesh cells with anchor points and numbering for the $\vec{E}_\theta$ basis functions; (b) assembled cells with global numbering.

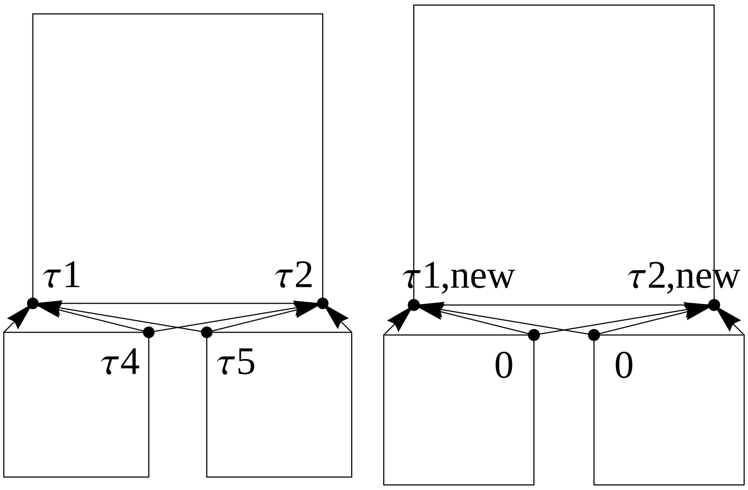

Figure 5.5: The "mass" associated with the fine basis functions that couple to multiple coarse basis functions is redistributed.

after fusing them together. We concentrate on the E_θ field components on the subgridding boundary, six in total in the original configuration with two of them (the coarse grid points) remaining after assembling the coarse cell with the two fine ones. The relevant expansion functions are given by:

$$\begin{array}{cc}
E_{\theta,1c} = Z_c(z)\frac{R_0}{\Delta}\left(\frac{R_0+\Delta}{r}-1\right) & E_{\theta,2c} = Z_c(z)\frac{R_0+\Delta}{\Delta}\left(1-\frac{R_0}{r}\right) \\
E_{\theta,3f} = Z_f(z)\frac{2R_0}{\Delta}\left(\frac{R_0+\Delta/2}{r}-1\right) & E_{\theta,4f} = Z_f(z)\frac{R_0+\Delta/2}{\Delta/2}\left(1-\frac{R_0}{r}\right) \\
E_{\theta,5f} = Z_f(z)\frac{R_0+\Delta/2}{\Delta/2}\left(\frac{R_0+\Delta}{r}-1\right) & E_{\theta,6f} = Z_f(z)\frac{R_0+\Delta}{\Delta/2}\left(1-\frac{R_0+\Delta/2}{r}\right) \\
Z_c(z) = \left(1-\frac{z-Z_0}{\Delta}\right) & Z_f(z) = \left(1+2\frac{z-Z_0}{\Delta}\right)
\end{array}$$

The pertinent linear combination of fine cell basis functions, to obtain the corresponding coarse ones, is:

$$E_{\theta,1c}\Big|_{z=Z_0} = E_{\theta,3f} + \alpha\left(E_{\theta,4f}+E_{\theta,5f}\right)\Big|_{z=Z_0} \tag{5.25}$$

$$E_{\theta,2c}\Big|_{z=Z_0} = E_{\theta,6f} + \beta\left(E_{\theta,4f}+E_{\theta,5f}\right)\Big|_{z=Z_0} \tag{5.26}$$

$$\alpha = \frac{R_0}{2(R_0+\Delta/2)} \tag{5.27}$$

$$\beta = \frac{R_0+\Delta}{2(R_0+\Delta/2)} \tag{5.28}$$

Only considering the six basis functions in the example, the 2×6 electric field restriction matrix A_E has 8 non-zero entries: $A_{E,1,1} = A_{E,1,3} = A_{E,2,2} = A_{E,2,6} = 1$, $A_{E,1,4} = A_{E,1,5} = \alpha$ and $A_{E,2,4} = A_{E,2,5} = \beta$, while the diagonal entries of the disjoint electric field mass matrix $[\star_\epsilon]_{disjoint}$ are:

$$\begin{aligned}
&(\tau_1,\tau_2,\tau_3,\tau_4,\tau_5,\tau_6) = \\
&\quad \frac{\epsilon\pi\Delta^2 R_0}{16}\left(4, 4(1+\Delta'), 1, 1+\Delta'/2, 1+\Delta'/2, 1+\Delta'\right)
\end{aligned} \tag{5.29}$$

We have, for simplicity, assumed that the value of ϵ does not change from one cell to the other. All this finally implies that the corresponding electric field 2×2 mass matrix $[\star_\epsilon]$ of the joined cells has the following elements:

$$\epsilon_{11} = \tau_1 + \tau_3 + \alpha^2(\tau_4+\tau_5) \tag{5.30}$$

$$\epsilon_{12} = \epsilon_{21} = \alpha\beta(\tau_4+\tau_5) \tag{5.31}$$

$$\epsilon_{22} = \tau_2 + \tau_6 + \beta^2(\tau_4+\tau_5) \tag{5.32}$$

showing that the grid assembling process can give rise to non-diagonal mass matrices.
To prevent the restriction operator from introducing these non-diagonal elements the following procedure has to be adopted:

1) Identify the disjoint basis functions which couple to multiple joint basis functions. In the example of Fig. 5.4 these disjoint basis functions are those associated

with anchor point 4 and 5. In general this amounts to identifying columns in the restriction matrix with more than one non-zero element.

2) Set the corresponding elements on the diagonal of $[\star_\epsilon]_{disjoint}$ to zero. In our example this implies that τ_4 and τ_5 must be set to zero.

3) For each of the considered disjoint basis functions, redistribute the original value on the diagonal over the multiple joint basis functions it couples with. The relevant joint basis functions are easily identified as they correspond to the row indices of the non-zero elements in the corresponding disjoint basis function column. In our example disjoint basis function 4 couples with joint basis functions 1 and 2 and the same is the case for disjoint basis function 5. In BOR-FDTD the number of joint basis functions that couple to multiple disjoint ones is at most two.

4) The redistribution over the two joint basis functions is carried out in such a way that the value added to $[\star_\epsilon]_{disjoint,jj}$ $(j = 1, 2)$, is proportional to $[\star_\epsilon]_{disjoint,jj}$ and that the trace of the $[\star_\epsilon]_{disjoint}$ matrix remains unaltered. The example of Fig. 5.4, in which a redistribution over two basis functions has to be carried out, will clarify the procedure. Both τ_4 and τ_5 have to be redistributed over τ_1 and τ_2 as follows:

$$\tau_{1,new} = \tau_1 + \frac{\tau_1}{\tau_1 + \tau_2}\tau_4 + \frac{\tau_1}{\tau_1 + \tau_2}\tau_5 = \tau_1 + \alpha(\tau_4 + \tau_5) \tag{5.33}$$

$$\tau_{2,new} = \tau_2 + \frac{\tau_2}{\tau_1 + \tau_2}\tau_4 + \frac{\tau_2}{\tau_1 + \tau_2}\tau_5 = \tau_2 + (1 - \alpha)(\tau_4 + \tau_5) \tag{5.34}$$

with $\alpha = \frac{\tau_1}{\tau_1+\tau_2}$. This redistribution is depicted in Fig. 5.5. Using these new values $\tau_{1,new}$ and $\tau_{2,new}$, with $\tau_{4,new} = \tau_{5,new} = 0$, the diagonal entries of $[\star_\epsilon]_{disjoint,new}$ become:

$$\begin{aligned}(\tau_{1,new}, &\tau_{2,new}, \tau_{3,new}, \tau_{4,new}, \tau_{5,new}, \tau_{6,new}) = \\ &\frac{\epsilon\pi\Delta^2 R_0}{16}\left(5, 5(1 + \Delta'), 1, 0, 0, 1 + \Delta'\right)\end{aligned} \tag{5.35}$$

It is easily verified that the total sum remains unaltered and that $\frac{\tau_1}{\tau_2} = \frac{\tau_{1,new}}{\tau_{2,new}}$.

5) With this new disjoint mass matrix, the new joint mass matrix can be determined. By construction, this matrix will now be diagonal. In our example we have

$$\epsilon_{11,new} = \tau_{1,new} + \tau_3 = \frac{3\epsilon\pi\Delta^2 R_0}{8} \tag{5.36}$$

$$\epsilon_{12,new} = \epsilon_{21,new} = 0 \tag{5.37}$$

$$\epsilon_{22,new} = \tau_{2,new} + \tau_6 = \frac{3\epsilon\pi\Delta^2 R_0}{8}(1 + \Delta') \tag{5.38}$$

It should be noted that in BOR-FDTD only the E_θ components can give rise to a non-diagonal $[\star_\epsilon]$ matrix and to which the above procedure must be applied.

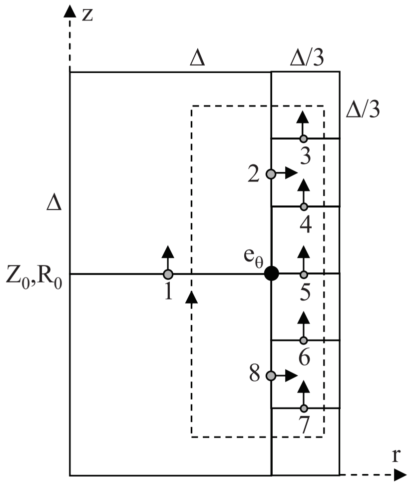

Figure 5.6: Updating of $\vec{E}_\theta$ at the subgrid edge $r = R_0$

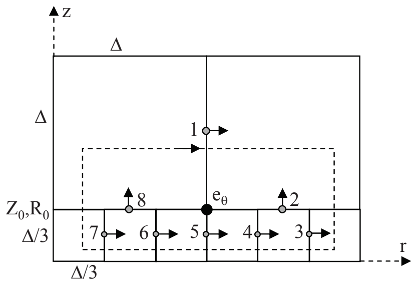

Figure 5.7: Updating of $\vec{E}_\theta$ at the subgrid edge $z = Z_0$

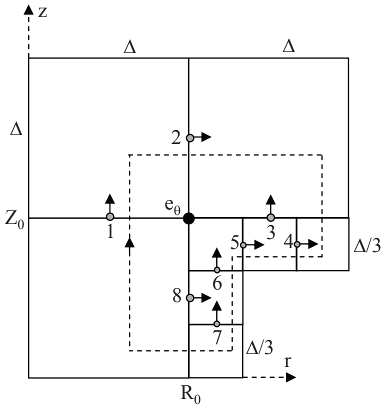

Figure 5.8: Updating of $\vec{E}_\theta$ at subgrid corner $r = R_0$, $z = Z_0$.

5.2.7 Leapfrog time stepping

The final BOR-FDTD equations are given by (12) and (13). Time-stepping of these equations is straightforward. It suffices to e.g. discretise **b** in (12) on whole time steps $n\Delta t$ and **e** on half time steps $(n+1/2)\Delta t$ to obtain the following leapfrog updating scheme:

$$\mathbf{b}_n = \mathbf{b}_{n-1} - C_{joint}\mathbf{e}_{n-1/2}\Delta t \tag{5.39}$$

$$\mathbf{e}_{n+1/2} = \mathbf{e}_{n-1/2} + [\star_\epsilon]^{-1} C_{joint}^T [\star_\mu^{-1}] \mathbf{b}_n \Delta t \tag{5.40}$$

This can be cast into the following form

$$\begin{bmatrix}\tilde{\mathbf{e}}_{n+1/2} & \tilde{\mathbf{b}}_n\end{bmatrix}^T = \begin{bmatrix}\mathbf{I}-\tilde{C}^T_{joint}\tilde{C}_{joint}(\Delta t)^2 & \tilde{C}^T_{joint}\Delta t] \\ -\tilde{C}_{joint}\Delta t & \mathbf{I}\end{bmatrix}\begin{bmatrix}\tilde{\mathbf{e}}_{n-1/2} \\ \tilde{\mathbf{b}}_{n-1}\end{bmatrix} \tag{5.41}$$

or $\mathbf{u}_n = \mathbf{A}\mathbf{u}_{n-1}$, with $\mathbf{A}$ the so-called amplification matrix, $\tilde{\mathbf{e}} = [\star_\epsilon]^{1/2}\mathbf{e}$, $\tilde{\mathbf{b}} = [\star_\mu^{-1}]^{1/2}\mathbf{b}$ and $\tilde{C}_{joint} = [\star_\mu^{-1}]^{1/2}C_{joint}[\star_\epsilon]^{-1/2}$. The reader is referred to [8] for a proof of the stability of this leapfrog scheme both in the absence and presence of subgridding, provided the time step Δt respects the Courant limit of the size of the smallest grid, i.e. $c\Delta t \leq \Delta_{finest}/f(M)$, where $f(M)$ is roughly proportional to M [22]. All eigenvalues of $\mathbf{A}$ are located on the unit circle.

Equations (5.39) and (5.40) suffice to write down an algorithm. However, starting from these equations it is elucidating to see how the proposed method takes care of the updating at subgridding boundaries. Let us start with b_r. Looking at Fig. 1 and supposing that b_r is on a subgridding edge (say at $r = R_0$) and because after assembling the grid we only use coarse grid values, updating of b_{r1} requires the value of e_{z1} at the same place and the neighboring $e_{\theta,00}$ and $e_{\theta,10}$ values. To obtain the necessary value of e_θ at $z = Z_0 + \Delta/2$, (36) will enforce a linear interpolation, i.e. the e_θ value used at $z = Z_0 + \Delta/2$ will simply be $\frac{e_{\theta,00}+e_{\theta,10}}{2}$. This is of course what we would have expected right away. An analogous reasoning holds when updating b_z. For b_{z1} e.g. the value of e_{r1} at the same place and the neighboring $e_{\theta,10}$ and $e_{\theta,11}$ values are needed. To obtain the necessary value of e_θ at $r = R_0 + \Delta/2$, (36) now enforces an interpolation using the functions $f_1(r)$ and $f_2(r)$ defined in (2), i.e.

$$e_{\theta,r=R_0+\Delta/2} = f_1(r)e_{\theta,10} + f_2(r)e_{\theta,11} \tag{5.42}$$

Coarse b_θ components always have coarse e_r and e_z neighbors and updating them is never problematic. Fine b_θ near the subgridding boundary are updated directly using the neighboring coarse e_r and/or e_z.

Updating e-fields at subgridding boundaries turns out to be more complicated. This will be illustrated by the subgridding example of Fig. 5.3 studied above. We will use the numbering convention of Fig. 5.3b. To update $e_{r,1}$ ($r = R_0 + \Delta/2$, $z = Z_0$) we need the coarse value of $b_{z,1}$ at the same point, the coarse grid value $b_{\theta,5}$ at $r = R_0 + \Delta/2$, $z = Z_0 + \Delta/2$ and three fine b_θ values, i.e. $b_{\theta,9}$, $b_{\theta,12}$ and $b_{\theta,15}$ all at $z = Z_0 - \Delta/6$ and resp. at $r = R_0 + \Delta/6$, $r = R_0 + \Delta/2$ and $r = R_0 + 5\Delta/6$. Eqn. (5.40) leads to the following weighted value of $e_{r,1}$:

$$\epsilon\mu\frac{de_{r,1}}{dt} = \frac{-3}{2\Delta}b_{\theta,5} - Mb_{z,1}\left(\frac{1}{12}\frac{1}{R_0+\Delta/6} + \frac{1}{12}\frac{1}{R_0+5\Delta/6} + \frac{10}{12}\frac{1}{R_0+3\Delta/6}\right)$$
$$+\left(\frac{1}{2\Delta} - \frac{1}{6(R_0+\Delta/2)}\right)b_{\theta,9} + \left(\frac{1}{2\Delta}\right)b_{\theta,12} + \left(\frac{1}{2\Delta} + \frac{1}{6(R_0+\Delta/2)}\right)b_{\theta,15} \tag{5.43}$$

We have again restricted ourselves to the simple case of a completely homogeneous medium with material parameters ϵ and μ. An analogous reasoning holds when updating e_z. Suppose that we take a similar example as in Fig. 5.3 but that we now place the subgridding boundary at $r = R_0 + \Delta$. Let us stick to the numbering of Fig. 5.3b by counterclockwise rotating the figure over 90 degrees. To update $e_{z,1}$ ($r = R_0 + \Delta$, $z = Z_0 + \Delta/2$) we now need the course value of $b_{r,1}$ at the same point, the coarse grid value $b_{\theta,5}$ at $r = R_0 + \Delta/2$, $z = Z_0 + \Delta/2$ and three fine b_θ values, i.e. $b_{\theta,9}$, $b_{\theta,12}$ and $b_{\theta,15}$ all at $r = R_0 + 7\Delta/6$ and resp. at $z = Z_0 + \Delta/6$, $z = Z_0 + \Delta/2$ and $z = Z_0 + 5\Delta/6$. Eqn. (5.40) now shows that the corresponding weighted value of $e_{z,1}$ is:

$$\begin{aligned}\epsilon\mu\frac{de_{z,1}}{dt} &= \frac{-3}{2\Delta}\frac{R_0+\Delta/2}{R_0+\Delta}b_{\theta,5} - \frac{M}{R_0+\Delta}b_{r,1} && (5.44)\\ &+ \frac{1}{2\Delta}\frac{R_0+\Delta(1+1/6)}{R_0+\Delta}(b_{\theta,9}+b_{\theta,12}+b_{\theta,15}) && (5.45)\end{aligned}$$

The updating formula for e_z is simpler than the one for e_r. This is a consequence of the fact that in the z-direction linear interpolation intervenes while in the r-direction a more complicated updating as in (38) plays a role: in cylindrical coordinates, ”up” and ”down” are equivalent, but ”left” and ”right” are not.

The updating strategy for e_θ is more complicated and depends on the exact position of the anchor point. Figs. 5.6, 5.7 and 5.8 shows the three possible situations. In Fig. 5.6, e_θ is located at an r is constant edge, here at $r = R_0 + \Delta$ with $z = Z_0 + \Delta$. To update e_θ neighboring values of b_z and b_r are needed. From (5.40) one derives that

$$\epsilon\mu\frac{de_\theta}{dt} = \frac{3}{2\Delta}b_{z,1} + \frac{1}{\Delta}(b_{r,2}-b_{r,8}) - \frac{1}{6\Delta}(b_{z,3}+b_{z,7}) - \frac{1}{3\Delta}(b_{z,4}+b_{z,6}) - \frac{1}{2\Delta}b_{z,5} \tag{5.46}$$

In points 1, 2 and 8 course grid values are used, in the other ones fine grid values. Fig. 5.7 shows the analogous case for updating e_θ at an z is constant edge, here at $z = Z_0$ with $R = R_0 + \Delta$. The update equation now becomes:

$$\begin{aligned}\epsilon\mu\frac{de_\theta}{dt} &= \frac{3}{2\Delta}b_{r,1} + (b_{z,2}-b_{z,8})\left(\frac{-1}{\Delta}+\frac{1}{6}\left(\frac{1}{6R_0+11\Delta}-\frac{1}{6R_0+7\Delta}\right)\right)\\ &- \frac{1}{6\Delta}(e_{r,3}+e_{r,7}) - \frac{1}{3\Delta}(b_{r,4}+b_{r,6}) - \frac{1}{2\Delta}b_{r,5} && (5.47)\end{aligned}$$

Here again, in points 1, 2 and 8 course grid values are used, in the other ones fine grid values. The most intricate situation arises when e_θ is located at a corner point as shown in Fig. 5.8 for $z = Z_0$ and $R = R_0$. In this case we have that

$$\begin{aligned}\epsilon\mu\frac{de_\theta}{dt} &= \frac{9}{8\Delta}(b_{z,1}+b_{r,2}) + (\frac{-3}{4\Delta}+\frac{1}{8(6R_0+5\Delta)}-\frac{1}{8(6R_0+\Delta)})b_{z,3}\\ &- \frac{1}{8\Delta}(b_{r,4}+b_{z,7}) - \frac{1}{4\Delta}(b_{r,5}+b_{z,6}) - \frac{3}{4\Delta}b_{r,8} && (5.48)\end{aligned}$$

Coarse grid point are at 1, 2, 3 and 8, fine ones at 4, 5, 6 and 7. By the dashed lines in Figs. 5.6, 5.7 and 5.8 we have indicated the way in which the anchor points are

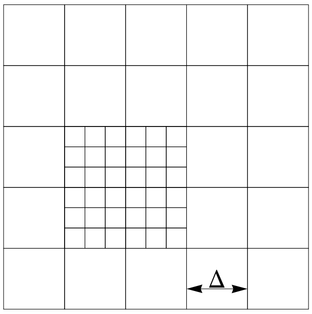

Figure 5.9: A simple configuration for the exact eigenspectrum calculation.

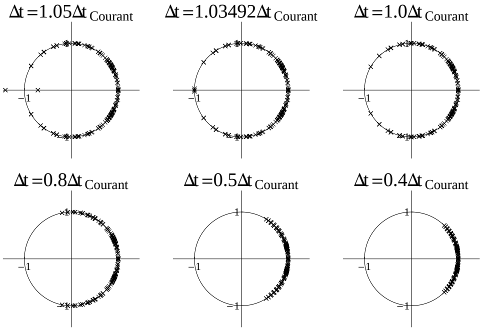

Figure 5.10: The eigenspectrum of the discrete amplification matrix for the simple configuration of Fig. 5.9 and for various values of Δt.

ordered when calculating the corresponding time derivative of the e_θ field component. This reminds one of Ampère's law but one should be careful when wanting to interpret the obtained formula's in this way. In the absence of subgridding the restriction operators A_E and A_B only have 1 and 0 entries. In the subgridding case however these operators and also $[\star_\epsilon]$ and $[\star_\mu^{-1}]$ will depend on the explicit form of the curl-operator (8) and hence on the curl inclusion properties of the basis functions. Consequently, the proposed method imposes a strong relationship between the time-domain updating equations at the subgridding boundaries and the specific form of the curl operator.

5.2.8 Numerical results

First, stability, grid reflection and grid dispersion are investigated. Next the accuracy of the method is illustrated by determining the resonance frequencies of a toroidal cavity. This is followed by the study of a reentrant cylindrical particle accelerator cavity, showing that subgridding can substantially reduce CPU-time and memory requirements while retaining accuracy. Further research will focus on plasma applications, the results of which will be presented elsewhere.

Stability

In what follows we consider toroidal cavities (except for the cylindrical cavity example of Section 5.2.8) with PEC boundaries and focus on a particular angular mode with index M implying a $\cos(M\theta)$ dependence for e_r, e_z and b_θ and a $\sin(M\theta)$ dependence for e_θ, b_r and b_z.

In a first example we explicitly calculated the 349 eigenvalues of the amplification matrix $\mathbf{A}$ for the very simple configuration of Fig. 5.9 and for $M = 27$. The problem space counts 5×5 course grid cells of 1cm by 1cm, four of which have been subdivided in 9 fine grid cells. The cavity is filled with air, $R_0 = 2m$ and

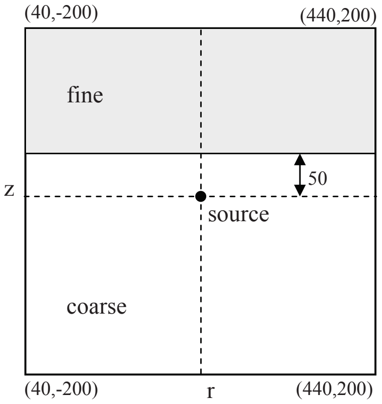

Figure 5.11: Simulation domain for grid reflection and grid dispersion calculations.

$z_0 = 0m$ (but the results remain completely invariant under a change of z_0). The behavior of the eigenvalues versus Δt is shown in Fig. 5.10. For a suitable choice of Δt obeying the Courant condition ($\Delta t = \Delta_{Courant}$) for the smallest cells, i.e. $c\Delta t = \frac{\Delta}{3\sqrt{2}} \approx 0.236\Delta$, all eigenvalues are on the unit circle. as shown in Fig. 5.10. For a smaller time step, these eigenvalues move on the unit circle towards point $(1, 0)$ as in Fig. 5.10 for $c\Delta t = 0.8, 0.5$ and $0.4\Delta_{Courant}$. However, one remarks that when increasing Δt slightly beyond the Courant limit, up to $c\Delta t = 1.03492\Delta_{Courant}$, stability is still preserved. We again refer to [8] for a thorough discussion, proving that the mass lumping in most cases results in an improved stability. When further increasing Δt, as shown in Fig. 5.10 for $c\Delta t = 1.05\Delta_{Courant}$, a negative real eigenvalue outside the unit circle is found and the time stepping will no longer remain stable. Note that in classical BOR-FDTD [22], the time step must be chosen roughly inversely proportional to the angular mode number. Since we do not consider cells close to the $r = 0$ axis, we can use a time-step much larger than in BOR-FDTD while still preserving stability. As remarked by one of the reviewers, having all eigenvalues on the unit circle is a necessary but not a sufficient condition for stability. The eigenvalues on the unit circle must also be simple or nondefective [28].

Although the eigenspectrum results above indeed confirm the theoretical underpinning of the theory given in [7], asserting that the subgridding methodology we used automatically leads to a stable algorithm, we further assessed the long term stability in the examples given below in Section 5.2.8, by letting the algorithm run for a very large amount of time steps, i.e. several 10^5 steps. No instability could be detected.

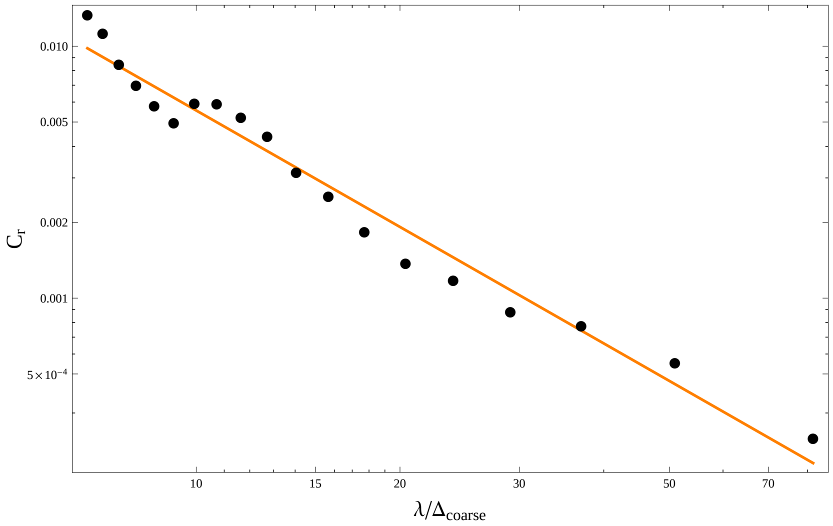

Figure 5.12: Grid reflection at the subgridding boundary

Grid reflection

Ideally, waves should propagate into the subgridded area without any reflection. To investigate the behavior of our technique, a sinusoidal line source with a $M = 0$ (i.e. θ-independent source) in the toroidal direction and with a wavelength $\lambda = N\Delta_{coarse}$ was used, with N ranging between 6 and 100. The cross-section of the considered configuration is that of Fig. 5.11. The simulation domain measures 200 by 200 $\Delta_{coarse} \times \Delta_{coarse}$ cells with the left boundary located at $40\Delta_{coarse}$ from the axis. The intersection point S of the source loop with the (r,z)-plane is located in the center of the simulation domain. In the lower part of the simulation domain the course discretization Δ_{coarse} is used, while the upper gray part is subgridded with $\Delta_{fine} = \frac{\Delta_{coarse}}{2}$. The boundary between the subdomains is located at $50\Delta_{coarse}$ from the center. To assess the grid reflection, a first simulation is performed only using the course grid over the entire domain. The total simulation time is chosen such that the waves do not yet reach the outer boundaries. In the second simulation the coarse grid is used in the lower subdomain and the fine in the upper subdomain. The reflection coefficient plotted in Fig. 5.12 is defined as

$$C_r = \frac{avg(|(E_\theta)_2 - (E_\theta)_1|)}{avg(|(E_\theta)_1|} \tag{5.49}$$

C_r is the average absolute difference between the θ-component of the electric field in the second and first simulation, divided by the corresponding value in the first simulation, whereby the average is taken over all cells of the lower, i.e. coarse cell, subdomain. This reflection coefficient decreases quickly as the amount of

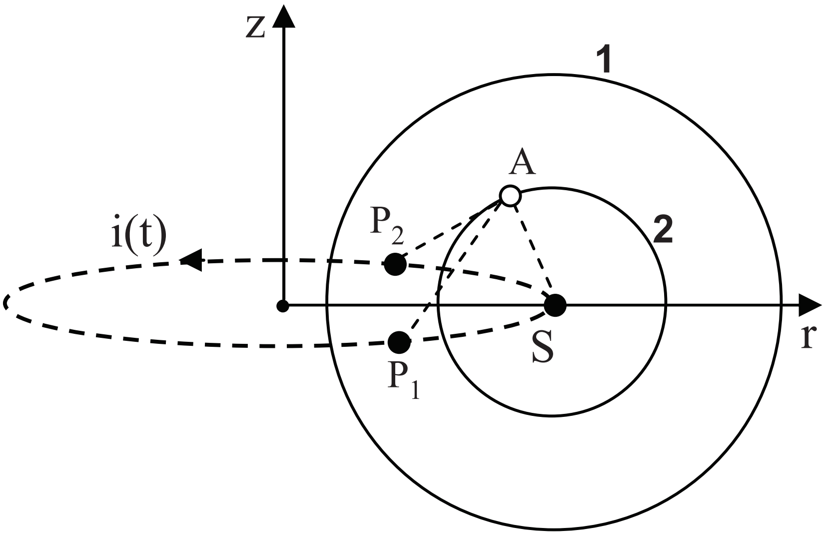

Figure 5.13: Current loop and field observation circles in the (r,z)-plane.

sampling points per wavelength increases, dropping below $6 \cdot 10^{-3}$ or 0.6% when $N \geq 10$. More important than the absolute value of C_r is the fact that C_r decreases as $(\frac{\lambda}{\Delta_{coarse}})^{-1.5}$ which is the value predicted by Monk [18] for 2D cartesian FDTD.

Grid dispersion

Another phenomenon commonly encountered in FDTD simulations is the direction-dependent speed of light due to the regular discretization grid. To investigate this dispersion, we again start from the configuration of Fig. 5.11. At $t = 0$ the current $i(t)$ in the loop (see also Fig. 5.13) is simultaneously switched on in all the points of the loop (corresponding to an $M = 0$ mode). The current then starts oscillating sinusoidally with circular frequency ω (whereby due care is taken to smoothly switch the current on). We now determine all field values in the (z,r)-plane at *a fixed instant* t_0 and we chose ct_0 to be $170\Delta_{coarse}$, with c the speed of light in vacuum and $\Delta_{coarse} = \lambda/7$. This implies that the wavefront in the (r,z)-plane of Fig. 5.13 will reach no further than the circle of radius $170\Delta_{coarse}$ centered on S. This particular wavefront (denominated “1") originates from the point S itself. Contributions from other points on the loop have to travel over a longer distance and cannot yet reach this outer wavefront. However, now consider another circular wavefront inside “1", such as the one denominated “2". Field contributions on this wavefront, e.g. in the point A, not only come from S but also from other parts of the loop, e.g. from the points P_1 and P_2. The smaller the wavefront radius, the larger the portion of the loop points of which can contribute. Contributions to “2" coming from S are obviously in phase. It is important to realize that contributions

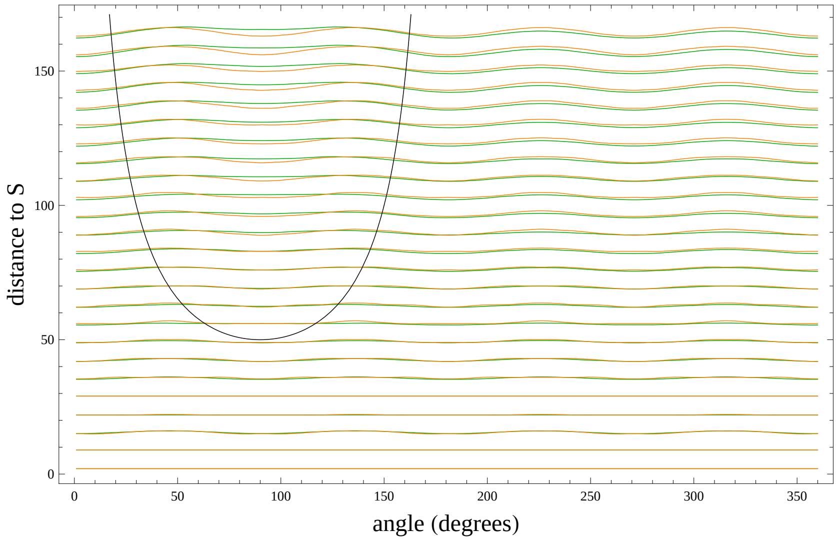

Figure 5.14: Distance between S and wave maxima/Δ_{coarse} vs. angle. Orange lines are without subgridding, green lines with subgridding. The black curve is the subgridding boundary.

to “2" e.g. coming from points P_1 and P_2 on the loop will also be in phase with the contributions from S. Indeed, although the fields originating from P_1 and P_2 have to travel over a larger distance, the extra phase shift this involves is compensated by the fact that when the signal was emitted at P_1 and P_2, the phase of the source loop in these points lags behind as compared to the phase of S at a later time. Or put differently: phase variations of the source points as a function of time and phase delays due to different path lengths compensate each other. The above reasonings lead to the following conclusion. When registering all fields at the fixed instant t_0, the fields will be in phase on circles such as “1" and “2" and indeed on any other circle centered on S. Consequently, field maxima (minima) will be found on some of these circles and such circles will be spaced by the wavelength. It must be emphasized that on such a “maximum" circle, the *value* of the maximum is *not* constant over the whole circle. Points on the circle closer to the center of the current loop will exhibit higher values than points further away. This is due to the 1/distance decrease of source point contributions.

The phenomena described above crucially depend on the direction independent velocity of light. Hence, grid dispersion and the influence of subgridding can be clearly assessed in this way. For the parameters given above ($ct_0 = 170\Delta_{coarse}$ and $\Delta_{coarse} = \lambda/7$) and for the non-subgridded case, the orange lines in Fig. 5.14 represent the numerically obtained loci of the maxima of the electric field. In order to give a clear picture of the results, we opted for a cartesian representation with the angle along the horizontal axis and with the distance to S, i.e the circle radius,

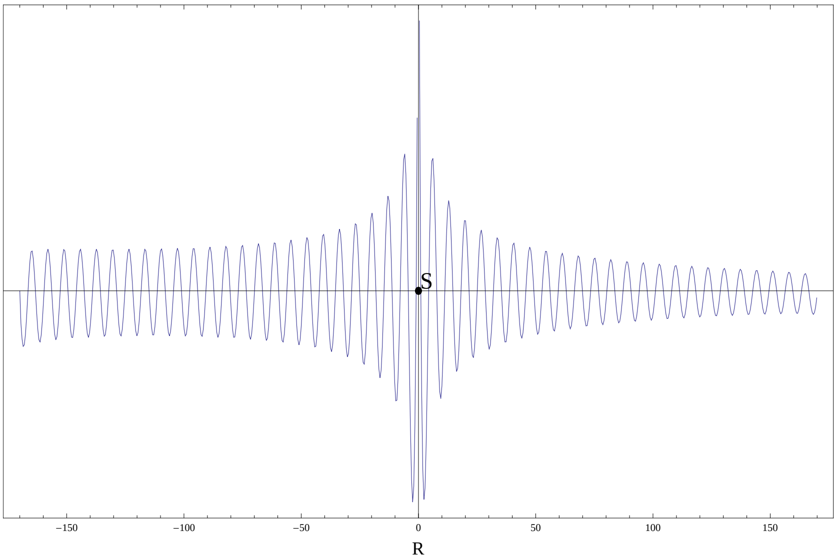

Figure 5.15: Electric field amplitude at t_0 along the r-axis.

along the vertical axis. Ideally all lines in Fig. 5.14 should be horizontal. It can be seen that with increasing distance to S, increasing dispersion errors become visible as an approximately 90°-periodic deviation from the ideal circles (i.e. horizontal lines in Fig. 5.14). This deviation is approximately 1.3% of the distance to S. One can also clearly see that the maxima are spaced by λ. The dispersion error decreases as the amount of discretization points per wavelength increases. For 14 points per λ we obtained a deviation of 0.4%.

Next, the numerical experiment was repeated while introducing subgridding ($\Delta_{fine} = 0.5\Delta_{coarse}$) in the gray part of Fig. 5.11, corresponding to the area inside the black curve on Fig. 5.14. It is clear that the dispersion error decreases inside the subgridded area as the green lines are flatter than the orange ones and that little or no additional dispersion error is visible at the subgridding edge. Finally, to make clear that the value of the maximum varies along each circle, some additional data are given in Fig. 5.15. This figure shows the electric field amplitude along the r-axis ($z = 0$) starting in the leftmost point of circle “1" and ending in its rightmost point. Remarks that the position of the maxima (and minima) is symmetrical with respect to the midpoint S. $R = 0$ corresponds to S itself. For corresponding maxima, the absolute value is higher to the left ($R < 0$) of S and the closer to S, the higher the value.

Toroidal cavity examples

As a next example consider a perfectly conducting torus with a square cross-section of inner radius 2 m, outer radius 4 m and a height of 2 m. As coarse discretization length we select Δ to be 1 cm and this coarse grid is combined with a fine grid with discretization length $\Delta/3 = 1/3$cm. This fine grid is an asymmetrically positioned square starting 60 cm from the left of the cavity (at $r = 2.6m$), and 60 cm from the bottom of cavity ($z = 60cm$) with side length 34cm. A line current in the toroidal direction at the center of the cavity, i.e. at a radius of 3 m, is used as the excitation. In the time-domain this source terms takes the form

$$j_\theta(t) = \cos(\omega_0 t) e^{-\left(\frac{t-t_0}{a}\right)^2} \tag{5.50}$$

with a Fourier spectrum proportional to

$$J_\theta(\omega) \propto e^{-j\omega_0 t_0} e^{-\frac{a^2}{4}(\omega-\omega_0)^2} + e^{j\omega_0 t_0} e^{-\frac{a^2}{4}(\omega+\omega_0)^2} \tag{5.51}$$

Choosing appropriate values for a, t_0 and ω_0 enables us to only excite frequencies within a frequency range of interest, taking care that t_0 is large enough such that $j_\theta(t = 0) \approx 0$. The time step $\Delta t = 1 \cdot 10^{-11}$ s is chosen slightly below the Courant limit with respect to the fine discretization length. First, we excite a low-frequency $M = 0$ mode in a vacuum-filled cavity using a line source of center frequency $\omega_0 = 600$ MHz, with $t_0 = 0.1\mu s$ and $a = 0.04\mu s$. From the Fourier transform of the simulation results in each point of the grid, it is easy to derive the resonance frequency that occurs. Both the subgridded and the non-subgridded simulations show a first resonance frequency at $\omega = 672$ MHz. The difference is below the frequency resolution. The analytical solution for the lowest-mode frequency is $\omega = 660$ MHz. The difference between the simulated results and the exact result is approximately 2%.

To further investigate the influence of the subgridding, a more complicated problem is considered by filling the cavity for $r > 3.5$ m with a dielectric material with $\epsilon = 9\epsilon_0$. Furthermore, we use a toroidal mode $M = 5$ and a higher-frequency source with a Gaussian spectrum centered at $\omega_0 = 3.3$ GHz, with $t_0 = 0.08\mu s$ and $a = 0.02\mu s$. The resulting spectrum is shown in Fig. 5.16. There is very little difference between the location of the resonance frequency in the subgridded and the non-subgridded case. A typical plot after 10^4 time steps of $|E_\theta|$ over the cross-section is shown in Fig. 5.17. The presence of the dielectric material is clearly visible. $|E_\theta|$ is nicely continuous everywhere and in particular at the subgridding edge. Furthermore, the subgridded area only barely disturbs the symmetry between the upper and lower halves of the configuration.

In a last simulation, we examined multilevel subgridding: a part of the subgridded area is itself subgridded (Fig. 5.18). Compared with a non-subgridded simulation, the resonance frequencies shift by about 0.4%. In all these examples, all simulations have run for at least $3 \cdot 10^5$ time steps and, as expected, no sign of instabilities has been observed.

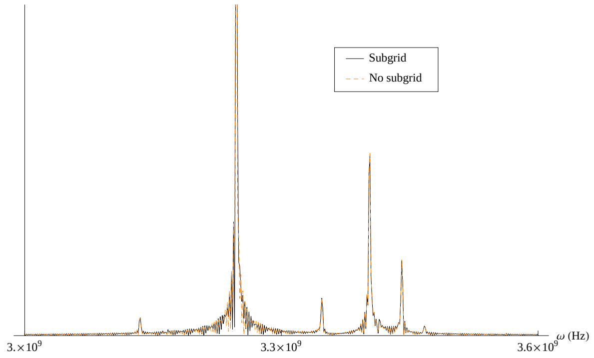

Figure 5.16: Comparison between a subgridded and a non-subgridded cavity for a toroidal M=5 mode with a resonance frequency near 3.25 GHz

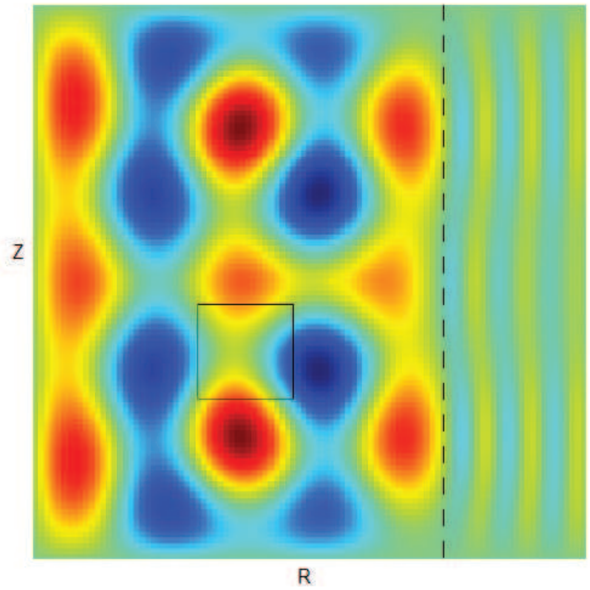

Figure 5.17: $|E_\theta|$ after 10^4 steps. The rectangle indicates the boundary of the subgridded domain.

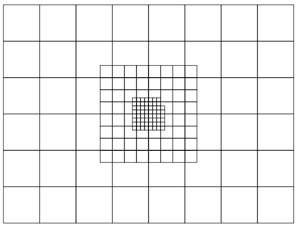

Figure 5.18: Multilevel subgridding

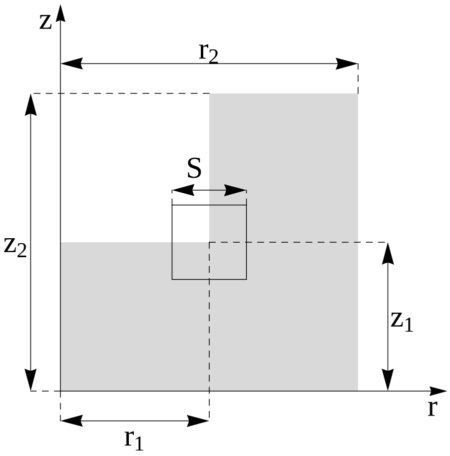

Figure 5.19: Reentrant cavity (gray) with sharp internal corner. The square of side $S = 3$ mm is the 1/2 subgridded part. $r_1 = 6.004$ mm, $r_2 = 42.29$ mm, $z_1 = 7.958$ mm, and $z = 22.792$ mm.

Reentrant cylindrical cavity

In [5, 23], the problem of calculating the resonant frequencies of reentrant cylindrical cavities, such as those encountered in Alvarez-type particle accelerators, is discussed. Due to the presence of sharp internal corners at which the electric field becomes large and varies strongly over a small distance, FDTD methods are hard to use for this kind of problem. Here, we will revisit the configuration of [5] (Fig. 5.19, Figs. 1 and 2 in [5]), first with a uniform fine discretisation, and then with subgridding near the sharp corner. In this way, we can obtain nearly the same result using only about $(1/2)^2 = 1/4$ of the memory needed for the fine discretization. Note that this is a cylindrical configuration, not a toroidal one, so some care must be taken to properly simulate the $r = 0$ axis. The subgridding does not intersect with the $r = 0$ axis, so our method reduces to classical BOR-FDTD there, allowing the use of the on-axis update equations described in [22].

At $M = 0$, it suffices to introduce some minor changes to the mass lumped electric mass matrix $[\star_\epsilon]$ to make this method give the correct BOR-FDTD equations at $r = 0$ as well.

The dimensions given in Fig. 5.19 are those of [5]. In a first simulation a uniform grid of size $\Delta = 0.1$ mm is used. After exciting the cavity using a time-domain source with a broad frequency spectrum, we fourier-transformed the result to find the lowest resonance peak at 2.1 GHz, as predicted in [5].

In a second simulation the overall discretization length was doubled to $\Delta = 0.2$ mm, except for a small subgridding square of side $S = 3$ mm around the internal corner (Fig. 5.19), where the discretization length remains fine at $\Delta = 0.1$ mm. By doing so, we decrease the memory used by the simulation by almost a factor 4. The running time decreases as well because almost 4 times less unknowns have to be updated every time step. Nevertheless, we still have to obey the Courant limit of the small cells and thus have to run the simulation for the same amount of time steps. The resulting fields are barely distinguishable from those of the uniform fine simulation. Most importantly, the excited resonance peak is still at 2.1 GHz.

5.2.9 Conclusions

We have extended the provably stable subgridding method of [7] to BOR-FDTD. Using appropriate mass-lumping techniques yields an explicit and stable time-stepping algorithm provided the Courant limit of the fine mesh cells is respected (although the mass-lumping can lead to a relaxing of this limit). The FDTD updating equations at subgrid edges and corners, resulting from the mathematical machinery, cannot readily be interpreted intuitively. Some simple cases provide the reader with the necessary insight. Several numerical examples, using toroidal cavities, have demonstrated that the proposed subgridding is indeed stable and by considering the eigenmodes of such cavities it is also shown that the method remains very accurate even in the case of multilevel subgridding. We also provided some data on the subgridding reflection and disperion behavior. Finally, a short study of the resonant behavior of an accelerator type reentrant cylindrical cavity, shows that subgridding can lead to savings in CPU time and memory while retaining accuracy.

In the future, we intend to extend our method to be able to subgrid plasmas instead of simple dielectrics. In that case the current and the constitutive equation connecting the current to the fields need to be treated in a special way (using an auxiliary differential equation).

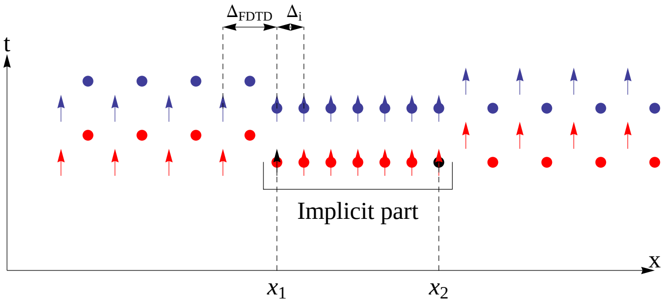

Figure 5.20: A hybrid explicit/implicit spatio-temporal grid.

5.3 Hybrid methods

5.3.1 Theory

In electromagnetism one often encounters wave equations which are well-behaved over large regions of space, and have difficult behaviour only in some small region (e.g. very short wavelengths in plasma physics or strong decay over a short distance in good electric conductors). It would be convenient to be able to use explicit methods (section 3.1) in the regions where the wave is well-behaved, and implicit methods (section 3.5) with smaller Δ in the other regions. To do this, some way of connecting both methods is required. Unsurprisingly, the finite element interpretation of both methods provides us with a way to do just that.

In figure 5.20, an 1D implicit grid is coupled on both sides to an explicit FDTD grid. Note that there are n implicit cells and $2n+2$ degrees of freedom associated with these cells. Every cell has 2 implicit time-stepping equations (as in figure 3.4), giving a total of $2n$ equations. Thus, we are left with two degrees of freedom on the explicit/implicit boundary for which a special equation will have to be constructed. By construction, we place one of these degrees of freedom on the left interface and one on the right.

In what follows, we will concentrate on the $x = x_2$ case, i.e. the right interface. In the finite-element interpretation, we connect the triangular implicit basis-function to the rectangular explicit basis-function (figure 5.21 , bottom). We deform the triangular electric basis-functions for the special case where the distance between neighbouring electric discretisation points is only $\frac{\Delta_{FDTD}}{2}$, as shown in the top of figure 5.21. We test the resulting basis-functions with the normal implicit test-function (red dashed in figure 5.21).

The spatially-interpolated temporal derivative of the magnetic field remains as it was in a purely implicit method. Only the temporally-interpolated spatial derivative of the electric field changes: on the left, it uses two temporaly-separated electric field points as input (as usual), but on the right, it now uses two spatially-

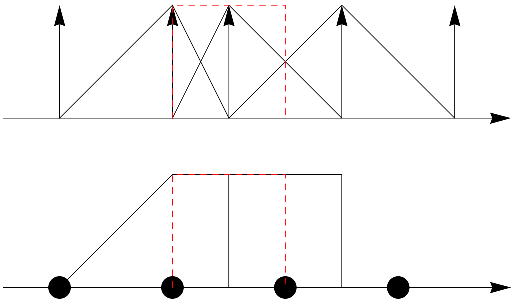

Figure 5.21: Modified electric and magnetic basis-functions at the explicit/implicit interface

separated electric field points.

$$\begin{aligned}&\frac{\frac{1}{2}\left(B_y(x,t+\Delta_t)+B_y(x+\Delta_{FDTD},t+\Delta_t)\right)-\frac{1}{2}\left(B_y(x,t)+B_y(x+\Delta_{FDTD},t)\right)}{\Delta_t}\\ &\quad=\frac{1}{2\Delta_{FDTD}}\left(E_z(x+\Delta_{FDTD}/2,t+\Delta_t/2)+E_z(x+3\Delta_{FDTD}/2,t+\Delta_t/2)\right)-\\ &\qquad\qquad\frac{1}{2\Delta_{FDTD}}\left(E_z(x,t)+E_z(x,t+\Delta_t)\right)\end{aligned} \tag{5.52}$$

The left-hand side is the usual implicit spatial interpolation of the time derivative, this time using 2 implicit and 2 explicit points, which naturally exist at the correct positions. The right-hand side interpolates two explicit E_z at $\Delta_{FDTD}/2$ and $3\Delta_{FDTD}/2$ from the interface to get E_z at Δ_{FDTD} from the interface. This is used together with 2 implicit E_z at the interface to end up with a spatial derivative located at the same spatio-temporal position as the interpolated time derivative. A similar equation updates E_z at the left interface ($x = x_1$).

$$\begin{aligned}&\epsilon_0\mu_0\frac{\frac{1}{2}\left(E_z(x,t+\Delta_t)+E_z(x-\Delta_{FDTD},t+\Delta_t)\right)-\frac{1}{2}\left(E_z(x,t)+E_z(x-\Delta_{FDTD},t)\right)}{\Delta_t}\\ &\quad=-\frac{1}{2\Delta_{FDTD}}\left(B_y(x-\Delta_{FDTD}/2,t+\Delta_t/2)+B_y(x-3\Delta_{FDTD}/2,t+\Delta_t/2)\right)+\\ &\qquad\qquad\frac{1}{2\Delta_{FDTD}}\left(B_y(x,t)+B_y(x,t+\Delta_t)\right)\end{aligned} \tag{5.53}$$

This equation may not have a finite-element interpretation as straightforward as (5.52) because Ampere's law in the finite-element interpretation of FDTD requires partial integration [7], but it is clear enough by analogy with (5.52).

All time-stepping can be done using the equations (5.52)-(5.53) together with the standard FDTD equations in the explicit part and the implicit update equations from chapter 3 in the implicit part.

5.3.2 Spurious reflection

Consider the left interface of figure 5.20. In the left explicit part, the discrete vacuum solution is (section 3.1.2)

$$E_y = \left(e_{y,e,+} \exp\left(ik_e x\right) + e_{y,e,-} \exp\left(-ik_e x\right)\right) \exp(-i\omega t) \tag{5.54}$$

$$B_z = \frac{1}{c}\left(e_{y,e,+} \exp\left(ik_e x\right) - e_{y,e,-} \exp\left(-ik_e x\right)\right) \exp(-i\omega t) \tag{5.55}$$

where k_e is the wavenumber in the explicit part, and $e_{y,e,\pm}$ is the amplitude of a wave moving in the positive resp. negative x direction.

In the implicit part, the discrete vacuum solution is (section 3.5.3)

$$E_y = e_{y,i,+} \exp\left(ik_i x\right) \exp(-i\omega t) \tag{5.56}$$

$$B_z = \frac{1}{c} e_{y,i,+} \exp\left(ik_e x\right) \exp(-i\omega t) \tag{5.57}$$

where we consider only waves moving in the positive x-direction.

Using the interface condition (5.53) and Faraday's law at $x = x_1 - \Delta/2$, we get two equations in three unknowns $e_{y,e,+}, e_{y,e,-}, e_{y,i,+}$, from which we can calculate the spurious reflection $\frac{e_{y,e,-}}{e_{y,e,+}}$. We can choose the x-coordinate of the interface, x_1 in figure 5.20, to be $x_1 = 0$ without loss of generality. Doing so, we see the spurious reflection will not depend on Δ_i, neither directly (Δ_i does not occur in the interface condition nor in Faraday's law at $x = x_1 - \Delta/2$) nor indirectly (via k_i).

The reflection coefficient is

$$\frac{e_{y,e,-}}{e_{y,e,+}} = \frac{e^{-4i\beta}\left(-\alpha e^{i\beta} + e^{\frac{i\chi}{2}} + (-1+\alpha)e^{i(\beta+\chi)}\right)\left(-(1+\alpha)e^{i\beta} + e^{\frac{i\chi}{2}} + \alpha e^{i(\beta+\chi)}\right)}{\left(\alpha - (-1+\alpha)e^{i\chi} + e^{\frac{1}{2}i(2\beta+\chi)}\right)\left(1+\alpha-\alpha e^{i\chi} + e^{\frac{1}{2}i(2\beta+x)}\right)} \tag{5.58}$$

$$\chi = \omega\Delta_t \tag{5.59}$$

$$\alpha = \frac{\Delta}{c\Delta_t} \tag{5.60}$$

$$\beta = \arcsin\left(\alpha \sin\left(\frac{\chi}{2}\right)\right) \tag{5.61}$$

If the explicit part is run at the Courant limit ($\alpha = 1$), β simplifies to $\beta = \chi/2$ and the reflection coefficient is identically zero for all waves independent of their wavelength. Numerically, this is indeed the observed behaviour. In figure 5.22 we transmit a Gaussian pulse through a thin vacuum layer modelled by the fully implicit method. The spectrum in front of this layer is as good as identical to the spectrum behind this layer, abs(transmission coefficient) = 1.

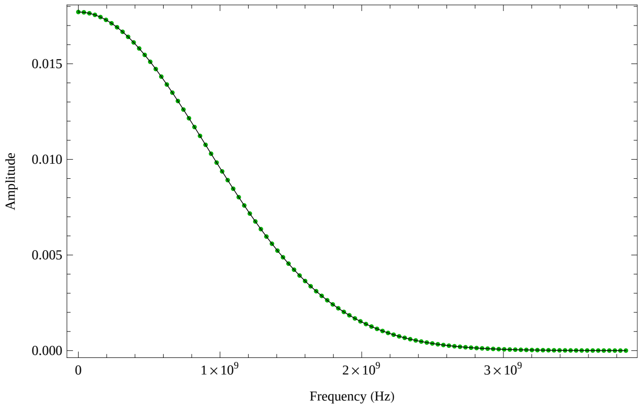

Figure 5.22: Spectrum in front of (green dots) and behind (black line) a thin implicit vacuum layer. These curves are almost exactly the same, there is no spurious reflection.

5.4 Conclusion

In this chapter we discussed our earlier work on FDTD refinement in cylindrical coordinates. We also constructed a hybridisation of the fully implicit method from chapter 3 with the FDTD method. This hybridisation enables us to model large amplitude changes over very short length scales, as in section 4.5, while modeling the rest of the simulation region with classical FDTD. In 1D, this hybridisation does not introduce any spurious reflection at the implicit/explicit interface.

Bibliography

[1] J.P. Bérenger. A Huygens subgridding for the FDTD method. *IEEE Transactions on Antennas and Propagation*, 54(12):3797–3804, 2006.

[2] ITER International Team B.J. Green and Participant Teams. ITER: burning plasma physics experiment. *Plasma Physics and Controlled Fusion*, 45(5):687, 2003.

[3] M. Bonilla, M.-F.Wong, and V. F. Hanna. A finite-element formulation for FDTD subgridding. *Microw. Opt. Technol. Lett.*, 32(2):104–108, 2002.

[4] S. C. Brenner and L. R. Scott. *The mathematical theory of finite element methods*. Springer, 2008.

[5] R. C. Carter, J. Feng, and U. Becker. Calculation of the properties of reentrant cylindrical cavity resonators. *IEEE Transactions on Microwave Theory and Techniques*, 55(12):2531–2538, Dec 2007.

[6] J. Chen and J. Wang. A novel body-of-revolution finite-difference time-domain method with weakly conditional stability. *IEEE Microwave and Wireless Components Letters*, 18(6):377–379, 2008.

[7] R. A. Chilton. *H-, P- and T-refinement strategies for the finite-difference-time-domain (FDTD) method developed via finite-element (FE) principles*. PhD thesis, Ohio State University, 2008.

[8] R. A. Chilton and R. Lee. Conservative and provably stable FDTD subgridding. *IEEE Transactions on Antennas and Propagation*, 55(9):2537–2549, Sep 2007.

[9] D.B. Davidson and R.W. Ziolkowski. Body-of-revolution finite-difference time-domain modeling of space-time focusing by a three-dimensional lens. *J. Opt. Soc. Amer. A*, 11(4):1471–1490, 1994.

[10] B. Donderici and F. L. Teixeira. Improved FDTD subgridding algorithms via digital filtering and domain overriding. *IEEE Transactions on Antennas and Propagation*, 53(9):2938–2951, 2005.

[11] B. Donderici and F. L. Teixeira. Domain-overriding and digital filtering for 3D FDTD subgridded simulations. *IEEE Microwave and Wireless Components Letters*, 16(1):10–12, 2006.

[12] Y. Yi H.-L. Chen, B. Chen and D.-G. Fang. Unconditionally stable ADI-BOR-FDTD algorithm for the analysis of rotationally symmetric geometries. *IEEE Microwave and Wireless Components Letters*, 17(4):304–306, 2007.

[13] J. Yamauchi J. Shibayama, B. Murakami and H. Nakano. LOD-BOR-FDTD algorithm for efficient analysis of circularly symmetric structures. *IEEE Microwave and Wireless Components Letters*, 19(2):56–58, 2009.

[14] D.J. Pommerenke K. Xiao and J.L. Drewniak. A three-dimensional FDTD subgridding algorithm with separated temporal and spatial interfaces and related stability analysis. *IEEE Transactions on Antennas and Propagation*, 55(7):1981–1990, 2007.

[15] L. Kulas and M. Mrozowski. Low-reflection subgridding. *IEEE Transactions on Microwave Theory and Techniques*, 53(5):1587–1592, May 2005.

[16] R. Lee. A note on mass lumping in the finite element time domain method. *IEEE Transactions on Antennas and Propagation*, 54(2):760–760, 2006.

[17] E. Okoniewska M. Okoniewski and M.A. Stuchly. Three-dimensional subgridding algorithm for FDTD. *IEEE Transactions on Antennas and Propagation*, 45(3):422–429, 1997.

[18] P. Monk. Subgridding FDTD schemes. *Applied Computational Electromagnetics Journal*, 11(1):37–46, 1996.

[19] E. R. Rebhan and G. Van Oost. Thermonuclear burn criteria for D-T plasmas. *Fusion Science and Technology*, 49(2):16–26, 2006.

[20] D. N. Smithe. Finite-difference time-domain simulation of fusion plasmas at radiofrequency time scales. *Physics of Plasmas*, 14(14):2537–2549, Apr. 2007.

[21] T. Stix. *Waves in Plasmas*. American Institute of Physics, 1992.

[22] A. Taflove and S. Hagness. *Computational Electrodynamics: The Finite-Difference Time-Domain Method*. Artech House, 2005.

[23] R. Taylor. Calculation of resonant frequencies of re-entrant cylindrical electromagnetic cavities. *Journal of Nuclear Energy, part C : Plasma Physics*, 3:129–134, 1961.

[24] F. L. Teixeira. FDTD/FETD methods: a review on some recent advances and selected applications. *Journal of Microwaves and Optoelectronics*, 6(1):83–95, Jun. 2007.

[25] P. Thoma and T. Weiland. A consistent subgridding scheme for the Finite Difference Time Domain method. *Int. J. Num. Model.: Electr. Netw., Devices and Fields,*, 9:359–374, 1996.

[26] W. Tierens and D. De Zutter. BOR-FDTD subgridding based on finite element principles. *Journal of Computational Physics*, pages 4519–4535, 2011.

[27] T. D. Tsiboukis. *Synthesis Lectures on Computational Electromagnetics*. Morgan & Claypool Publ., 2006.

[28] S. Wang and F. L. Teixeira. Some remarks on the stability of time-domain electromagnetic simulations. *IEEE Transactions on Antennas and Propagation*, 52(3):895–898, 2004.

[29] S. Wang, F. L. Teixeira, R. Lee, and J.-F. Lee. Optimization of subgridding schemes for FDTD. *IEEE Microwave and Wireless Component Letters*, 12(6):223–225, 2002.

[30] M. F. Wong, V. F. Hanna, and J. Wiart. Finite element formulation of space-time subgridding scheme in the FDTD method. *Int. J. Num. Model*, 13:127–137, 2000.

[31] R. Mittra Y. Chen and P. Harms. Finite-difference time-domain algorithm for solving Maxwell's equations in rotationally symmetric geometries. *IEEE Transactions on Microwave Theory and Techniques*, 44(6):832–839, 1996.

Conclusion and future work

Overall conclusion

In this doctoral thesis a finite-difference-like unconditionally stable discretisation of Maxwell's equations on fully collocated grids was derived. This enables the discretisation of a variety of material descriptions (auxiliary differential equations, ADEs) in their natural form, without undue additional interpolations, as well as the effective modeling of waves whose speed is much slower than the vacuum lightspeed c. Furthermore, an unconditionally well-behaved ADE-based approach was derived which describes "warm" plasma behaviour, including Bernstein waves, in time-domain. We used our discretisation of Maxwell's equations combined with these plasma descriptions to calculate wave propagation in a variety of scenarios including a plasma wave beach, mode conversion, and Budden tunneling.

Possible future work on plasma physics

In section 2.4.3, we found a double root at $\omega = 0$. This is evidence indicating that the same physics might be describable using one less degree of freedom, i.e. 7 rather than 8 degrees of freedom.

So far, our warm plasma descriptions are limited to perpendicular propagation $k_{||} = 0$. It is probably possible to extend the results of chapter 2 to some finite order in $k_{||}$ by introducing coupling terms between the equations for the $\vec{E} \perp \vec{B}_0$ case and the $\vec{E} \parallel \vec{B}_0$ case. This would still not include Landau damping since the imaginary part of the plasma dispersion function $Z(\zeta)$ (which is responsible for the damping) is not analytic at $\zeta = \infty$ [2]:

$$Z(\zeta) \simeq i\sqrt{\pi}\exp(-\zeta^2) - \frac{1}{\zeta}\sum_{n=0}^{\infty}\frac{d_n}{\zeta^{2n}} \text{ assuming } \zeta \in \mathbb{R} \tag{5.62}$$

$$d_0 = 1 \tag{5.63}$$

$$d_{n+1} = \frac{2n+1}{2}d_n \tag{5.64}$$

Going further, it may be possible to repeat the derivations of chapter 2 at some constant nonzero $k_{||}$, which should lead to descriptions that include Landau damping but no poloidal fields. To generalize even further, an expansion in $k_{||}$ around some nonzero $k_{||}$ could include even poloidal effects.

As we have pointed out repeatedly, the study of non-uniform warm plasmas requires knowledge of the ordering of the spatial derivative operators w.r.t. position-dependent equilibrium quantities, an ordering which cannot be obtained by lines of reasoning starting from the dielectric tensor alone. This, too, requires further work.

A time-domain plasma description may also be useful for the study of nonlinear phenomena such as parametric decay [4, 3, 1].

Possible future work on computational electrodynamics

As it turns out, our collocated method can be effectively hybridized with more standard FDTD methods, enabling e.g. the modeling of wave propagation through very thin layers of conducting material without having to decrease the FDTD discretisation length or time step. In 1D, this can even be done without introducing any spurious reflections whatsoever. We do not expect this particular result to hold in 2 or 3 spatial dimensions, but it is reasonable to expect that the spurious reflections will still be very low. It seems possible to generalize this hybridized method to 2D and 3D by using staggered discretisations in the directions along the material surface and fully implicit discretisations in the direction perpendicular to it, in which case the equations decouple into a number of essentially 1D problems which are banded and efficiently solvable. Such a technique may well be quite useful in e.g. electromagnetic compatibility (EMC) problems.

For the modeling of magnetized plasmas and other anisotropic materials, a full 2D or 3D version of this method would be useful. Wile this can be done in principle (in fact we gave a 2D example in [5]), in practice an efficient method is needed to solve the sparse set of equations which has to be solved at every time step, possibly based on preconditioners and iterative methods. For this, a deeper understanding of these equations and their condition numbers is needed.

It is possible to construct higher-order collocated fully implicit methods. The first such higher-order method employs piecewise cubic rather than piecewise linear basis-functions, and has two (instead of one) degrees of freedom per component per vector field per discretisation point. The associated “interpolator” is unconditionally invertible: its eigenvalues are bounded away from zero for all system sizes (this contrasts with the first-order interpolator, which is only invertible for odd system sizes and its eigenvalues approach zero as the system size becomes larger). This gives hope that such methods might be leveraged to influence the condition number of the set of equations which must be solved, possibly enabling the use of highly efficient iterative methods.

Bibliography

[1] T. Amano and M. Okamoto. Parametric effects of an alternating field on inhomogeneous plasmas. *Journal of the Physical Society of Japan*, 26(2):529–540, 1969.

[2] M. Brambilla. *Kinetic theory of plasma waves*. Clarendon Press, 1998.

[3] M. Porkolab. Theory of parametric instability near the lower-hybrid frequency. *Physics of Fluids*, 17(7), 1974.

[4] D. N. Smithe. Time domain modeling of plasmas at RF time-scales. *Journal of Physics: Conference Series*, 78(1):012069, 2007.

[5] W. Tierens and D. De Zutter. An unconditionally stable time-domain discretization on cartesian meshes for the simulation of nonuniform magnetized cold plasma. *Journal of Computational Physics*, pages 5144–5156, 2012.